AN EXPERIMENTAL INVESTIGATION OF MICROEXPLOSION

IN EMULSIFIED VEGETABLE-METHANOL BLEND

A Thesis

by

HYUNGSEOK NAM

Submitted to the Office of Graduate Studies of
Texas A&M University
in partial fulfillment of the requirements for the degree of

MASTER OF SCIENCE

May 2012

Major Subject: Mechanical Engineering

An Experimental Investigation of Microexplosion in Emulsified Vegetable-Methanol

Blend

AN EXPERIMENTAL INVESTIGATION OF MICROEXPLOSION

IN EMULSIFIED VEGETABLE-METHANOL BLEND

A Thesis

by

HYUNGSEOK NAM

Submitted to the Office of Graduate Studies of
Texas A&M University
in partial fulfillment of the requirements for the degree of

MASTER OF SCIENCE

Approved by:

Chair of Committee,   Jorge L. Alvarado
Committee Members,   Kalyan Annamalai
                            Sergio C. Capareda
Head of Department,   Jerald Caton

May 2012

Major Subject: Mechanical Engineering

ABSTRACT

An Experimental Investigation of Microexplosion in Emulsified Vegetable-Methanol

Blend. (May 2012)

Hyungseok Nam, B.S., SungKyunKwan University, Korea

Chair of Advisory Committee: Dr. Jorge L. Alvarado

Vegetable oil is one of the most widely available renewable sources of energy that can be used to meet the world's demands. Many vegetable oils also have the advantage of containing little to no detectable amounts of nitrogen. Recently, research studies have revealed that when two liquids with different vapor pressure values are formed into droplet-like emulsions, a microexplosion effect can happen under specific environmental conditions. Understanding the microexplosion phenomenon can help increase the efficiency of bio-emulsion combustion as well as reduce pollution levels. Many researchers have conducted experiments to find the optimal condition that induces microexplosion effects. Microexplosion is also associated with the formation of shock waves characteristic of explosions at larger scales. However, little is known about how emulsion composition and droplet size affect the microexplosion process.

Through this research, methanol-in-vegetable oil emulsion has been studied from the microexplosion point of view using custom made electric furnace equipment with a high speed camera system and an acoustic sensor system. The main goal of this study is to understand the effect of emulsion compositions, chamber temperatures, and droplet sizes

on the characteristics of microexplosion. First, an n-hexadecane-in-water emulsion was prepared to validate the performance of the custom-made experimental apparatus using previous published data. Methanol-in-canola oil emulsions with different compositions were also prepared and used to compare the microexplosion phenomena with water as a volatile compound. Microexplosion events of the blended fuels were captured using a high speed camera and an acoustic sensor. The wave signals generated by the microexplosion were analyzed after converting the signals using a Fast Fourier Transform coded in Matlab.

One of the major findings of this research work was that higher temperatures and higher concentrations of high vapor pressure fluids such as methanol and water in emulsions causes a high probability of microexplosion event due to the sudden expansion of the emulsified fluid. Also, the effect of size on microexplosion was evident in the greater probability of explosion. Methanol-in-canola oil emulsion with 15 % methanol with droplets size of 200 μm placed in a furnace chamber heated to 980 ˚C showed optimal microexplosion behavior based on the formation of fine droplets. Also, smaller droplets produced higher frequencies, which could be used to detect microexplosion without high speed imaging. When large droplets microexploded, lower frequencies were detected in all the blends.

DEDICATION

This thesis is dedicated to my family, Mr. Ki-Woo Nam, Mrs. Jung-Hee Park, Mrs. Myung-Ok Won, Mrs. Ji-Hye Han, Mr. Dae-Hoon Han and Mr. Ho-Seok Nam, for their love, guidance and continuous support through my vital educational years.

ACKNOWLEDGEMENTS

I would like to offer my sincere gratitude to several people who made this thesis possible. First, I wish to thank my committee chair, Dr. Jorge L. Alvarado, for his guidance and mentorship. He has always been extremely helpful, and has generously shared his knowledge with me throughout the numerous discussions we had during the course of this research work. I would also like to thank two committee members for their kind assistance: Dr. Kalyan Annamalai for giving me an idea of combustion science, and Dr. Sergio C. Capareda for his support of this thesis.

In addition, I wish to express my gratitude to Dr. Jung Soon Jeong for his assistance in making Labview codes, and to Dr. Jin-Wook Kim at KIMS (Korean Institute of Materials Science) for his instructions on the concept of vibration and Fast Fourier Transform. I would also like to thank my fellow members of Dr. Alvarado's research team, Gautam Sandesh Savant and Qibo Li, for their wholehearted support; Shreyas Bhimani for all the assistance he gave me in imparting a basic knowledge of combustion science, as well as his dedication to my research work; Soo-Yeon Lee for her help in solving a differential equation; and Dae-Hoon Han for his assistance in making final PowerPoint slides. I must also extend my gratitude to my best friend, Suk-Bae Joo, for always reminding me of the importance of persistence and hard work.

In closing, I would like to thank my parents for their encouragement and the unconditional love they have instilled in me right from the time when I was a little child.

And last but not least, I wish to thank my lovely wife, Jihye Han, for inspiring me to make

the necessary effort to bring this thesis to fruition.

NOMENCLATURE

G_1^I	Total free energy of molecules of liquid 1 in state I [J]
G_2^I	Total free energy of molecules of liquid 2 in state I [J]
G_{12}^I	Excess interfacial free energy between liquid 1 and 2 in state I [J]
ΔG^{form}	Free energy of emulsion formation [J]
T'	Temperature [˚C]
$S_2^{II,config}$	Configurational entropy of the droplets of liquid 2 in state II [J/kg-K]
n_i	Number of moles of component i with chemical potential μ_i
A^I	Total area of a droplet 2 in state I [m]
A^{II}	Total area of droplets 2 in state II [m]
R_1	Radius of curvature for the liquid 1 in state I [m]
$\Delta P_{droplet}$	Difference in pressure [pa]
T	Period of wave length [s]
f_s	Sampling frequency [Hz]
$X(\omega)$	Fourier transform of x(t)
$A(\omega)$	Even function of ω
$B(\omega)$	Odd function of ω
$x(t)$	Periodic function of time t with period T
t	Time of wave [s]
K	Microexplosion strength

M	Total mass of droplet including oil and water [kg]
J	Bubble nucleation rate [$1/m^3s^1$]
R_0	Initial radius of emulsion droplet [m]
R_1	Radius of emulsion kernel when oil membrane is formed [m]
k	Boltzmann's constant [1.3808×10^{-23} J/K]
h	Plank's constant [6.6261×10^{-34} J·s]
r_{cr}	Critical diameter of a vapor embryo [m]
n_T	Number of potential nucleation sites per unit volume
$V_{ellipse}$	Volume of ellipse [m^3]
r_{sphere}	Radius of sphere [m]
$u\,(x\,,t)$	Displacement of the plane of particle [m]
E	Elastic modulus [pa]
ΔP	Change in linear momentum [pa]
I	Impulse [N·s]
F	Constant total net force [N]
$\Delta t'$	Time interval over the impulse force [s]
m	Constant mass of the object [kg]
Δv	Change in wave velocity produced by the force [m/s]
V_{Total}	Volume of the droplets right before microexplosion [m^3]
Vi	Volume of the distributed (countable) droplets after ME [m^3]
Vii	Volume of fine droplets (below 10 μm) [m^3]

y   Percentage of fine droplets [%]

Greek symbols

$\emptyset$ Volume fraction of water in an emulsified oil

ω_k Frequency of the *k*th harmonic [Hz]

γ_{12} Interfacial tension between liquid 1 and liquid 2 [dyne/cm]

ω Angular frequency [Hz]

Acronyms

EIA   US Energy Information Administration

SO_x Sulfur Dioxide

CO_x Carbon Monoxide

NO_x Nitrogen Oxides

FFT   Fast Fourier Transforms

DFT   Discrete Fourier Transforms

HLB   Hydrophillic-Lipophile Balance

W/O   Water-in-Oil emulsion

O/W   Oil-in-Water emulsion

O/O   Oil-in-Oil emulsion

W/O/W   Water-in-Oil-in-Water emulsion

HHV   Higher Heating Value

GHG   Greenhouse Gases

PM   Particulate Matter

AE   Acoustic Emission

SNR   Signal-to-Noise Ratio

B-R   Birchley-Riley model

CM   Methanol-in-Canola oil

CW   Water-in-Canola oil

HW   Water-in-Hexadecane

PFI   Programmable Function Interface

DAQ   Data Acquisition

ME   Microexplosion

Vi   Virtual Instruments

TABLE OF CONTENTS

LIST OF FIGURES

LIST OF TABLES

1. INTRODUCTION

The worldwide economic growth in recent decades has led to improvement in living standards and greater prosperity for individuals. New state-of-art technologies in transportation and electronic equipment have benefited humankind greatly. However, economic growth cannot be separated from the corresponding environmental impacts including issues related to air pollution, global warming and the depletion of global resources. Economic growth is deeply related with the amount of electricity generation and its corresponding emissions. According to US Energy Information Administration (EIA), the main sources for electricity generation in 2009 were coal (44.5 %), natural gas (23.3 %) and nuclear energy (20.2 %) out of 3,950 billion kWh. The use of fossil fuel among all the available sources reaches almost 70 %.

Fossil fuels are used in many applications including coal in boiler or thermal power plants, natural gas for heating applications and cooking, and petroleum products for transportation. The main advantages of fossil fuels include their relative low cost, abundant supply, and a large infrastructure system in place to deliver them to users around the world. However, a major disadvantage of burning fossil fuel such as coal, petroleum and natural gas is the related air pollution that is produced during their use. Excessive air pollution can result in worse living standards for humans and more pronounced global warming effects. The harmful emissions from fossil fuel are mainly composed of sulfur dioxide (SO_x), carbon dioxide and carbon monoxide (CO_x), nitrogen oxides (NO_x), and

_____

This thesis follows the style of Applied Thermal Engineering.

soot. Recently, as the concerns about low-level ozone (tropospheric ozone) have gained significant relevance recently, ozone precursors such as NO_x and soot are still major environmental factors amongst all the exhaust gases produced during the combustion of fossil fuels. Low-level ozone causes pulmonary diseases among children and the elderly in many metropolitan areas. Another drawback of combusting fossil fuel is the depletion of the world resources.

Vegetable oil is one of the available renewable sources of energy that can be used to meet the world's demand. Many vegetable oils also have the advantage of containing little to no detectable amount of nitrogen. The most widely adopted type of vegetable oil is biodiesel. Biodiesel is made through the process of transesterification, which consists of removing triglycerides and combining oil esters of vegetable oil with alcohol to make biodiesel a low viscosity fuel. The process is time consuming and expensive. Moreover, as part of the transesterification process, byproducts such as glycerol are produced, which needs to be disposed of properly. Another method of using vegetable oil is by mixing alcohol with vegetable oil emulsions. The benefits of using alcohol-in-vegetable oil emulsion include the elimination of several transformation processes including transesterification and the associated production of glycerol.

Recently, research studies have revealed that when two liquids with different vapor pressure values are formed into droplet-like emulsions, a microexplosion effect can happen under specific environmental conditions. When such emulsions are sprayed in a high temperature chamber, the sudden expansion of volatile compounds that usually exhibit high vapor pressure values leads to a violent microexplosion of the emulsified

droplets. The microexplosion phenomena involve formation of smaller droplets with very high surface-to-volume ratio which result in better mixing with air leading to more complete combustion and lower NO_x emissions.

Understanding the microexplosion phenomena can help increase the efficiency of bio-emulsion combustion as well as reducing pollution levels. Many researchers have conducted experiments to find out the optimal condition to induce microexplosion effects by suspending single droplets on a thin wire. Microexplosion is also associated with the formation of shock waves characteristic of explosion at larger scales. However, little is known about how emulsion composition and droplet size affect the microexplosion process.

For this study, an experimental apparatus was developed to understand the role of bio-emulsion composition, droplet size and chamber temperature on microexplosion effects. The experimental apparatus consisted of a high speed camera for capturing the images of the microexplosion events and an acoustic sensor to understand the explosion characteristic of each emulsion. First, n-hexadecane (19 %) mixed with water (79 %) and surfactant (2 %) was prepared to validate the experimental apparatus using previous published data. Then different emulsions consisting of canola oil and methanol at different compositions were prepared. Also, water-in-canola oil was used to compare the microexplosion phenomena when different volatile fluids such as alcohols were used. Pure canola oil was chosen because of its relatively cheaper cost, availability, and low nitrogen content. Also, other vegetable oils like soybean, rapeseed, corn, and peanut oils have already been researched a lot in recent years.

The main goal of this research study was to find out the effect of emulsions composition, furnace temperature, and initial droplet size on the particles size distribution of the small droplets formed after microexplosion. In addition, the acoustic characteristics of microexplosion including, microexplosion amplitude and frequency range were also considered. All the experiments were conducted at constant furnace temperatures of 900 ˚C and 980 ˚C. The initial single droplet sizes were 230 µm (±8 µm) and 300 µm (±8 µm). The high speed camera system and the acoustic sensor were synchronized to get droplet images and acoustic signal waves of microexplosion event at the same time. All the collected wave signals were analyzed using the Fast Fourier Transform (FFT) algorithm using Matlab to understand the frequency properties of droplet microexplosion.

2. LITERATURE REVIEW

In this section, a short description of microexplosion phenomena is presented including a discussion of their properties and principles. The section also covers emulsions, emulsifiers, basic concept of explosion, fast Fourier transform, and signal processing. Additionally, past research studies done in the area of detecting microexplosion are also introduced.

2.1 Emulsions

Emulsions are defined as thermodynamically unstable dispersions of two insoluble fluids such as water and oil [1]. The types of emulsions are largely classified as water-in-oil (W/O) emulsion, oil-in-water (O/W) emulsion, oil-in-oil (O/O) emulsion and double emulsion (W/O/W). Oil-in-oil emulsion, for example, consists of methanol dispersed in canola oil, and the former type (O/W) is made of water dispersed in hexadecane. The size of emulsion in liquid-liquid dispersion can be distinguished as white macro-emulsion (0.1 μm to 100 μm) and the translucent micro-emulsion (less than 100 nm).

2.1.1 Emulsion Formation and Its Break-Down

There are many ways to produce liquid-to-liquid emulsions. The first step is to mix two immiscible liquids is to separate the dispersed phases into smaller droplets by applying the mechanical energy [2]. Then these fine droplets are enclosed by a continuous

phase before emulsification. Interaction energies between emulsion droplets arise from Van der Waals, electrostatic and steric forces [1]. Techniques of applying mechanical energy include ultra-sonic, high pressure homogenizer, stirring and blending, injection of dispersed droplets into continuous phase, and the phase inversion technique [2].

When emulsions are made with forced mechanical energy, the separate phases mix, and form stable droplets of one phase inside the other in a way that reduces the free energy according to the second law of thermodynamics. Stable droplets (aggregates) are maintained in a metastable state when a stable barrier among them keeps the droplet from coalescing. However, external perturbation or chemical imbalance can induce droplet coalescence which diminishes the stability of the emulsion [1]. Coalescence takes place when the metastable state is disturbed strong enough so the system can reach a different equilibrium state which minimizes surface energy by decreasing surface. After coalescence occurs, particles would settle according to their density values resulting in creaming or sediment formation. To make emulsions more stable, emulsifiers or surfactants are needed to help reduce surface energy while increasing the repulsive nature of the droplets. A summary of emulsifier or surfactants is provided in the section 2.1.3.

2.1.2 Thermodynamics in Emulsion Formation and Break-Down

A more detailed understanding of emulsions can be explained with the Gibbs model, which regards the process as an equilibrium phenomenon. Physically, the emulsions are formed when a droplet of liquid 2 in state I is disrupted forming smaller liquid droplets 2 as shown in Figure 1 (State II).
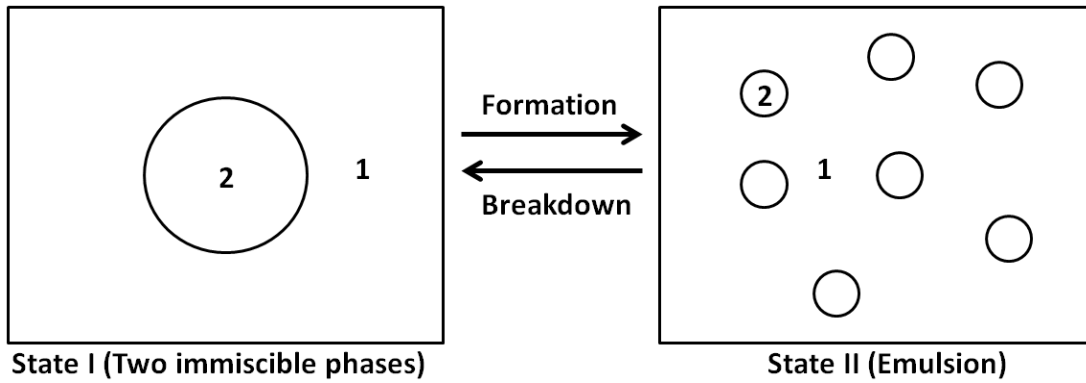
Figure 1. Emulsion formation and breakdown [3].

During the formation of an emulsion, the change in free energy from state I to state II can be represented using thermodynamic equations. The total free energy of G^I and G^{II} of state I and state II, respectively can be expressed as follows.

$$G^I = G_1^I + G_2^I + G_{12}^I \qquad (1)$$

$$G^{II} = G_1^{II} + G_2^{II} + G_{12}^{II} - T' \bullet S_2^{II,config} \qquad (2)$$

where, G_1^I is the total free energy of molecules of liquid 1 in state I

G_2^I is the total free energy of molecules of liquid 2 in state I

G_{12}^I is the excess interfacial free energy between liquid 1 and 2 in state I

$S_2^{II,config}$ is the configurational entropy of the droplets of liquid 2 in state II

T' is temperature

The free energy of emulsion formation of ΔG^{form}, which shows an energy change from State I to State II, is

$$\Delta G^{form} = G^{II} - G^{I} = G_{12}^{II} - G_{12}^{I} - T' \bullet S_2^{II,config}$$ (3)

The Gibbs fundamental equation (4) relates changes in Gibbs free energy to entropy, interfacial energy and composition.

$$dG_{12}^{I} = -S^{I} dT_{12} + A^{I} d\gamma_{12} + \sum n_i d\mu_i$$ (4)

where, γ_{12} is the interfacial tension between liquid 1 and liquid 2

n_i is the number of moles of component i with chemical potential μ_i

At constant temperature and composition, the Gibbs fundamental equation (4) can be reduced to

$$dG_{12}^{I} = A^{I} d\gamma_{12}$$ (5)

For a stable interface, Equation (5) can be expressed as

$$G_{12}^{I} = A^{I} \gamma_{12}$$ (6)

Combining Equations (3) and (6), the free energy of emulsion formation ΔG^{form} can be expressed as

$$\Delta G^{form} = \Delta A \gamma_{12} - T' \Delta S^{conf}$$ (7)

where, $\Delta A = A^{II} - A^{I}$;

A^{I} is the total area of a droplet 2 in state I

A^{II} is the total area of droplets 2 in state II

When emulsion formation takes place, both the interfacial energy term $\left(\Delta A \gamma_{12}\right)$ and the configurational entropy term $\left(T'\Delta S^{conf}\right)$ are positive, but $\Delta A \gamma_{12} >> T'\Delta S^{conf}$ in most cases. Therefore, the Gibbs free energy of formation is positive, which indicates that emulsion formation happens non-spontaneously since the emulsion is thermodynamically unstable state due to the large value of $\Delta A \gamma_{12}$.

Without any stabilization mechanism, the emulsion breaks down by flocculation and coalescence in the absence of external forces [2]. Flocculation, which usually happens before coalescence, is aggregation of the droplets with no change in primary droplet size. It occurs when the repulsion force is not strong enough to keep droplets apart. The coalescence is the fusion of two or more droplets which form larger droplets because of the disruption of droplets surface barriers. This happens when the stronger van der Waals attraction force is comparable with the repulsion force. Moreover, larger droplets require less surface energy per unit volume since they exhibit lower surface-to-volume ratio than smaller droplets. The change in Gibbs free energy from state II to state I proceeds as shown in Figure 2 in the absence of a stabilizer because Gibbs free energy always try to be minimized when a system reaches equilibrium at constant pressure and temperature. Thus, the emulsion looks for equilibrium state by reducing $\Delta A \gamma_{12}$ term, since $\Delta A \gamma_{12} >> T'\Delta S^{conf}$

.
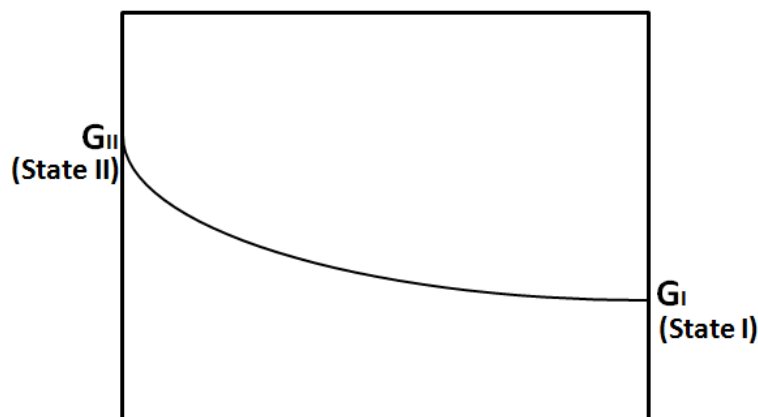
Figure 2. The Gibbs free energy curve when the emulsion breaks down in the absence of an emulsifier [3].

If an emulsifier is used to stabilize the emulsion, an energy barrier arises between the droplets. The breakdown process from state II to state I of emulsified emulsion is more difficult than that of non-emulsified emulsion. Figure 3 depicts two metastable states; one at state II and the other at the cup-shaped turning point. If the maximum Gibbs free energy values are sufficiently high, the emulsions remain in the stable state indefinitely at constant pressure and temperature. These metastable cases are regarded as kinetically stable rather than thermodynamically stable. In fact, thermodynamically, they can only be considered to be metastable states. In the case of kinetically stable emulsion, a third component such as surfactants or emulsifiers is used to keep them kinetically stable even if there are no thermodynamically metastable states present. For a thermodynamically metastable state, no energy is required to make them stable.
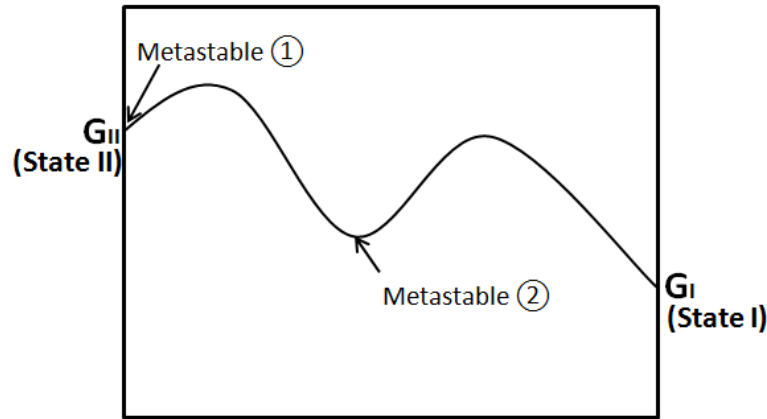
Figure 3. The Gibbs free energy curve for breakdown of systems in the presence of a surfactant or emulsifier [3].

2.1.3 Emulsifier and HLB Concept

The role of emulsifier, which is also referred to as surfactant, is to lower the surface tension of liquid at the interface between two immiscible liquids. By reducing the interfacial tension, the formation of emulsion is easily achieved by just using a high-speed mixer to achieve large droplet emulsions such as macro-emulsions. However, a large amount of energy is needed to form smaller droplet emulsions [3]. From physics, it is known that Laplace pressure, which is the pressure difference between the inside and the outside of a droplet, can be used to estimate droplet size given the surface tension of the two fluids. The pressure at the concave side of interfacial tension γ is almost always larger than that at convex side [2]. For a perfectly spherical droplet, the Laplace pressure is given by

$$\Delta P_{droplet} = \gamma \left(\frac{1}{R_1} + \frac{1}{R_2} \right) = \frac{2\gamma}{R} \tag{8}$$

where, R_1 and R_2 are the radius of curvature for the liquid 1 and 2 in state I

$\Delta P_{droplet}$ is the difference in pressure

Thus, the emulsifier plays a major role in lowering Laplace pressure by reducing the interfacial tension (γ).
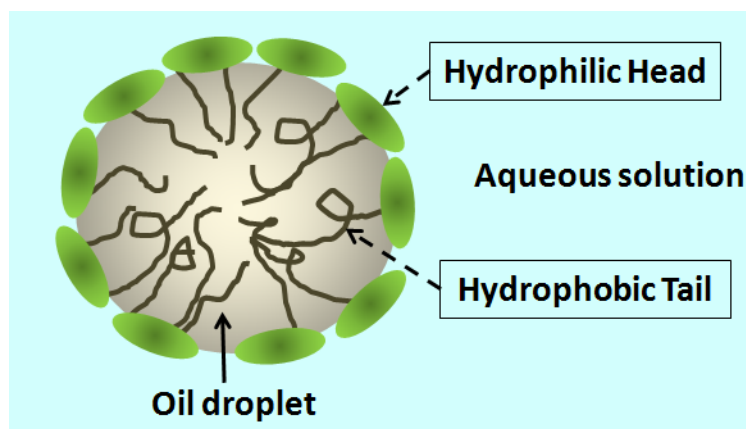
Figure 4. Schematic representation of oil-in-water (O/W).

Certain surfactants are amphiphilic organic compounds that contain hydrophobic tails and hydrophilic heads [3]. Those types of surfactants or emulsifier connect water-insoluble oil to water. As shown in Figure 4, the hydrophilic head adheres to water since water is a polar solvent, and the hydrophobic tail extends into the oil in the oil-in-water emulsion (O/W). In contrast, for a W/O emulsion, the hydrophilic head reside in water while the hydrophobic tail extends into the oil.

It is known that the selection of different emulsifier is often made on trial and error basis. One way to determine the best combination of surfactants for a given emulsion is by

using the semi-empirical scale, Hydrophillic-Lipophile Balance (HLB) value devised by

Griffin in 1949 [4]. This value is based on the percentage of hydrophilic and hydrophobic

groups in the surfactant molecule. The Equation (9) shows how to calculate the average

HLB number.

$$HLB = x_1 HLB_1 + x_2 HLB_2 \tag{9}$$

where, x_1 is the weight fraction of emulsifiers 1

x_2 is the weight fraction of emulsifiers 2

Table 1 provides a guide to the selection of emulsifiers for different applications.

In general, lower HLB value emulsifiers are used for W/O emulsions whereas higher HLB

value emulsifiers are used for O/W emulsion.

Table 1. A summary of surfactant HLB ranges and their applications [3].

HLB range	Application
3-6	W/O emulsifier
7-9	Wetting agent
8-18	O/W emulsifier
13-15	Detergent
15-18	Solubilizer

2.1.4 Canola-based Vegetable Oil Emulsion

Canola derived from 'CANadian Oil, Low Acid' is a cultivar of rapeseed that

contains less than 2 % erucid acid and less than 30 µmol/g of glucosinolates. Oil made of

plants which contain high levels of glucosinolates lead to higher emissions of NO_x during combustion due to the high amount of nitrogen in glucosinolates. Also, glucosinolates add a pungent taste to the oil. Thus, the Canadian Rapeseed Industry has refined the rapeseed cultivar in order to reduce the content of glucosinolates in rapeseed oil which is known as canola oil. As Table 2 shows, the amount of glucosinoates in traditional rapeseed oil is almost 4 times greater than that in canola oil. This also leads to less content of sulfur in canola oil. Canola oil can be considered as a multi-component fuel since it contains different hydrocarbon groups with different molecular weight [5].

Table 2. Generic properties of rapeseed and canola oil [6].

Oil composition	Traditional Rapeseed Oil	Canola Oil
Erucid acid (%)	45	<1.0
Linolenic acid (%)	8-9	8-12
Linoleic acid (%)	14-18	19-23
Oleic acid (%)	18-27	53-60
Palmitic acid (%)	3-5	3-5
Stearic acid (%)	1-3	1-3
Sulfur (ppm)	25-40	<17
Glucosinolates (μmol/g)	70-120	<26.5

Bhimani [6] used two different composition emulsion using 100 % natural canola oil of Wesson brand, 99.99 % methanol from EMD bioscience, Span 80 and Tween 80 surfactants from Sigma-Aldrich, USA. Two concentrations were made as 89 – 9 emulsion (9 % methanol mixed in 89 % canola oil with 2 % surfactant) and 85 -12.5 emulsion (12.5 %

methanol mixed in 85 % canola oil with 2.5 % surfactant). Bhimani [6] determined the ultimate analysis of pure canola oil as depicted in Table 3.

Table 3. Ultimate analysis of pure canola oil.

Element	% weight
Carbon	80.22
Hydrogen	10.9
Oxygen	8.62
Nitrogen	0.14
Sulfur	0.004
Water	0.115
Ash	0.001
HHV (KJ/Kg)	40173.3

The normalized empirical chemical formula based on one mole of carbon was calculated as $CH_{1.6305}O_{0.0015}N_{0.0015}S_{0.00002}$. The chemical formula for the two emulsions was also determined on the basis of the percentage mass of each component in a 100 g blend. After calculating the percentage contribution of each component, the empirical formulas of the 89 – 9 emulsion and the 85 – 12.5 emulsion were determined to be $CH_{1.687}O_{0.1143}N_{0.0013}S_{0.00001}$ and $CH_{1.704}O_{0.128}N_{0.0012}S_{0.00001}$, respectively.

The viscosity of the emulsions was determined at 25 ˚C by using a rotational type viscometer. The addition of methanol and emulsifier helped reduced viscosity considerably. Table 4 [6] shows viscosity and stability data of each fuel type. The results indicate that more amount of surfactants cause higher viscosity in the emulsions. From the

stability point of view, 89 – 9 emulsion is more stable than the 85 – 12.5 emulsion due in part to the lower amount of methanol used in the blend.

Table 4. Viscosity and stability of the fuels.

Fuel Type	Viscosity(cP) at 25 ˚C	Stability (hours)
Canola Oil	55	-
89-9 Emulsion	38.8	7
85-12.5 Emulsion	41.2	4

2.2 Microexplosion

The concept of microexplosion was first introduced by Ivanov and Nefdov [7] in 1965. Microexplosion takes place when droplets break up into finer droplets violently at high temperature driven by the difference in vapor pressures between the interior and exterior of each droplet. Moreover, volatile liquids surrounded by liquid with low vapor pressure exhibit lower diffusivity compared to gases. Droplets containing liquids with low diffusivity provide insufficient mass flux to support complete evaporation and combustion of volatile compounds resulting in a weaker flame. In a high temperature environment, emulsified liquids with low diffusivity cannot evaporate fully due to the rapid increase in temperature. When droplets experience a rapid temperature change, droplet grow considerably due to the formation of bubbles inside each droplet. Under extreme conditions, droplets cannot grow fast enough and experience a drastic change in internal pressure resulting in their abrupt breakage. The violent explosion of droplets is defined as

microexplosion [2]. As part of the microexplosion process, secondary droplets are formed which are at least an order of magnitude less in size than the initial droplets. Secondary droplets exhibit high surface-to-volume ratio which leads to complete combustion and lower NO_x emissions [8].

Three distinctive properties of the microexplosion phenomena have been identified recently [9]. First, emulsions have to consist of two or more liquids with sufficiently different volatilities and the concentrations of them should be in the optimum range. That is because volatile compounds experience internal bubble nucleation in lieu of reaching higher temperatures. On the other hand, less volatile liquid see an increase in droplet temperature. Second, volatile components should be surrounded by less volatile liquid when emulsion droplets are formed. This allows homogenous bubble nucleation within the volatile fluid. Lastly, microexplosion phenomena take place when the internal pressure inside the droplets increases due to increases in droplet temperature resulting in the formation of a high percentage of fine droplets whose diameter is less than 10 μm.

Houlihan [8] proposed "The Triple Crown" benefits of microexplosion including a reduction in NO_x, better fuel efficiency and lower greenhouse gases (GHG) of emulsified fuel of oil and water. When the primary fuel atomization takes place in the combustion zone, many droplets do not combust entirely leading to the formation of particulate matter (PM). Incomplete combustion takes place because relatively large droplets do not have sufficient time to completely burn [8]. In a high temperature, conditions for microexplosion are more favorable leading to a significant increase in the surface area of secondary droplets. Higher surface-to-volume ratio leads to better mixing air and a more

complete combustion. Houlihan [8] was able to correlate the high latent heat of vaporization of water to a decrease in flame temperature. The cooling effect of water also results in lower emissions of thermal NO_x which is formed through high temperature oxidation of N_2. Also, water vapor increases the number of hydroxyl (OH) radicals which help oxidize soot precursors [10]. Furthermore, addition of water vapor helps reduce the possibility of pre-ignition and detonation problems in spark ignition engines [11]. Most recent studies point out that emulsified fuels should induce a more complete combustion especially when microexplosion occurs. In such conditions, the combustion process results in better power output per fuel input and less amount of pollution which helps prevent formation of greenhouse gases (GHG) [8]. Figures 5 and 6 show the different sequence of combustion processes of pure fuel and blended fuel.
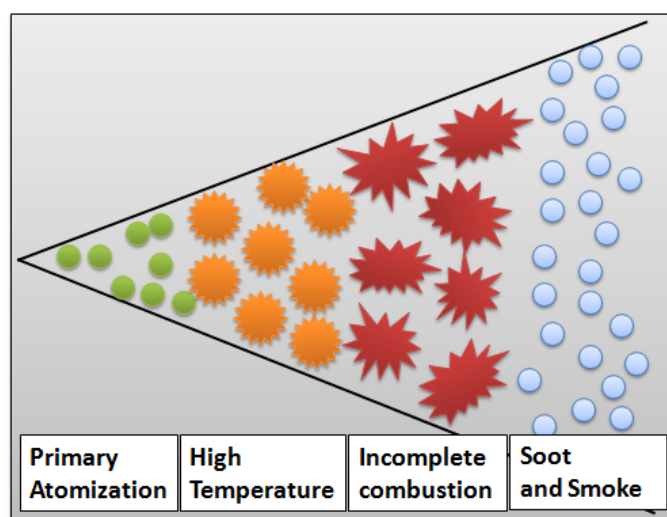
Figure 5. Regular fuel oil combustion [8].
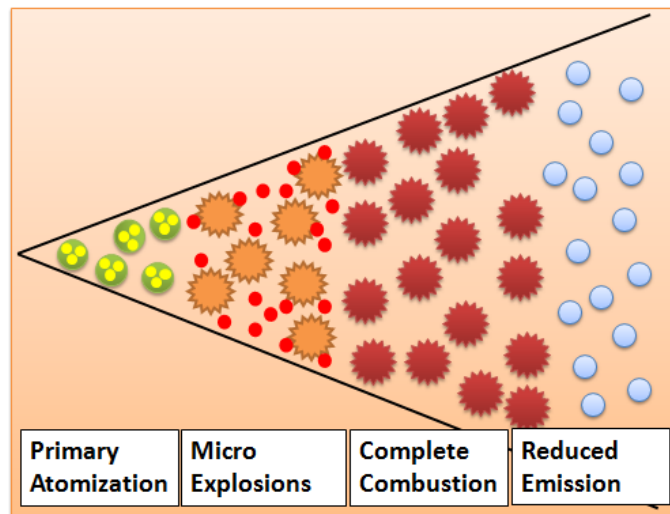
Figure 6. Emulsified fuel combustion [8].

2.2.1 Classification of Explosive Waves

An explosion is defined as a rapid release of energy compared to the surroundings and results in noise due to sudden pressure wave propagation [12]. Chemical, atomic, and thermal explosives are typical examples of explosions.

The basic concept of an explosive process can be explained with stress waves, including the detonation wave (shock wave) that propagates in gaseous, liquid or solid explosive mediums [13]. A stress wave can be divided into a normal stress wave and a tangential stress wave, which originate from the sources, such as earthquake, explosion and ultrasonic wave, and separate during propagation based on their different speed and direction. The normal stress wave or pressure wave is also referred to as rarefaction wave due to the fact that it does not usually pass mediums such as liquids, gases, and loose materials. According to the direction of the waves, the normal wave in the longitudinal

direction and the tangential wave in the transverse direction are also called P-wave and S-wave, respectively.

An understanding of the basic characteristics of each medium is necessary since the stress σ and the relative volume deformation is unique for each medium. Figures 7 (a) and (b) show the relationship between pressure stress and the relative volume deformation of fluid and solid, respectively.

(a) Fluids   (b) Solids
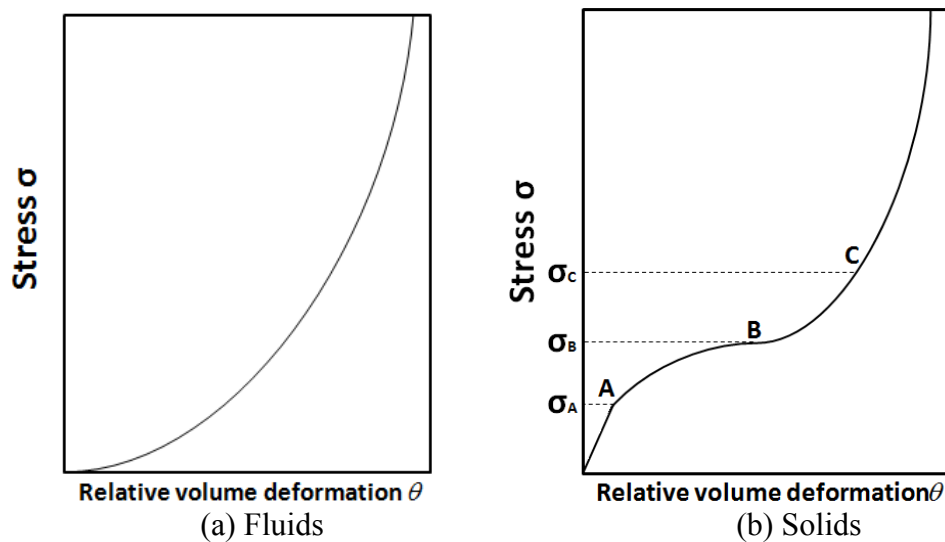
Figure 7. Relationship between pressure stresses and relative volume [13].

In solids, the stress σ changes linearly with relative volume deformation up to σ_A in an elastic range. Since $\dfrac{d\sigma}{d\theta}$ is constant in this range, while the front pressure velocity is physically equal to the velocity of sound according to the law of conservation of momentum and the law of conservation of mass [13]. Within the interval between σ_A and σ_B, the material is gradually compressed resulting in a shear stress. In relation to wave

propagation, the higher pressures are slower than the lower ones which can be referred to as plastic stress waves. In the range from σ_B to σ_C, the medium starts to behave like a fluid as shown in Figure 7 (a). This region is called the stable subsonic shock wave region, where higher pressure waves propagate faster than lower ones. Also, sound wave speed within the σ_b to σ_c region is lower than the sound wave speed in the range from 0 to σ_A. Finally, the area under the $\sigma-\theta$ curve starting at σ_C encompasses stable supersonic shock waves. Detonation waves and explosive waves are generated in this range. That means the maximum pressure and its continuous lower pressure waves are always greater than σ_C ($P > \sigma_C$). Furthermore, surface waves must be considered because most explosions take place in more than two different phases, such as rock and air, or rock and soil with different density. The surface waves propagate along the interface of the individual phase layers [13]. The typical surface waves are Rayleigh wave (R-wave) and Love wave (Q-wave).

2.3 Past Research on the Studies of Microexplosion

The combustion of sprays of liquid fuel has recently been studied in many fields of combustion science including gas turbine, internal combustion engine and boiler. Many researchers discovered that the initial droplet size, volatility, superheating, chemical composition of the fuel, and the surface tension can be attributed to the microexplosion phenomena.

Out of the many proposed, the superheat temperature and oil composition have been related to microexplosion. Tsue et al. [14] have been able to correlate time-to-microexplosion and droplet temperature. The possibility of microexplosion from

a statistical point of view has been explained as a randomly distributed phenomenon. An emulsion of 1 % of polyoxyethylene nonylphenyl ether with n-tetradecane and n-hexadecane in water was prepared to form 1.0 mm diameter droplets. In their experiments, each droplet was suspended at the end of a 0.25 mm quartz fiber and inserted into a high temperature chamber to determine the occurrence of microexplosion. From statistical analysis of all the experiments, the author discovered that the likelihood of microexplosion increases exponentially as the amount of water increases. Watanabe et al. [15] prepared W/O emulsified fuel with 90 vol. % kerosene and 10 vol. % water to detect microexplosions using emulsified fuel droplets. Two experimental apparatus were prepared in order to understand the puffing and microexplosion as a function of temperature in the furnace and the exhaust gas concentration. Puffing is defined as water vapor being blown out from the droplet surface without rupturing the whole droplet. The author [15] verified previously researched fact [16] that puffing increases when the furnace temperature and the initial droplet size increase. Thirty single droplets with diameter ranging from 0.9 – 1.0 mm were tested. Twenty-nine out of thirty droplets showed puffing, and seven of those showed microexplosion at 850 K. It confirmed that microexplosion occurs after puffing. From the experiments, the difference between microexplosions and puffing was clearly identified by high speed imaging. Furthermore, it became evident that microexplosion occurs more frequently when water changes to vapor abruptly, and that higher superheat temperatures resulted in higher incidence of microexplosion. In similar experiments which consisted of using fuel sprays, temperature distribution inside the furnace became more uniform. Also, temperature was lower due to

the cooling effect caused by the vaporization of water. The latent heat of water and the secondary atomization of microexploded droplets led to the reduction of NO_x concentration.

In 1993, Takei et al. [17] tested small emulsified droplets composed of n-hexadecane and n-heptane in a laboratory scale chamber. n-hexadecane and n-heptane depict low and high volatility, respectively. The amount of time required for ignition suspended fuel droplets was recorded and correlated to initial droplet diameter, fuel mixture ratio, and the ambient temperature. The author [17] observed that large droplets or droplets that contain less volatile fuel require more time was for evaporation. Due to insufficient time allowed for evaporation, larger droplets basically burnt out without microexploding or mixing properly with oxygen. On the other hand, smaller droplets had sufficient time to mix with air before completely vaporizing. The author was able to correlate droplet size to the Damkohler number (mass transport time/reaction time) which he used to show mass transfer time becomes shorter as the reaction time becomes relatively long. Also, this also means that ignition time is inversely proportional to droplet size and could lead to a situation where no ignition takes place since the droplet contents tends to vaporize under those conditions. The author also tested 1 mm diameter droplets made of 40 % heptane (volatile compound) and 60 % of hexadecane (compound with low volatility). During the test, the small droplets disappeared before ignition occurred because heptane vaporized before having the possibility of being ignited, whereas the large droplets ignited easily as soon as heptanes reached the boiling point. It can be concluded that smaller droplets combust after reaching the boiling point of the less

volatile fuel while combustion of larger droplets containing volatile fuel takes place before reaching the fuel's boiling point.

Ferrante et al. [18] studied microexplosion of liquid bio fuel in a fluidized bed. A pressure transducer was used to measure the fluidized bed pressure and the main furnace was equipped with a video camera to record events inside the bed surface. The experiments were conducted in order to verify that microexplosion temperature zone ranged from 600 to 700 °C. A Matlab code was used to simulate the microexplosion in the bed. The sequence of frames from the video and those from Matlab were compared. The pressure spikes were recorded at three different temperatures. The experiments revealed that average height of the spikes decreased with temperature. The author suggests that at above 800 °C the microexplosion occurrence ceased since the pressure signals smoothed out significantly. Also, pressure readings were taken both with and without fuel injection inside the boiler. It was revealed that microexplosion occurred at the bed surface at 650 °C and microexplosion inside the bed above 650 °C.

Wang and Law [19] investigated microexplosion under high pressure, up to 5 atm with water/oil emulsion droplets and multi-component droplets which consisted of mixtures of n-alkane (hexane, heptane, hexadecane and octadecane), and n-alcohol (dodecanol, methanol, ethanol, propane, or butanol). In the first set of experiments, the less volatile n-alkane with the more volatile n-alkane emulsion, the less volatile n-alkane with the more volatile n-alcohol emulsion, and water with diesel emulsion were used under different pressure and water concentration ratios. Most of the emulsions showed larger normalized droplet size (d_e/d_o) at higher pressures. Experimental results indicate

that microexplosion only occurs when the right ratio of components is used. The author [19] also concluded that increasing chamber pressure raised the possibility of microexplosion regardless of mixture type, unless they contain fuel components with similar volatilities.

Morozumi and Saito [20] studied the effects of emulsifiers on microexplosion phenomena by taking into account and measuring viscosity, the diameters of dispersed water droplets, microexplosion behavior, emulsion droplet temperature, and the interfacial tension between water and oil phases in n-hexadecane emulsions. In the experiments, 80 wt % of n-hexadecane and 20 wt % of water were mixed with two different compositions of non-ionic emulsifiers. Case A used only Solgen 40, and case B used a mixture of Solgen 40 and Noigen TDS-30. At a constant chamber temperature of 1073 K, 0.1 mm diameter R-type thermocouple wire was used to suspend the $1.5 - 1.8$ mm diameter droplets. A high speed camera recorded microexplosion events at a frequency of 1000 Hz. The results highlighted that the interfacial tension between water and n-hexadecane were lower for case B than for case A because the case B mixture surfactant gets adsorbed on both sides of the water-oil interface. Thus, as the amount of emulsifier increases, the interfacial tension decreases. However, above a certain amount of surfactant, interfacial tension remained almost constant. Water droplets were found to be well distributed in hexadecane, and coalescence was rarely found in case B due to the mixture of emulsifiers. In the microexplosion experiment, the author [20] discovered that a large content of emulsifier would have a negative influence on the microexplosion

occurrence due to the fact that microexplosion the chamber temperature and ignition time increase as the emulsifier contents increases.

2.4 Acoustic Emission

Acoustic emission (AE) is a phenomenon where elastic waves and sound waves are spontaneously generated by the rapid release of energy from sources such as mechanical loading and bombs [21]. Sound wave is a form of energy that pushes atoms closer together momentarily and moves through the atoms causing the region of compression to move forward. It is also referred to as stress wave, micro-seismic activity and rock noise.

AE is also used in nondestructive techniques [21]. In AE, the wave energy is released from the source rather than being generated by an acoustic sensor itself. AE can also be used to detect dynamic processes such as earthquake vibrations, crack growth and plastic deformation. Major examples of acoustic emission applications are monitoring of pressure vessels, detection of fatigue failures, monitoring materials behavior or resistance welds and stress corrosion cracking.

2.4.1 Acoustic Emission Testing Equipment

Acoustic Emission Sensors

The function of acoustic emission sensor is to convert an acoustic wave being propagated through the surface of the object into a specific electric signal [22]. For this reason, acoustic sensors are usually termed as transducers. Mostly, transducers use a

piezoelectric element for electro-mechanical conversion. The front face of a transducer consists of a thin disk of piezoelectric material connected to an electric conductor. The piezoelectric element disk is normally made of small crystals of Titanates and Zirconates mixed with other materials [22]. Figure 8 shows the setup inside the AE sensor.
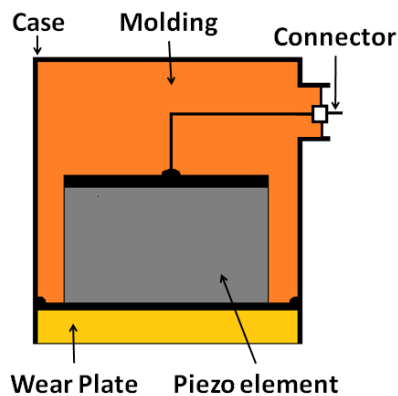
Figure 8. Schematic setup of an acoustic sensor [22].

To maximize the sensitivity of a piezoelectric transducer, it has to be attached to a flat surface of material for the acoustic energy to pass into the sensor with minimum loss. When attaching an AE sensor onto a surface, a coupling material such as grease, oil or epoxy adhesive to improve the transmission of the shear waves by removing any air from the interface between sensor and surface.

Preamplifier

The role of the preamplifier is to strengthen the incoming small electrical signal before it is transferred to the data acquisition system without a significant level of

degradation of the signal-to-noise ratio (SNR). SNR is defined as the ratio of signal power to the noise power. Equation (10) shows the equation of the SNR.

$$dB = 20 \log\left(\frac{V_{signal}}{V_{noise}}\right) \tag{10}$$

Most preamplifiers support 20 dB, 40 dB and 60 dB gain values, which amplifies ten times, hundred times and a thousand times of the wave signals, respectively.

2.5 Signal Processing

Signal processing is categorized into analog signal processing, discrete time signal processing and digital signal processing. Analog signal processing (ASP) consists of signals that have not been digitized. Digital signal processing (DSP) consists of discrete time signals, which are digitized by an analog-to-digital converter (ADC). The ADC converts the continuous analog signals to digital signals [23].

When digitizing signals, the sampling rate is the first step. Every discrete points of the signal are read in a periodic interval (T). The sampling frequency or sampling rate, f_s, is defined as

$$f_s = \frac{1}{T} \tag{11}$$

In the discretization and conversion of analog signals, it is important to consider the Nyquist-Shannon sampling theorem. It is the basis followed when discrete signals are reconstructed as uniformly sampled continuous-time signal. The theorem which is also

referred to as Nyquist sampling theorem states that a signal has to be sampled at least twice as fast as the highest frequency of the original signal [23]. If lower sampling frequencies are used, the resulting signal suffers from aliasing and become indistinguishable when sampled. Figure 9 shows sine curves which are sampled at three different rates. The sampling rate of Figures 9 (a) and 9 (b) is set as four times and twice the highest frequency of the original signal, respectively. The sine curve of Figures 9 (a) and (b) is distinguishable with the discrete signals at the given sampling rate. However, the discrete signals with a sampling rate 1.5 times as fast as the highest frequency in Figure 9 (c) is difficult to predict as sinusoidal.
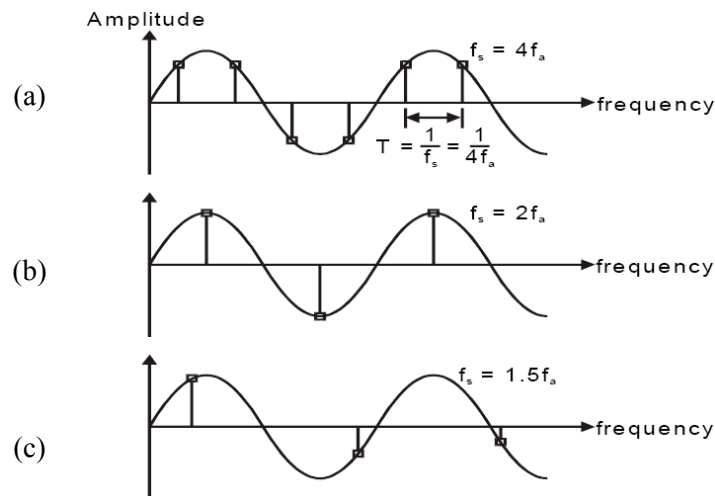
Figure 9. Sine waves at three different rates demonstrating the Nyquist frequency
(a) $f_s = 4f_a$, (b) $f_s = 2f_a$, (c) $f_s = 1.5f_a$ [24].

Another important consideration in signal processing is the selection of triggering points. Triggering points are the designated amplitude values that would trigger data

collection once they are exceeded. There are several types of triggering options in most digitizers including immediate triggering, hysteresis triggering, edge triggering, window triggering, and digital triggering. Basically, the trigger occurs when a signal crosses the trigger threshold set by users. The slope at the triggering point can be specified as either positive or negative.

Additionally, in digital signal processing several types of domains are used such as time domain, frequency domain, and wavelet domain. For microexplosion experiments requiring a sequence of signals from a digitizer, time domain approach is the most appropriate. Moreover, signals transformed through FFT require the use of a frequency domain [23].

2.5.1 Fast Fourier Transform

As part of signal processing of acoustic waves, Fast Fourier Transform (FFT) are routinely used to understand the physical attributes of the waves. FFT is basically a mathematical algorithm used to calculate the Discrete Fourier Transform (DFT) in an efficient manner [25]. DFT is based on a mathematical operation such as the Fourier transform which convert a signal into its constituent frequencies. Once Fourier transform is done, all the signals on the time domain are computed into signals on the frequency domain which help understands resonance frequency of each component.

Fourier analysis is possible with the study of Fourier series which begin with the sum of waves with trigonometric characteristics. Figure 10 shows two different waves (a

and b) with different frequencies but identical amplitude. In that case, they can be combined and analyzed as one wave as shown in Figure 10 (c).
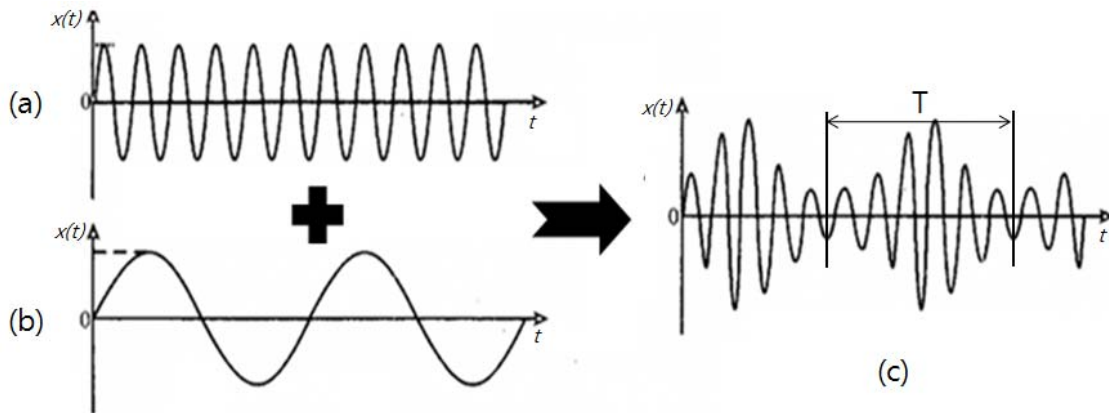
Figure 10. Wave combination and arbitrary periodic function of time [25]
(a) high frequency wave (b) low frequency wave (c) combined wave.

Infinite trigonometric waves or functions can be expressed using the following equation [25].

$$x(t) = a_0 + a_1 \cos\frac{2\pi t}{T} + a_2 \cos\frac{4\pi t}{T} + \cdots + b_1 \sin\frac{2\pi t}{T} + b_2 \sin\frac{4\pi t}{T} + \cdots \tag{12}$$

where, x(t) is a periodic function of time t with period T

Equation (12) can be also expressed as a Fourier series with Fourier coefficients as shown in Equation (13).

$$x(t) = a_0 + \sum_{k=1}^{\infty}\left(a_k \cos\frac{2\pi kt}{T} + b_k \sin\frac{2\pi kt}{T} \right) \tag{13}$$

where, $a_0 = \dfrac{1}{T} \displaystyle\int_{-T/2}^{T/2} x(t)dt$

$a_{\substack{k \\ k\geq 1}} = \dfrac{2}{T} \displaystyle\int_{-T/2}^{T/2} x(t)\cos\dfrac{2\pi kt}{T}dt$

$b_{\substack{k \\ k\geq 1}} = \dfrac{2}{T} \displaystyle\int_{-T/2}^{T/2} x(t)\sin\dfrac{2\pi kt}{T}dt$

It is customary to state vibration theory and FFT analysis in complex form to simplify data analysis. To convert Fourier transform into a complex form, the wave functions is expressed using the Euler equation (14), and converted into Fourier transform of X(ω) (15) as defined below. With the final Fourier integral Equation (16), frequency X(ω) can be calculated using time and angular frequency (ω) based on sampling frequency.

$$e^{i\theta} = \cos\theta + i\sin\theta \qquad\qquad (14)$$

$$X(\omega) = A(\omega) - iB(\omega) \qquad\qquad (15)$$

where, $A(\omega) = \dfrac{1}{2\pi} \displaystyle\int_{-\infty}^{\infty} x(t)\cos\omega t dt$

$B(\omega) = \dfrac{1}{2\pi} \displaystyle\int_{-\infty}^{\infty} x(t)\sin\omega t dt$

$\omega_k = \dfrac{2\pi k}{T}$

X(ω) is the Fourier transform of x(t)

A(ω) is an even function of ω

B(ω) is an odd function of ω

ω_k is the frequency of the kth harmonic

$$X(\omega) = \frac{1}{2\pi} \int_{-\infty}^{\infty} x(t)(\cos \omega t - i \sin \omega t)dt \tag{16}$$

$$X(\omega) = \frac{1}{2\pi} \int_{-\infty}^{\infty} x(t)e^{-i\omega t}dt \tag{17}$$

The Discrete Fourier Transforms (DFT) is based on the concept of a discrete time series as explained above. *x(t)* values are obtained periodically at a constant sampling rate through an analogue-to-digital converter. Figure 11 [25] shows the discrete values of *x(t)* are obtained at certain fixed intervals of time *(t)*.
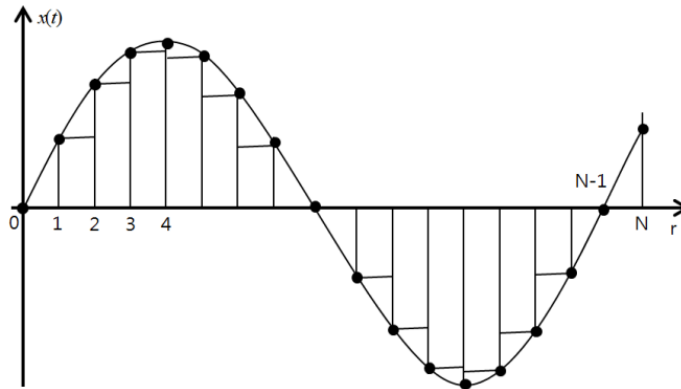
Figure 11. Sampling a continuous function of time at regular intervals [25].

The DFT of the discrete Fourier series *x(r)*, r = 0,1,2…,(N-1) can be defined using the following equation.

$$X_k = \frac{1}{N} \sum_{r=0}^{N-1} x_r e^{-i(2\pi kr/N)} \tag{18}$$

where, $k = 0,1,2,...,(N-1)$

An already developed computer algorithm can generate the Discrete Fourier Transforms (DFT) from the Fast Fourier Transform using as basis Equation (18). The finite number of data points in DFT can be processed efficiently and effectively with a FFT algorithm. It needs N^2 multiplications to get X_k by a direct approach because it has to calculate N multiplications of $(x_r) \times (e^{-i(2\pi kr/N)})$ for each of N. However, FFT reduces the number processes by an order $N\log_2 N$. The authors [25] gives an example of $N = 2^{15}$, with the number of FFT operations to be about $1/2000^{th}$ less than that of DFT operations. Therefore the algorithm reduces computer processing time and increasing the accuracy due to fewer operations.

2.6 Numerical Study of Microexplosion Strength

The explosion dynamics of a liquid droplet was numerically studied to understand the strength of microexplosion process. A relationship between microexplosion strength and natural frequency was obtained using a partial differential equation explained later in section 4.10.

Fu et al. [26] proposed a general model of the microexplosion in water-in-oil and emulsified droplets taking into account microexplosion strength. Also, the effects of various parameters on microexplosion strength were studied. To get a numerical equation of microexplosion strength, surface tension (γ) was ignored because it decreases considerably with temperature and with emulsifier concentration.

A definition of microexplosion strength K is shown in Equation (19) in terms of volume fraction of water, total mass of droplet, bubble nucleation rate, and droplet diameters [26].

$$K = \int_0^{R_1} \left(4\pi r^2 \phi J\right) M dr \qquad (19)$$

where, $M = 4/3\pi\left(R_0^3 - r^3\right)\rho$ is the total mass of droplet including oil and water [kg]

J is the bubble nucleation rate [$1/m^3 s^1$]

ø is volume fraction of water in an emulsified oil

R_0 is the initial radius of emulsion droplet [m]

R_1 is the radius of emulsion kernel when oil membrane is formed [m]

The homogenous nucleation theory [27] explains that the nucleation rate, J, of liquid undergoing phase change happens very rapidly at high temperatures, as shown in Equation (20). An abrupt growth rate of nucleation can be induced at superheat limit.

$$J = n_T \frac{kT}{h} \exp\left(-\frac{4\pi r_{cr}^2 \gamma}{3kT}\right) \qquad (20)$$

where, k is Boltzmann's constant (1.3808 $\times 10^{-23}$ J/K)

h is Plank's constant (6.6261$\times 10^{-34}$ J·s)

r_{cr} is the critical diameter of a vapor embryo (m)

γ is surface tension (kg/s^{-2})

n_T is the number of potential nucleation sites per unit volume

Fu et al. [26] found out that there is optimal amount of water content for maximum strength of the microexplosion process and it is proportional to initial droplet diameter. The probability of microexplosion depends on ambient temperature and pressure. Microexplosion rate increases with temperature.

2.7 Pencil Lead Break Test

Hsu-Nielsen source [28] or pencil lead break is used to simulate acoustic emission signals using the breakage of a graphite lead as shown in Figure 12. A 0.5 mm (or 0.3 mm) diameter pencil lead of approximately 3 mm length from its tip is broken by pressing it against a hard surface. This generates an intense or shock acoustic emission signals. The test is generally performed before microexplosion experiments to check the performance of the transducers. Also, it can be used to determine acoustic wave velocity and attenuation, as well as the accuracy of the source location setup.
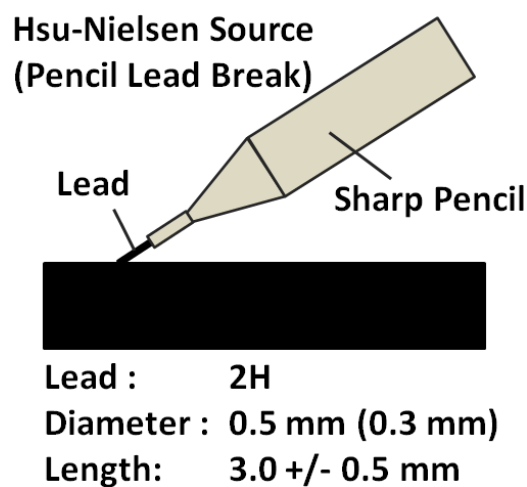
Figure 12. Schematic of pencil lead break test [28].

Yu et al. [29] used the pencil lead break test before and after each loading test to check the performance of the transducers and to generate reference noise waveforms from cracking of a pencil lead. This method has been used by Vallen [30] to determine the thickness and harness of a vessel. The test is used to determine the maximum distance that a sensor can detect an acoustic signal.

2.8 Past Research on Microexplosion Detection by Acoustic Sensors

In 2005, Yamasaki et al. [31] conducted an experiment to obtain the characteristics of microexplosion phenomena of a single droplet emulsion by using an acoustic emission sensor. The emulsion was made of 20 vol. % of n-hexadecane and 80 vol. % of water. Video camera captured the microexplosion events taking place at the tip of the quartz fiber stick. The sampling rate of the acoustic sensor was set at 0.2 MHz. Internal boiling and microexplosion phenomena were identified using high speed images and acoustic waves. The acoustic wave showed that puffing had higher amplitude than the section of wave corresponding to the microexplosion process. Right after the microexplosion had taken places, no more waves could be detected by the acoustic emission sensor. The acoustic wave prior to microexplosion process occurred mainly due to the droplet internal boiling and puffing phenomena. Under the same conditions, pure n-hexadecane droplets could not generate microexplosive wave amplitude as the one identified using the emulsion.

Tanaka et al. [32] studied the secondary atomization of droplets made of 70 % of n-tetradecane with 30 % of water, and 80 % of n-hexadecane with 20 % of water. The secondary atomization was classified as microexplosion and puffing after examining the

images collect using a high speed camera and a sound sensor (microphone). The author

tested a Birchley-Riley [33] emulsion and a W/O emulsion as shown in Figure 13.
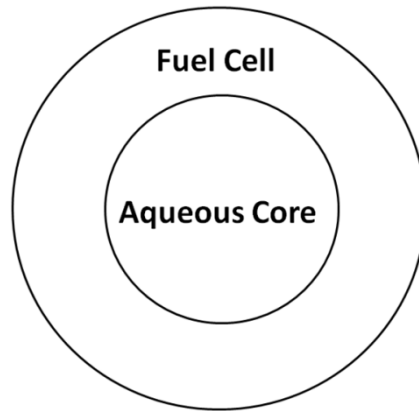
Figure 13. Fuel droplet of Birchely-Riley model [33].

The B-R emulsion droplet consists of a water core surrounded by a fuel shell under

high temperature. Both types of emulsions showed similar sound waves when

microexplosion took a place. In each case, the wave amplitude increased abruptly

decreased considerably at the onset of microexplosion. However, wave changes

corresponding to the puffing phenomena could not be detected due to the type of

instrumentation used. During puffing, droplets swell much more than when droplets

microexplode. The author also analyzed the wave signals using the Fast Fourier

Transform algorithm with both B-R and W/O emulsion droplets. The frequency spectrum

of microexplosion was characterized by increases in sound pressure levels all along the

frequency axis from 0 – 20 kHz. However, the frequency spectrum of puffing showed

reduced sound levels from over 2 kHz – 20 kHz. Regardless of the type of emulsion (B-R

type and normal W/O), sound waves depict similar behavior when microexplosion occurred.

3. OBJECTIVES AND TASKS

The overall objective of the research project was to understand the effect of droplet emulsion composition, initial droplet size and chamber temperature on the breakup characteristics of microexplosion phenomena. An experimental apparatus was put together using a high speed camera and an acoustic sensor for recording high speed images and sampling acoustic waves due to microexplosion, respectively. In order to meet the objectives, the following tasks were undertaken.

1. Make stable methanol-in-canola oil emulsions having 2 different compositions [6] including water-in-canola oil emulsion [34] and hexadecane-in-water emulsion [35]. Table 5 shows the composition of emulsions.

Table 5. Composition of emulsions.

Abbreviated Name	Full Name	Base Fluid	Secondary Fluid	Surfactant (w/w)
CM 90/10 [6]	Methanol-in-canola	89 % Canola oil	9 % Methanol	2 % of surfactant
CM 85/15 [6]	Methanol-in-canola	85 % Canola oil	12.5 % Methanol	2 % of surfactant
CW 90/10 [34]	Water-in-canola	87.5 % Canola oil	7.5 % Water	5 % of surfactant
HW 20/80 [35]	Hexadecane-in-water	19 % n-Hexadecane	79 % Water	2 % of surfactant

2. Design and build a custom-made electric furnace to be able to control the chamber temperature up to 1000 ˚C. Install a digitally controlled, temperature controlled linear actuator to insert a single droplet into the high temperature chamber.

3. Synchronize the high speed camera and acoustic sensors using a NI-USB DAQ board to obtain images and acoustic data at the same time.

4. Develop a Labview program to control the acoustic sensor and preamplifier. Develop a Matlab program (see APPENDIX B) for complete FFT analysis of the microexplosive wave signals to understand the microexplosion characteristics.

5. Validate the acoustic experimental setup by comparing the microexplosion wave signals of hexadecane-in-water emulsion with the previously published data [31].

6. Perform single droplet experiments following the conditions shown in Table 6. Obtain wave signals and images of microexplosion phenomena of the fuel emulsions droplets.

Table 6: Input variables.

Temp.	Emulsion Type	Droplet Sizes
(900 ˚C)	CM 90/10	Average initial droplet size for each emulsion condition i) 224 μm (±9 μm) ii) 304 μm (±9 μm)
	CM 85/15	
	CW 90/10	
(980 ˚C)	CM 90/10	
	CM 85/15	
	CW 90/10	
(730 ˚C)	HW 20/80	

4. EXPERIMENTAL SET-UP

This section describes the details of the experimental facility and instrumentation used for detecting microexplosion. The experimental set up was designed and assembled to be able to detect microexplosive wave signals, and capture images of microexplosion. Software programs such as Labview and Matlab were used for recording and analyzing the acoustic signals capture by the acoustic sensor. Figures 14 and 15 depict the overall experimental setup for this research project. The experimental set up was based on the Yamasaki's experimental system [31] which is depicted in Figure 16. By using the Yamasaki's set up as reference, it was possible to compare their hexadecane emulsion microexplosion results with the ones generated as part of this project.
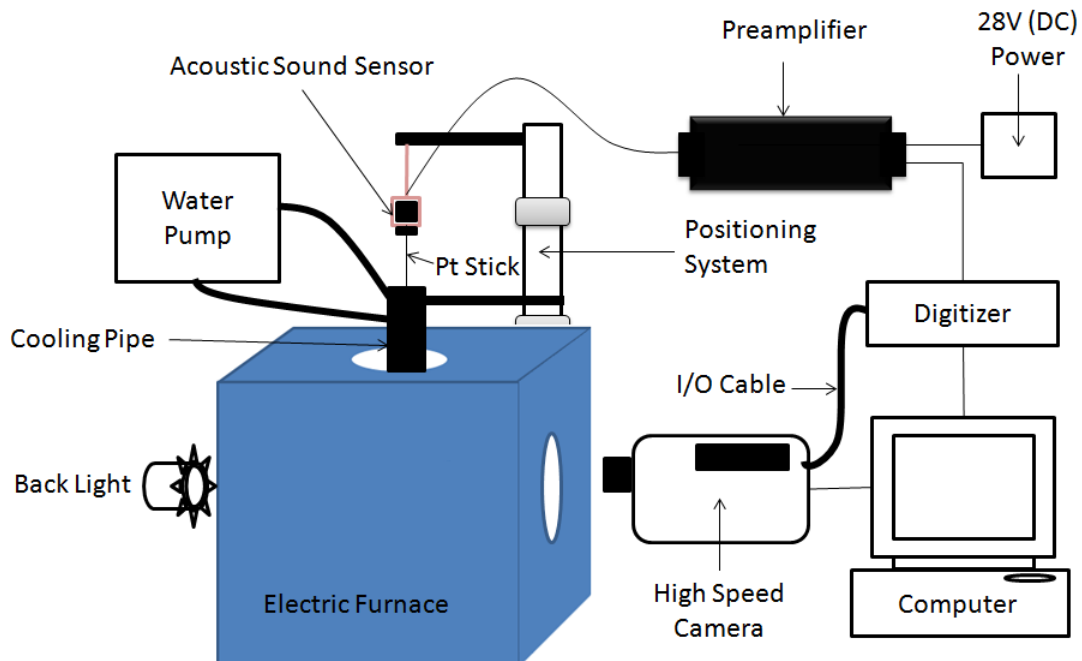
Figure 14. Overall experiment setup for this research I.
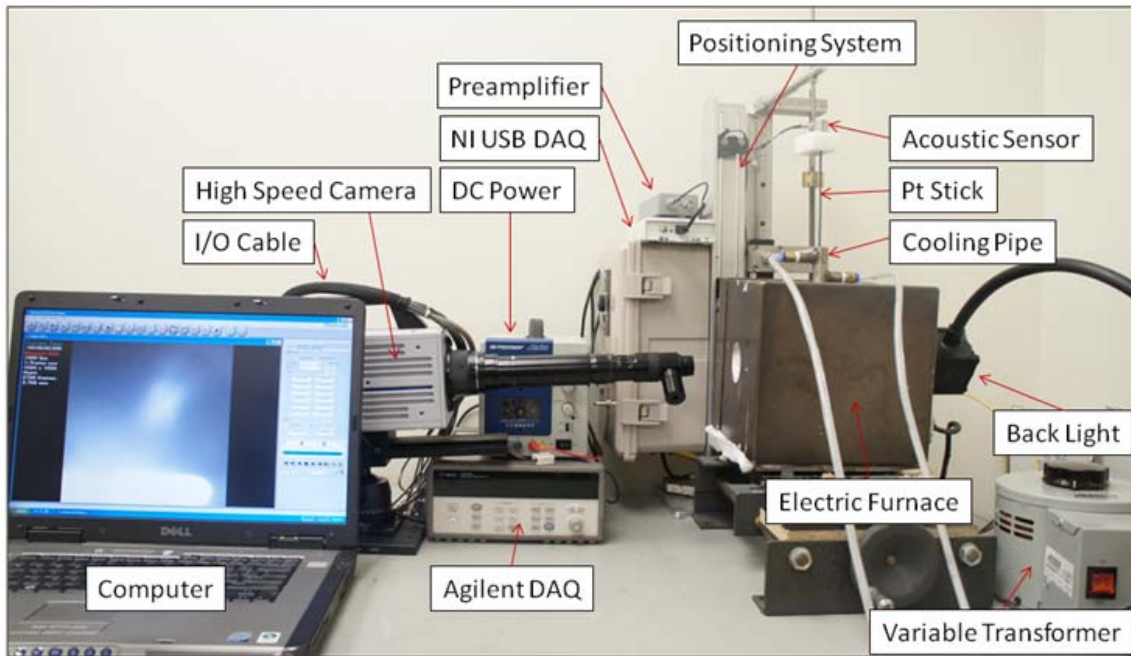
Figure 15. Experimental setup for this research II.
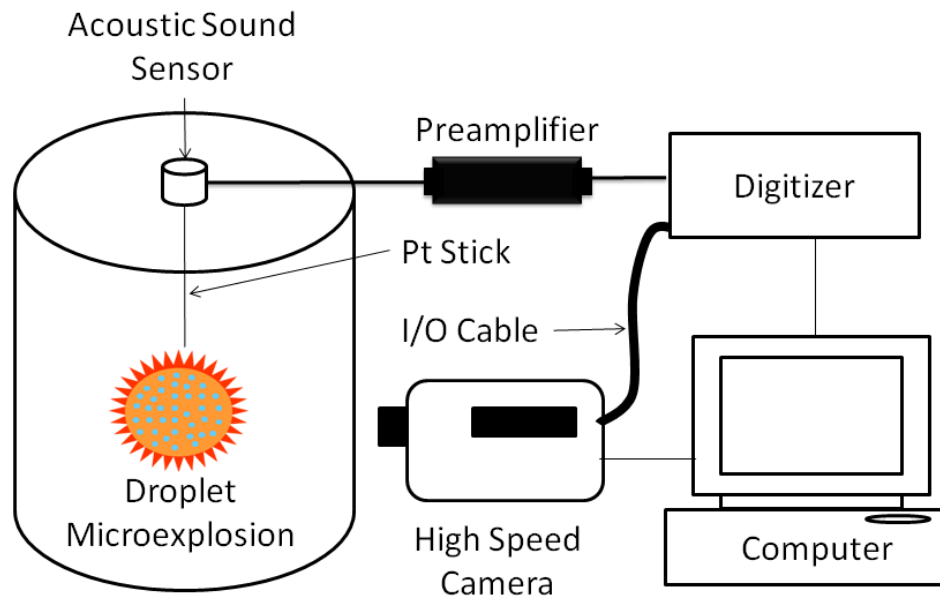
Figure 16. Experimental setup for verifying the acoustic system.

4.1 Acoustic Sensor Devices

An acoustic sensor system was used for obtaining and translating acoustic waves generated by the microexplosion process. The waves were transmitted using a Pt stick attached to an acoustic sensor. All of acoustic waves were collected using a NI DAQ which was transferred to a data analyzer. Figure 17 shows the schematic of the acoustic sensor system.
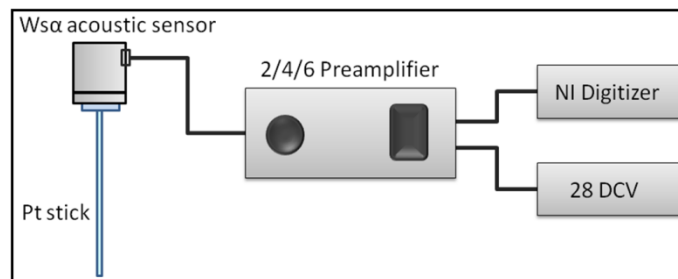
Figure 17. Schematic of acoustic sensor system.

4.1.1 Ws-alpha Acoustic Sensor and Preamplifier

The acoustic sensor was a single-ended and a broadband acoustic emission WSα sensor with reasonable flat response of about 1.0 MHz. It was purchased from Mistras (Physical Acoustic Corporation), USA. The sensor came with a 2/4/6C preamplifier that was used to amplify the power of signals by 20 dB, 40 dB and 60 dB. The preamplifier was connected to a 28 V (DC) variable transformer and operated with a single ended sensor or differential sensor. The Wsα Sensor and 2/4/6C preamplifier are shown in Figure 18.

(a)   (b)

Figure 18. (a) WSα sensor and (b) 2/4/6C preamplifier.

4.1.2 Pt Stick

Pt Stick was used to serve as a medium to transfer acoustic waves caused by the microexplosion of droplets to a NI digitizer. Platinum (Pt) was chosen because it has a melting point of 1700 ˚C and can endure severe and high temperature conditions inside the custom-made electric furnace. The Pt wire with a diameter of 25.4 μm was purchased from A-M Systems was attached to the tip of the Pt stick which has a diameter of 1 mm, by using a high temperature ceramic adhesive. The purpose of using the Pt wire was for suspending and holding a micro-sized emulsion droplet in the range of 150 μm to 350 μm. On the opposite side of Pt wire, a 10 mm diameter circular plate was attached to face of the Wsα sensor as shown in Figure 19.

Figure 19. Pt stick.

A National Instrument Data Acquisition digitizer was used for collecting acoustic wave data. The eight-bit digitizer featured 50 MS/s sampling rates on two simultaneously sampled channels. The PFI (programmable Function Interface) port was utilized for connecting I/O port cable to transfer a trigger pulse. A 8 MB onboard memory was used to acquire and store the data. A plug-and-play type USB digitizer allowed maximum portability and flexibility during the experiments

4.1.3 Labview Coding

A Labview code was developed for the NI USB 5132 digitizer using the niScope library. Figure 20 shows the front panel window or computer screen which includes two graphs, one for acoustic wave signal, and the other for the FFT spectrum. An input parameter box was also used to control the equipment through the software. For the configuration setups, sampling rate was set as 1 MHz because the expected frequencies was from 0 to 0.5 MHz on the basis of the Nyquist sampling theorem that states sampling rate need to be set at least twice as fast as the highest frequency of the original signal to avoid signal aliasing [23]. After setting the sampling rate, the record length was set as 3,000,000 to measure the signals for at least 3 minutes. An edge triggering option was of 200 mV threshold at the positive slope was used as sampling criterion. Table 7 shows the NI Vis' names (NI code symbols), icons, and short descriptions, which were used for writing the operation program.
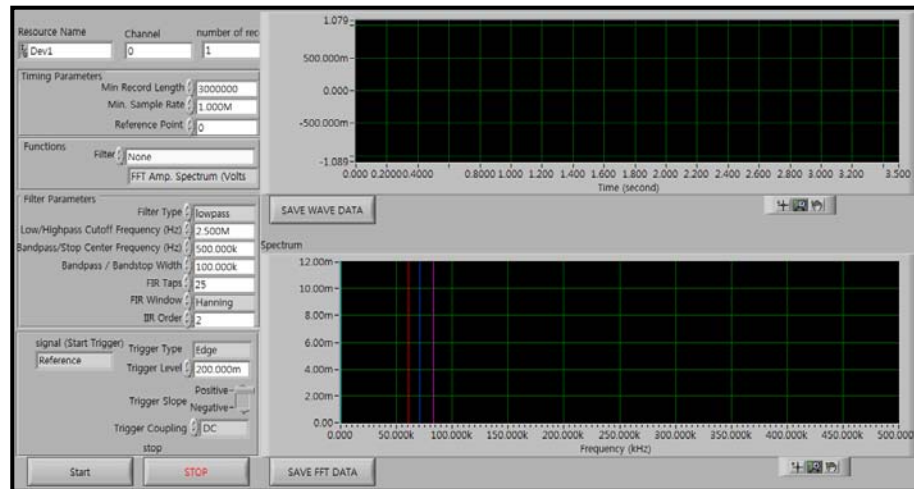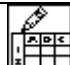
Figure 20. Labview front panel.

Table 7. Used niScope VIs for the operation program.

	Vis	Icon	Description
1	niScope Initialize.vi		Opens a session to the digitizer
2	niScope Configure Vertical.vi		Configures the vertical parameters such as input range, offset and coupling
3	niScope Configure Horizontal Timing.vi		Configures the horizontal parameters such as sampling rate and number of samples to acquire
4	niScope Add Waveform Processing.vi		Adds the user requested filter process before calculating any of the array measurements
5	niScope Configure Trigger Edge.vi		Configures common properties for edge triggering
6	niScope Initiate Acquisition.vi		Initiates a new acquisition
7	niScope Multi Fetch Array Measurement.vi		Shows the filtered data and applies an FFT to the filtered data and displays the results
8	niScope Clear Waveform.vi		Clears the filter process
9	niScope closing.vi		Closes the session and displays any errors that might have occurred
10	Write to File.vi		Saves the data
11	Simple Error Handler.vi		Indicates whether an error has occurred

4.2 High Speed Camera

A FASTCAM SA3 high speed camera purchased from Photron was used for recording images of the microexplosion phenomena. The high speed camera was used since microexplosion happens in milli-seconds. The camera was able to record images at 1000 Hz with a resolution of 1024 x 1024 pixels, and up to 60,000 Hz at a reduced resolution of 128 x 16 pixels. Since the camera was able to provide exceptional light sensitivity, image quality and color fidelity. A shutter speed control option was used in combination with a strong backlight. A 1.5X magnification of the camera was used for all experiments.

Additionally, an I/O port cable was purchased from Digital West Imaging to synchronize the high speed camera with the acoustic sensor system to make sure that acoustic waves could be matched with the high speed images. The General In port of the cable was used to connect to PFI port of the NI USB digitizer in the acoustic sensor system.

4.3 System Synchronization

Synchronization of the high speed camera and acoustic sensor were undertaken to fully understand the characteristics of acoustic waves produced by microexplosion. First, all of the input values such as sampling rate, the record length, the reference position and the trigger level for the acoustic sensor system were set also, the frame rate and shutter speed of the high speed camera were set and the I/O port cable was connected to camera. Using the Labview operation program, the 'Initiate Acquisition' function was activated to

start getting acoustic waves through the digitizer. The digitizer was used to store data onto the circular 8 MB onboard memory while the high speed camera waited for the trigger pulse from the digitizer. Once the sampling waves exceeded the threshold trigger level set by users, the system activated the digitizer to save the exact number of data points. At the same time, the high speed camera was simultaneously activated to capture the exact number of images based on an established value. Then, the sampled wave data and images were transferred from the equipment to the computer. Figure 21 explains how the synchronization process works in both systems.
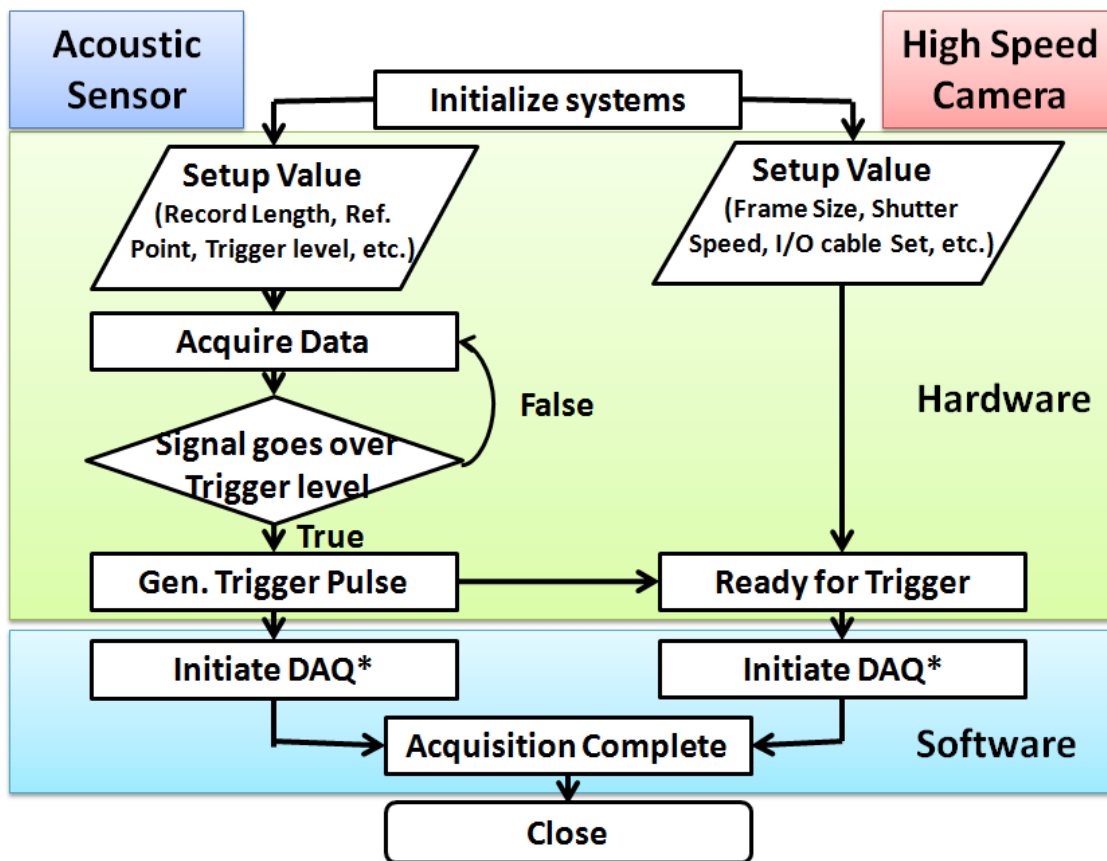
Figure 21. Synchronization of acoustic and high speed imaging systems.

Synchronization of the sound sensor with the high speed camera was undertaken using the pencil lead break method. The wave signals and the synchronized high speed images were recorded simultaneously. Figures 22 and 23 show two pencil lead strikes on an iron plate. With the triggering setting option set on both the acoustic sensor system and the high speed camera, the video started capturing images as soon as the first strike was hit on the plate. The second wave signal was propagated and recorded once the surface was struck a second time, and the wave signals and images were recorded simultaneously. The pencil lead test confirmed that the high speed camera and acoustic sensor system were less than 1 millisecond apart, indicating that observations made with the high speed camera could be correlated with the wave signals.
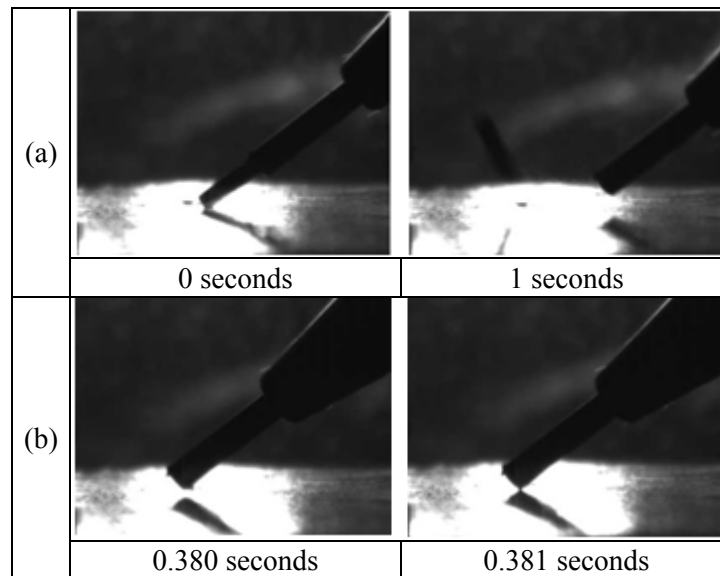
Figure 22. Images of pencil lead breakage used for the system synchronization (a) first strike (b) second strike.
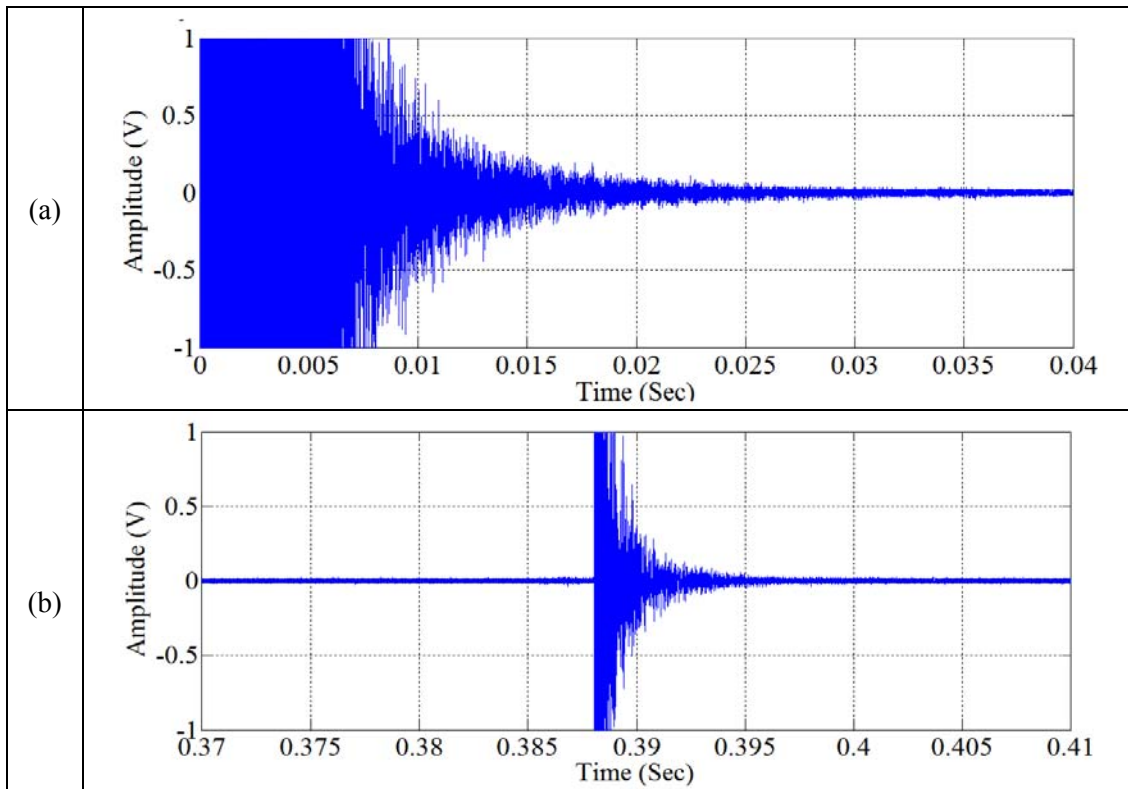
Figure 23. Waveform of synchronization test (a) first strike (b) second strike.

4.4 Custom-made Electric Furnace

A cubic type electric furnace was designed and built for this research work. It was made from four flat iron plates and two cover iron plates of 2 mm in thickness. Dimensions of the four flat iron plates were 210 mm × 205 mm, and that of two cover iron plates were 220 mm × 215 mm × 40 mm. The two plates had 53 mm holes each on center so the high speed camera and backlight could be used to image the process within the furnace. The holes were blocked with an extreme temperature quartz pure glasses which can stand up to 1150 ˚C. One cover plate had 28 mm hole on center for inserting the cooling pipe with the Pt stick inside of it. In the other cover plate, a 1 mm hole was made

for inserting a K-type thermocouple in the chamber. Inside the furnace, all the walls were plastered with high-temperature cement. The walls had a thickness of 20 mm to insulate the chamber. Spacers were placed for holding the electric wires used to power the heating elements located inside the chamber. Ceramic insulation fiber was used since it could endure up to 1300 ˚C.

Selection of the heating element was based on calculations used for the design of electric ovens. The inner furnace volume was used to determine the length and diameter of heating coils using a design chart as depicted in Figure 24. The chart shows the relation between the furnace inner volume and wattages needed to reach furnace temperatures up to 900 ˚C [36]. Since the inner volume was about 1000 cm^3 (61 $inch^3$), a 730 watt system was chosen to make sure that the temperature inside could go up to 900 ˚C. However, the system was designed for temperatures as high as 1000 ˚C to ensure the best conditions for microexplosion. In order to achieve such high temperature, thicker heating wire (Kanthal 20 gage) with a resistivity of 2.16 Ohms/m with a total length of about 3 m was used. The chamber was able to reach very high temperatures with less energy because it was able to retain a substantial amount of heat due to the effectiveness of the ceramic insulation fiber inside the furnace.
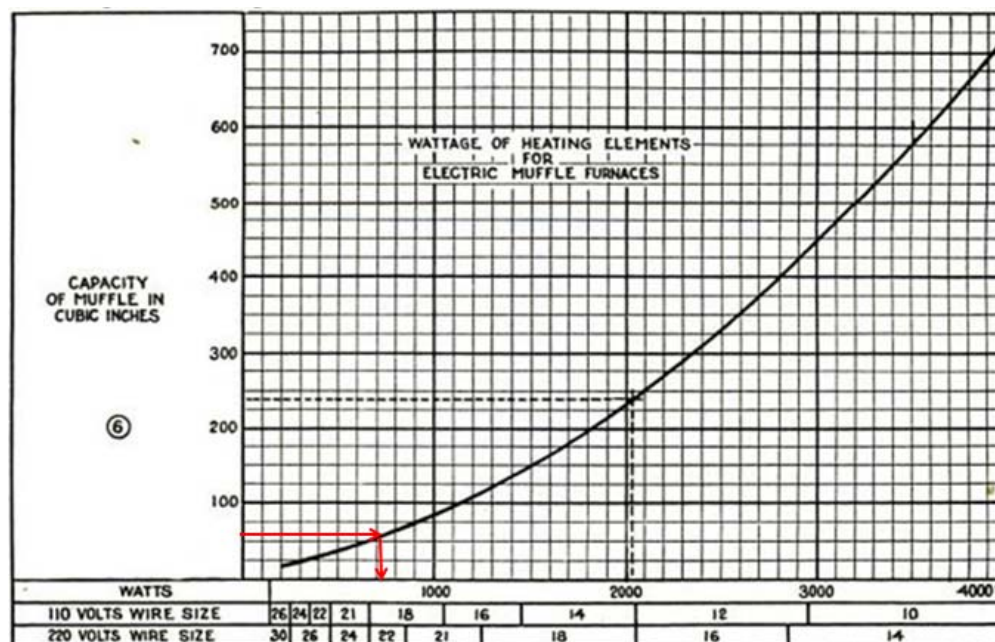
Figure 24. Wattage of heating elements for electric furnaces to increase up to 900 ˚C [36].

The electric furnace was tested to know specifically the wattage required for each furnace temperature. The furnace temperature gradients were recorded when a water-cooled pipe was inserted into the chamber. The purpose of the water-cooled pipe was to be able to bring small fuel droplets into the center of the chamber while minimizing fuel evaporation and keeping the droplet cooled. The water-cooled pipe consist of a water jacket where water flows at a rate of 1.68 ml/s. Figures 25 and 26 show the temperature gradient in furnace chamber with and without cooling pipe inside. 858 watts (7.4 Amps and 116 Volts) of power was able to increase the furnace temperature to 900 ˚C when there was no cooling pipe in the furnace. Also, 686 watts (6.6 Amps and 104 Volts) and 478 watts (5.5 Amps and 87 Volts) watts were required to reach 800 ˚C and 700 ˚C inside the chamber, respectively.
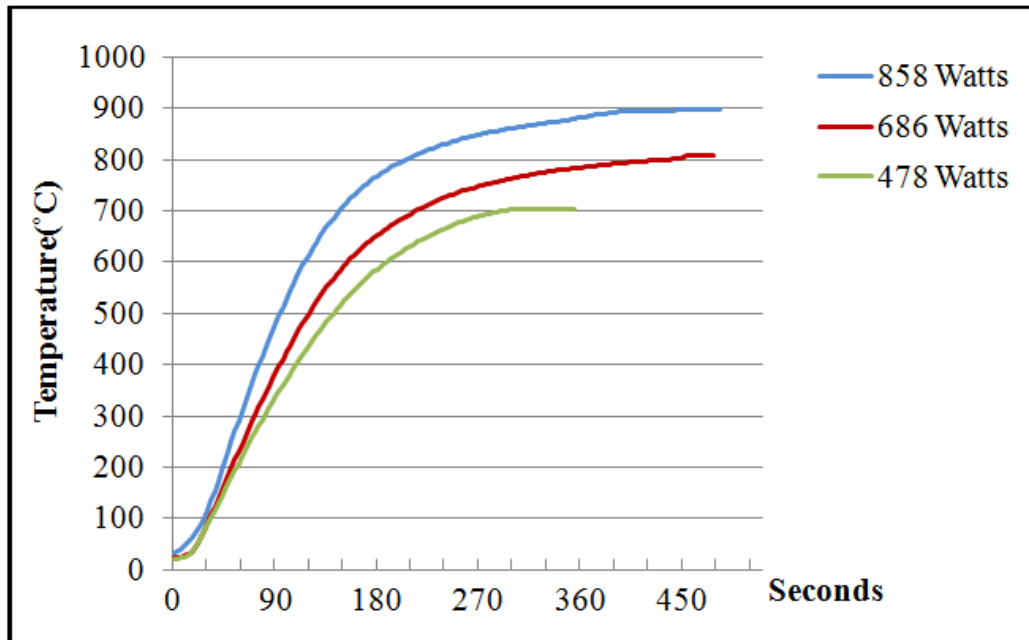
Figure 25 Temperature gradient of the electric furnace with cooling pipe.
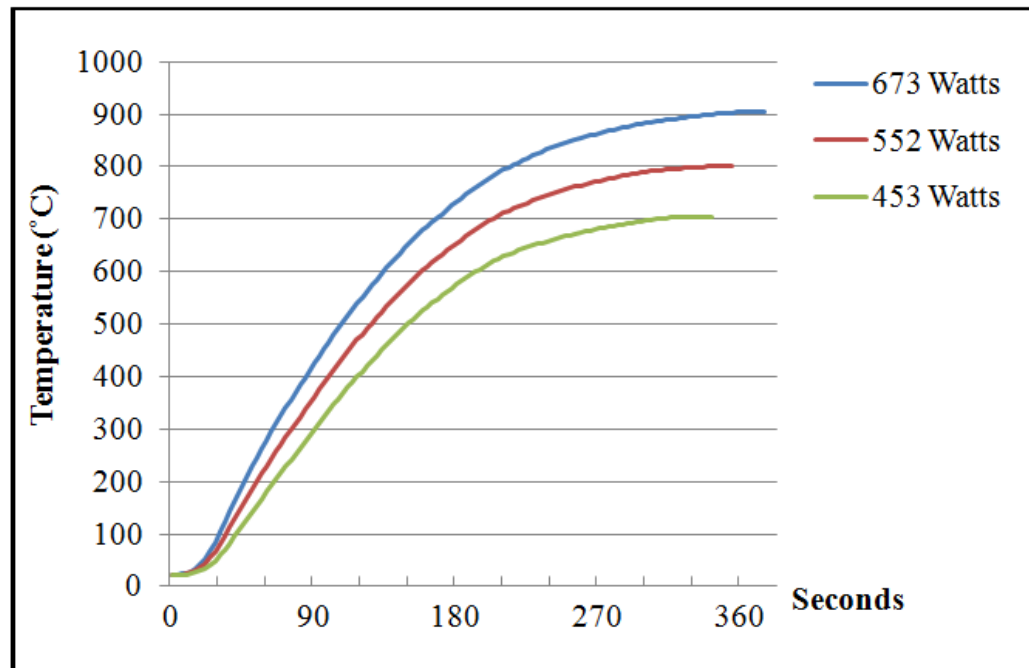
Figure 26 Temperature gradient of the electric furnace without cooling pipe.

4.5 Cooling Pipe and the Positioning System

A positioning system was developed to help guide the cooling pipe into the oven at a controlled speed. The chiller or cooling pipe also had to minimize the effects of environmental noise on the acoustic sensing equipment. A schematic representation of the positioning system and detailed drawing of connection part of AE sensor are shown in Figures 27 (a) and (b), respectively.
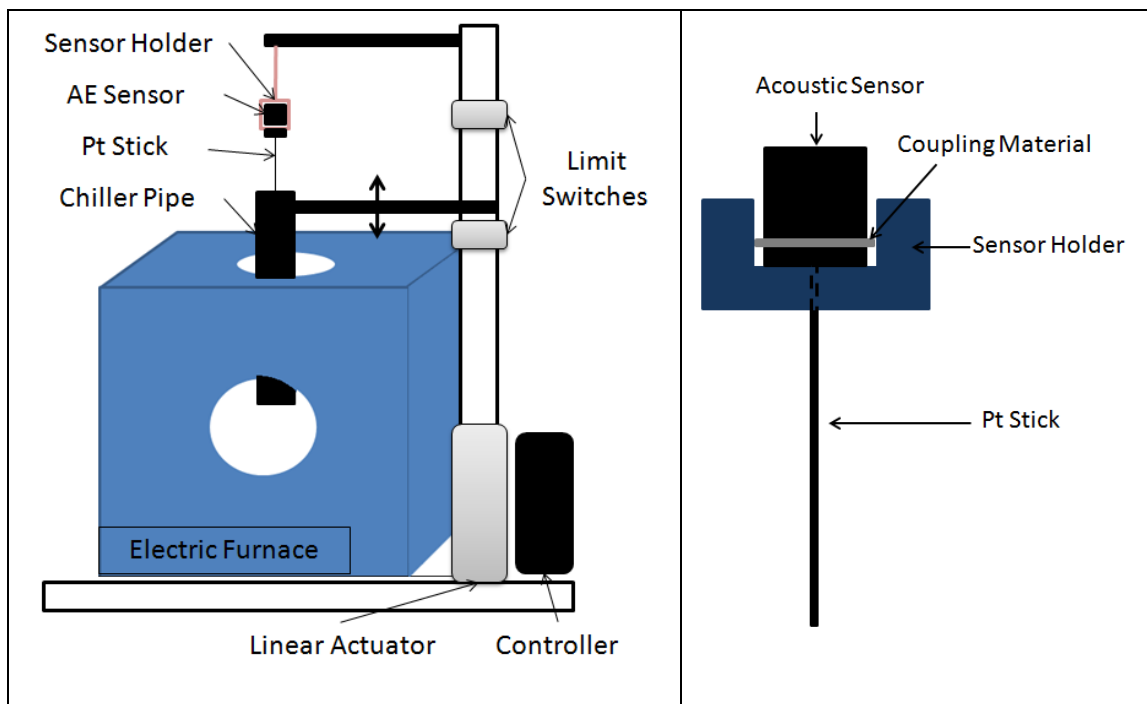
Figure 27. (a) Schematic of cooling pipe and supportive facility (b) detailed drawing of connection part of AE sensor and Pt stick.

The cooling pipe was operated using a linear motor. The pipe was especially designed for protecting a single emulsion droplet from the furnace heat while it was being lowered into its center. Figure 28 depicts the cooling pipe used for the experiments. The

outer pipe was made of inconel that can endure conditions above 1300 ˚C. The inner pipe was made of iron. The main tube had an external and internal diameter of 18 mm and 7 mm.

Figure 28. Cooling pipe.

A digitally controlled motor and speed controller were used to control the position of the cooling pipe. Both items were purchased from DKM Motor Co. The equipment was used for moving the cooling pipe at a constant speed. The range speed of the motor was from 100 to 1750 RPM. The linear motor was connected to the speed control box. Additionally, limit switches were used to for stopping the cooling pipe when it reached a certain position.

4.5.1 Role of Cooling Pipe

After each droplet was inserted into water-cooling pipe, the water-cooling tube was used to prevent the droplet from excessive heat flux from inside the chamber. It

allowed sufficient time to image the droplet before each droplet either expanded or microexploded inside the chamber. To start the experiment, the water-cooling pipe was quickly removed to expose the droplet to the inside of the high temperature chamber. As soon as the pipe was removed, the pipe itself generated some noise which was used to trigger both the acoustic and imaging systems. Figure 29 shows the water-cooling pipe before and after the droplet was exposed to high temperature.
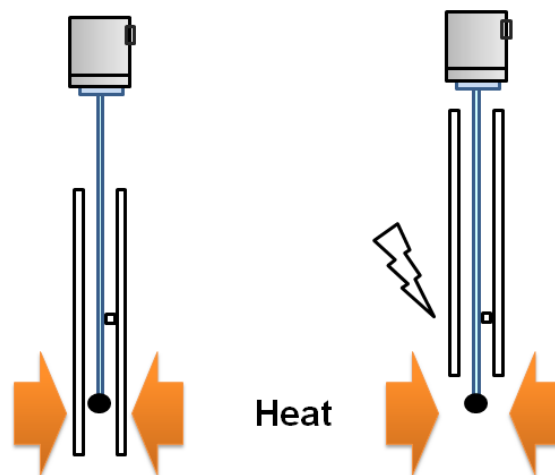
Figure 29. Purpose of the water-cooling pipe.

4.6 Agilent Data Acquisition System for Temperature Measurements

A type K thermocouple was used to measure temperature inside the electric furnace. A data acquisition (DAQ) system from Agilent Technologies was used to record temperature data using a computer. Temperature data were recorded at an interval of 2 seconds.

4.7 Emulsion Preparation

Three different oil emulsions were made for this research. 99 % Hexadecane of Sigma-Aldrich, 100 % pure Wesson canola oil, 99.99 % concentrated methanol of EMD bioscience and distilled water were used to make emulsified fuel with surfactants such as Tween 20, Tween 80 and Span 80 purchased from Sigma-Aldrich, USA. The hexadecane emulsions were made to validate the Yamasaki's experiments and findings [31]. Table 8 shows the properties of the secondary fluids such as water and methanol. Three additional emulsions were prepared as shown in Table 9.

Table 8. Properties of secondary fluids.

Chemical and Physical Properties	Water	Methanol
Molecular Formula	H_2O	CH_4O
Viscosity [Pa-sec] at 20˚C	0.001	0.00059
Boiling Point [˚C]	100	65
Heat of Vaporization [kg/kg] at 25˚C	2257	1100
Surface Tension [dyne/cm]	72	22.6
Vapor Pressure [kPa] at 25˚C	3.17	16.9

Table 9. Emulsion information used for this research on weight basis.

Emulsion Name	Base Fluid	Secondary Fluid	Surfactant (w/w)
HW 20/80 [35]	19 % n-Hexadecane	79 % Water	2 % of Tween 20
CM 90/10 [6]	89 % Canola oil	9 % Methanol	2 % of surfactant (75 % Span80+25 %Tween 80)
CM 85/15 [6]	85 % Canola oil	12.5 % Methanol	2 % of surfactant (75 % Span80 + 25 %Tween80)
CW 90/10 [34]	87.5 % Canola oil	7.5 % Water	5 % of surfactant (75 %Span 80 + 25%Tween 80)

Secondary fluids of water and methanol were used to compare the different effects on the microexplosion phenomena. One of the benefits of water as secondary fuel is that it has a higher latent heat of vaporization than methanol. Also, when water is used a secondary fluid, the combustion flame temperature decreases, which helps reduce the formation of thermal NO_x. On the other hand, methanol as a secondary fluid is a fuel that has a positive heating value (i.e. methanol is exothermic, while water is endothermic). It has been observed that greater concentrations of methanol in emulsions decrease the amount of NOx, UHC and CO emissions under combustion [6].

N. Kaneko et al. [35] describes the process of making n-hexadecane-in-water emulsion which was also used by Yamasaki [31]. The authors [35] used Tween 20 with a HLB number of 16.7 to blend the base and secondary liquids. The HLB number is used to predetermine the level of solubility of the secondary fluid into the primary fluid. Fluids with high HLB number tend to be more soluble in water. It is also common to use two different surfactants to be able to mix two water-insoluble oils in water. The right amounts of hydrophilic and hydrophobic surfactants were found by trial and error and using the formula defined by Mollet and Grubenmann [1].

$$\%(A) = \frac{100 \cdot (X - HLB_B)}{HLB_A - HLB_B} \tag{21}$$

$$\%(B) = 100 - \%(A) \tag{22}$$

where, A and B are mass fractions of two immiscible fluids

X is the HLB value of the desired emulsion

Morais et al. [34] proposed that the HLB number of a mixture of surfactants should be equal to the host liquid's HLB value to ensure proper mixing of the two phases. The author [34] suggested 5.0 % of surfactants including 25 % of Tween 80 and 75 % of Span 80 (w/w) to mix the canola oil in water. The percentage was calculated based on the canola oil's HLB value which about 7.0 is [37]. The HLB value of the surfactants was 4.3 for Span 80, and 15.0 for Tween 80. With the formula given above, 25 % of Tween 80 and 75 % of Span 80 (w/w) were used to make the emulsions. In the canola oil-methanol emulsion, a 2 % concentration of surfactants was enough to ensure stability [6].

The following was the procedure used for making 19 % Hexadecane-in-89 % water emulsion:

1. 39.88 g (40 ml) water was put in a beaker.

2. 2 % surfactant (0.952 g of Tween 20) based on a total weight of water and hexadecane of 47.61 g (50 ml), respectively were added to the beaker.

3. The hexadecane and the surfactant were mixed for 2 minutes using a mechanical blender to distribute the surfactant consistently in hexadecane.

4. 7.73 g (10 ml) of hexadecane was added to the beaker and blended for 15 minutes using a mechanical blender. Total weight of 79 % water − 19 % hexadecane emulsion was 48.56 g (51.05 ml).

5. After making the blend, the emulsion was dispensed into vials to check for stability. The emulsions were checked on an hourly basis to determine if the emulsions fluids separated into two phases. Figure 30 shows the hexadecane

emulsion after 10 minutes and 50 hours, respectively. The hexadecane

emulsion was very stable and took more than 3 days to separate out.

(a)   (b)
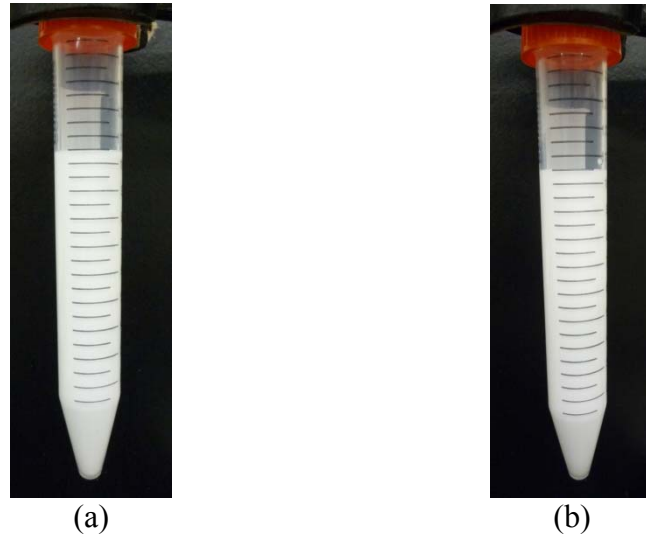
Figure 30. (a) Hexadecane emulsion after ten minutes (b) after 50 hours.

The same blending method was used to make water-in-canola oil emulsions and

methanol-in-canola oil emulsions. To make the water-in-canola oil emulsion, 43.30 g (45

ml) of canola oil was mixed with 4.985 g (5 ml) of water in addition to 5 % surfactants as

per the weight basis used by Morais et al. [34]. Figure 31 shows the water-in-canola oil

emulsion after ten minutes and 4 hours, respectively. Note that the water has separated out

and deposited at the bottom due to high density difference between the two fluids.
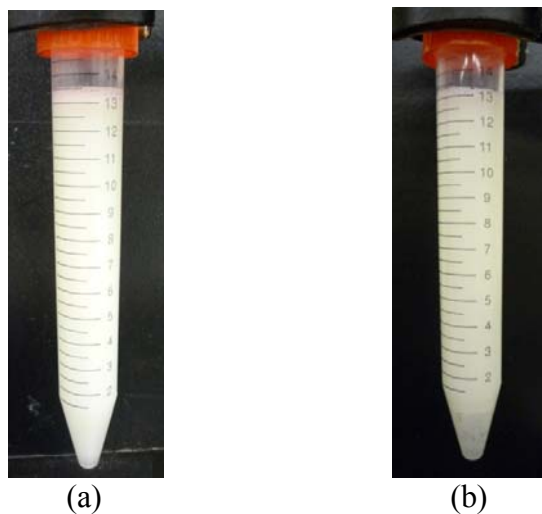
Figure 31. (a) Water-in-canola oil emulsion after ten minutes (b) after 4 hours.

45 ml (43.30 g) canola oil and 5 ml (3.95 g) methanol were blended with 2 % surfactants (0.945 g) and stirred for 25 minutes. Figure 32 shows the methanol-in-canola oil emulsion after ten minutes and 4 hours, respectively. The emulsion was stable for more than 4 hours.
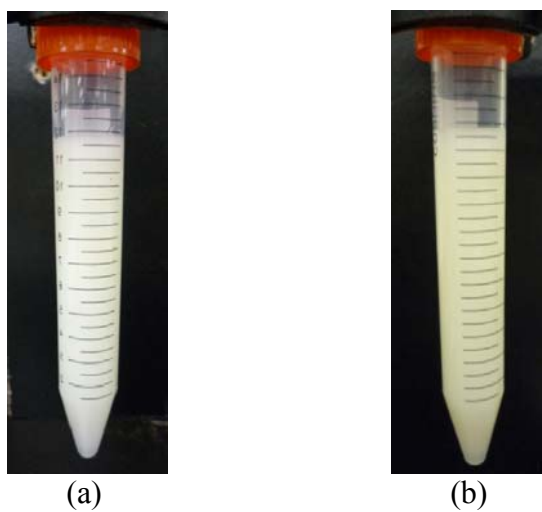
Figure 32. (a) Methanol-in-canola oil emulsion after ten minutes (b) after 4 hours.

4.8 Droplet Measurement Standard in the Optical Point of View

Droplets were measured using a reference thin wire and a 1.5X magnification on the high speed camera. First, a thin platinum wire of 0.0254 mm in thickness (0.001 inch) purchased from A-M System was used to for optical calibration. The high speed camera was used to measure the number of pixels corresponding to the thickness of the wire (6 pixels for 25.4 µm) yielding a linear resolution of 4.2 µm/pixel. The wire thickness was used as reference when measuring droplet size before and after microexplosion.

4.8.1 Camera Focus Range

Adequate range of focus was needed to measure the distributed droplets after microexplosion. A second platinum wire with a thickness of 0.0508 mm (0.002 inch) was used to focus high speed camera as well as to validate the standard measuring scale of 4.2 µm/pixel determined using a thinner Pt wire. Three 50 µm Pt wire were aligned horizontally at 1.5 mm intervals along the z-axis as shown in Figure 33. Each wire was staggered along the x-axis to be able to view all of them simultaneously.
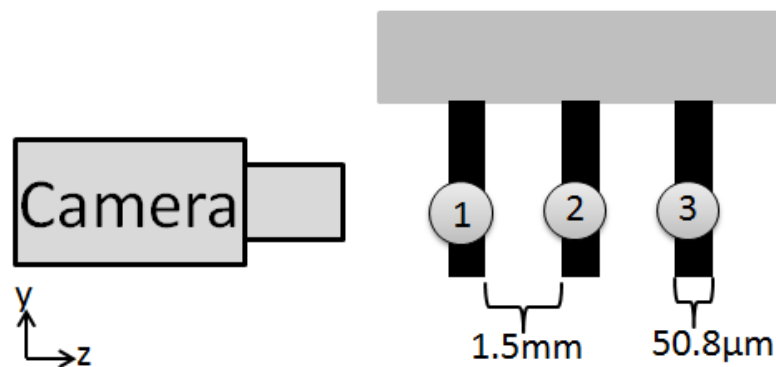
Figure 33. Schematic of micro platinum wire setup.

By controlling the camera distance from the object, three different focal positions were found for each wire. Figure 34 shows the wires in x-y plane at different focal distances. From Figure 34 (a-c), it can be seen that the working distance is no greater than 3 mm. However, the level of blurriness of the wires out of focus can be used to determine the actual size of droplets and the level of uncertainty when measuring droplet size.
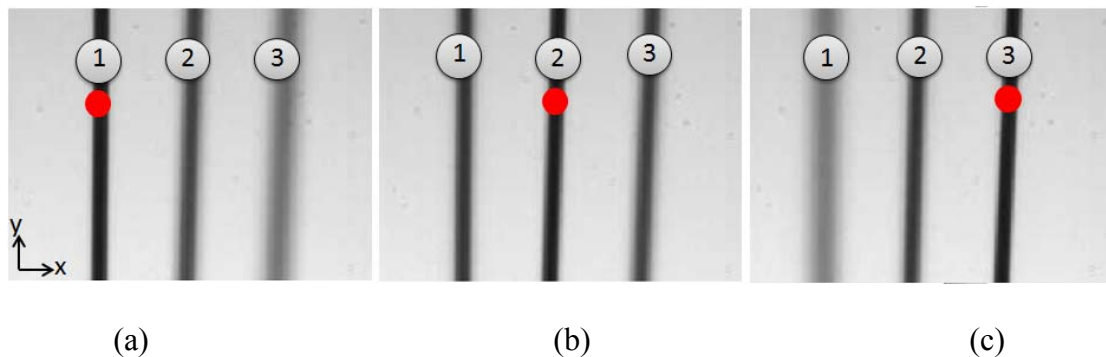
Figure 34. Three different focus ranges on the Pt wires (a) number 1 lane focused (b) number 2 lane focused (c) number 3 lane focused.

Given the wire thickness used for working distance calibration, it is estimated that a droplet located and viewed within 1.5 mm from the middle wire has an uncertainty of ±8.4 µm. Figure 35 shows the thickness of the out of focus wires varied with working distance.

Figure 35. Magnified picture of Figure 34 (b).

4.9 Droplet Preparation

25 μm (0.001 inch) diameter Pt-wire was used to suspend the microsize droplets using a very fine syringe (gage 30) to dispense a very small amount of liquid onto the Pt-wire holding station as seen in Figure 36. The droplet size was measured using a high speed imaging system with a magnification of 1.5X following the calibration procedure described below. A resolution of 4.2 μm/pixel was used during the experiment. Droplet diameter was calculated by counting the number of pixel across each droplet in the x-axis and z-axis. Since the droplet shaped was elliptical, the length along the y-axis was assumed to be the same as the one along the z-axis based on the principle of continuity. Droplet volume size adjustment was obtained using Equation (23) which corresponds to the volume of an ellipsoid. For simplicity purposes, all droplets were considered for be spherical when calculating droplet distribution statistics. With Equation (24), the radius of

an equivalent sphere can be determined by knowing the volume of the ellipsoid. Table 10

shows the characteristic droplet size for the emulsions used for this research project.

Figure 36. Droplet size adjustment.

$$V_{ellipse} = \frac{4}{3}\pi \times r_x \times r_y \times r_z \qquad (23)$$

where, $r_y = r_z$

$$r_{sphere} = \sqrt[3]{\frac{3}{4\pi} \times V_{ellipse}} \qquad (24)$$

Table 10. Initial droplet sizes for all of microexplosion or puffing cases (a) with droplet holder 1 with $r_x = 220$ µm (b) with droplet holder 2 with $r_x = 300$ µm.

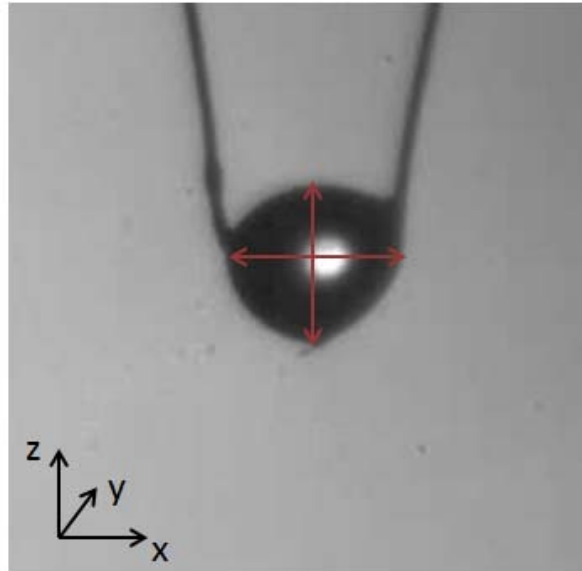|	Emulsion Type	Tem (°C)	Initial Droplet Sizes[1] (µm)								Aver. Droplet Size (µm)	STDEV
(a)	CM 85/15	980	224	215	228	232	236				227	8
	CM 90/10	980	232	239	211						227	15
	CM 85/15	900	198	206	207	211	224	236			214	14
	CM 90/10	900	164	228	233	232					214	34
	CW 90/10	980	219	237	236	232	238				232	8
	CW 90/10	900	233	244	231						236	7
	HW 20/80	730	215	210	232						219	12
	Total Average										**224**	
	Total STDEV										**9**	
(b)	CM 85/15	980	279	279	305	309	310	313			299	16
	CM 90/10	980	275	283	287	279	288	304	317	334	296	21
	CM 85/15	900	281	280	283	283	300	301	317		292	14
	CM 90/10	900	279	296	296	300	304	313	313	296	300	11
	CW 90/10	980	312	320	312	334					320	10
	CW 90/10	900	287	291	300	304	304	313	321		303	12
	HW 20/80	730	313	309	325						316	8
	Total Average										**304**	
	Total STDEV										**10**	

1: the initial droplet size corresponds to the r_{sphere}

4.10 Droplet Size Measurement

With the standard resolution scale of 4.2 µm/pixel, initial droplet size and distributed droplets size after microexplosion were determined optically. For instance, Figure 37 shows five different droplets which could be identified and selected for measurement by counting the number of pixels given the known pixel resolution. Figure 38 shows the five magnified droplets and how the measuring lines were set. As the

droplets got smaller, the level of clearness of the droplet boundary became weak which could lead to measurement errors. Droplets less than 10 μm in diameter were ignored since they could not be measured accurately. The total volume of droplets less than 10 μm can be estimated as explained in the next section.
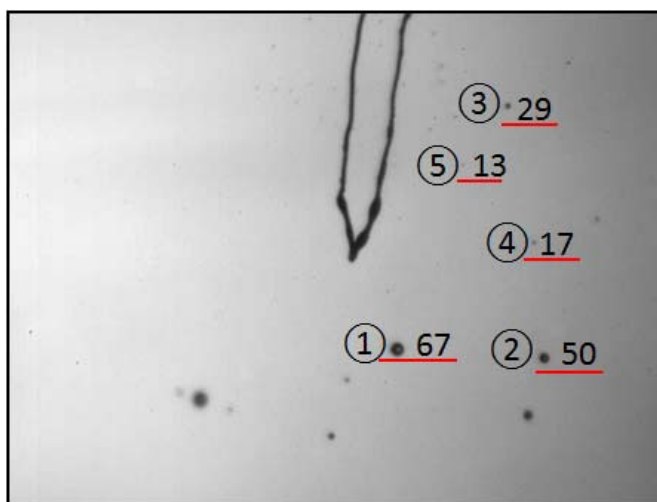
Figure 37. CM 85/15 distributed droplets after microexplosion.
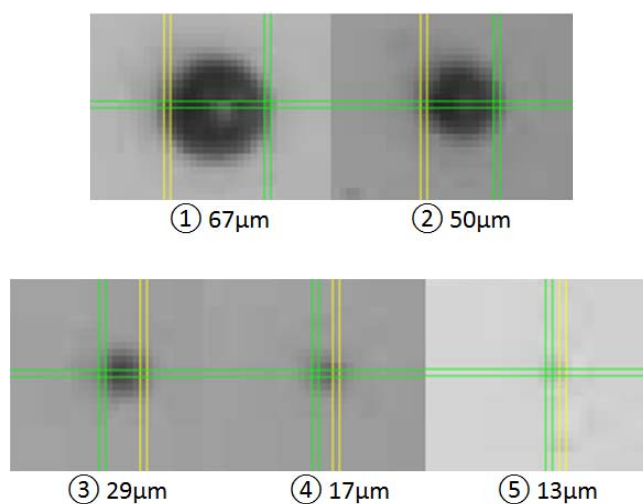
Figure 38. Distributed droplet sizes of CM 85/15.

4.11 Fine Droplet Study

Due to the limitation of the high speed camera, distributed droplets below 10 μm were ignored as explained in the previous section. Since the size of a droplet right before microexplosion and the distributed droplets right after microexplosion could be measured and counted, the estimated volume of finer droplets with diameter values less than 10 μm was calculated. Equation (25) and (26) was used to calculate the ratio of the fine droplet volume.

$$V_{Total} = \sum_i V_i + \sum_{ii} V_{ii} + V_r \qquad (25)$$

where, V_{Total} : Volume of the droplets right before microexplosion

Vi : Volume of the distributed (countable) droplets after microexplosion

Vii: Volume of fine droplets (below 10 μm)

Vr : Volume of remaining droplets on the wire

$$y = \frac{\sum_{ii} V_{ii}}{V_{Total}} \qquad (26)$$

where, y : percentage of fine droplets

Equation (26) makes the implicit assumption that the amount of fuel lost through evaporation was insignificant before microexplosion occurs. However, since droplet size decreased considerably before microexplosion, the final droplet volume before microexplosion was used to determine the percentage of fine droplets in each case. The exact concentration of secondary fuel in each case right before microexplosion was not

known since evaporation could not be stopped or avoided. Therefore, the results are reported based on the initial concentration of secondary fluid in each sample droplet.

4.12 Mathematical Description of Wave Propagation due to Microexplosion Using Long Elastic Bar Model

To relate the strength of a microexplosion event and its corresponding frequency, a partial differential equation of wave motion was derived as governing equation [38]. The partial differential equation (PDE) was based on the long elastic bar model. The PDE was solved after applying all the boundary conditions. The first boundary condition is based upon the impulse-momentum theorem [39]. The governing equation used to describe the motion of an elastic bar due to an initial displacement or velocity generated by a microexplosion force was derived as shown below. Assumptions were made as indicated below and based on shown in Figure 39.

1. The bar has a constant cross-section area in the unstrained state.

2. All cross-sectional planes remain flat surface and every element of membrane moves normal to the y-z plane.

3. Hooke's law can be applied to relate stress and strain.

4. The mass of membrane per unit area is constant.

5. Elastic modulus of object is constant.
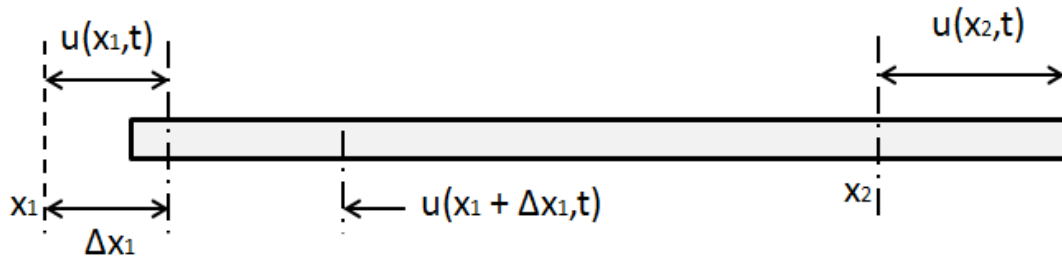
Figure 39. Medium of an elastic bar.

u (x ,t) is the displacement of the plane of particles as a function of time. From Hooke's law, the force acting upon the medium at x_1 can be estimated using Equation (27) and the Newton's second law as stated in Equation (28).

$$F_x = area \times E \times strain = AE\left[\frac{\partial u}{\partial x}(x_2,t) - \frac{\partial u}{\partial x}(x_1,t)\right] \tag{27}$$

where, E is elastic modulus

$$F_x = ma = \rho A(x_2 - x_1)\frac{\partial^2 u}{\partial t^2} \tag{28}$$

Equations (27) and (28) are coupled and divided by $(x_2 - x_1)$ resulting in the final governing equation as shown in Equation (29).

$$\frac{\partial^2 u}{\partial t^2} = a^2 \frac{\partial^2 u}{\partial x^2} \tag{29}$$

where, $a = \sqrt{\dfrac{E}{\rho}}$ is the longitudinal wave speed (m/s)

Next, a longitudinal elastic bar was used to represent the Pt stick which is shown schematically in Figure 40. An explosive force acting on the end of the bar was used to represent the microexplosion effect as shown in Figure 40. The explosive wave generated from a single droplet microexplosion event can be categorized as an impulse force, which can be taken into account using the impulse–momentum equation and Newton's second law. Equation (29) is used to relate momentum P with wave velocity [39].
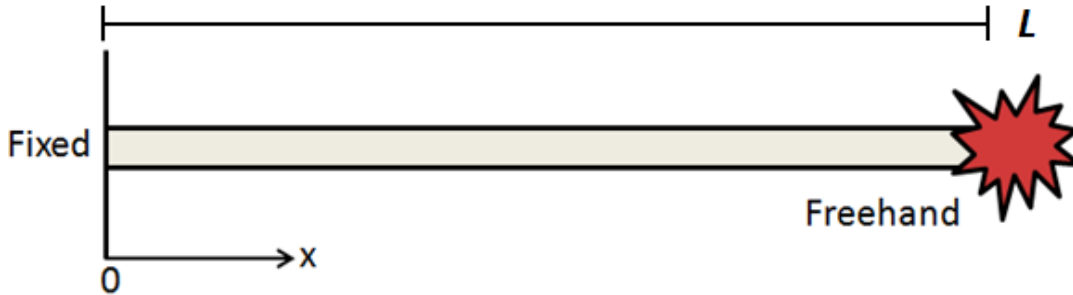
Figure 40. Elastic bar with fixed and free hand condition.

$$I = \Delta P \tag{30}$$

$$I = F\Delta t \tag{31}$$

$$F\Delta t' = m\Delta v \tag{32}$$

where, ΔP is the change in linear momentum

F is the constant total net force (N)

$\Delta t'$ is the time interval over the impulse force (s)

m is the constant mass of the object (kg)

Δv is the change in wave velocity produced by the force (m/s)

With the given governing equation, four boundary conditions for the experimental system are as follows.

① $u(0,t)=0$ for no displacement $x=0$

② $\dfrac{\partial u}{\partial x}(L,t)=0$ for no displacement gradient at free end $x=L$

③ $u(x,0)=0$ for no initial displacement $t=0$

④ $\dfrac{\partial u}{\partial t}(x,0)=\dfrac{Ft'}{m}$ for the impulse at $t=0$

The solution of Equation (33) after applying the four boundary conditions is as follows (see Appendix A).

$$\therefore u(x,t)=\sum_{n=0}^{\infty}C'_n \sin\!\left(\sqrt{\lambda}x\right)\sin\!\left(a\sqrt{\lambda}t\right) \tag{33}$$

where, $C'_n = \dfrac{2}{L}\cdot\dfrac{Ft'}{m}\displaystyle\int_0^L \sin\!\left(\sqrt{\lambda}x\right)dx$

$$\lambda=\left(\dfrac{(2n+1)\pi}{2L}\right)^2 \qquad n=1,\,2,\,3\ldots$$

Equation (33) shows that an increase in force coming from an increase in the strength of microexplosion which should result in larger displacements. Since the total period of the particle displacement can be obtained by measuring the time of the impulse wave using an acoustic sensor, the sound wave velocity can be calculated using Equations

(34) and (35). The relation between frequency and sound save velocity is expressed in Equation (36).

$$\frac{u(x,t)}{T} = \frac{1}{T}\sum_{n=0}^{\infty} C_n' \cos\left(\sqrt{\lambda}x\right)\sin\left(a\sqrt{\lambda}t\right)$$ (34)

where, T is the total period of impulse wave (s)

$$\frac{u(x,t)}{T} = v$$ (35)

$$f = \frac{v}{u(x,t)}$$ (36)

where, v is the particle wave velocity produced by the impulse force (m/s)

f is frequency (Hz)

Thus, the stronger microexplosion force is, the larger the displacement of particles becomes which results in lower frequency.

5. RESULTS AND DISCUSSION

This section presents the results of microexplosion experiments conducted using emulsions of hexadecane-water and canola oil-methanol under various conditions. The section also presents the analysis of distributed droplets generated after each microexplosion event. The analysis of acoustic waves and frequencies due microexplosion under various conditions is presented and discussed. The results of the microexplosion experiments show the effects of initial droplet size, chamber temperature and emulsion on microexplosion phenomena.

All the experiments were conducted under constant chamber temperatures 900 ˚C and 980 ˚C when canola oil emulsions were tested. Emulsions of hexadecane were tested at lower temperatures. All the emulsion droplets ranged from 150 μm to 350 μm. Among the samples, droplets of around 230 μm and 300 μm in diameter were optically and acoustically analyzed.

5.1 Optical Analysis of Microexploded Droplets

The first objective of the project was to determine the effects of chamber temperature, initial droplet size and fuel composition on microexplosion phenomena. In this section, microexplosion events were studied from the optical point of view.

Microexplosion phenomena happen when a liquid fuel droplet breaks up into finer droplets violently under a sudden exposure to high temperatures. The droplet growth is

driven by the difference in vapor pressures between its interior and exterior. Figure 41 shows an example of microexplosion event.

| (a) 0.914 seconds | (b) 0.915 seconds |
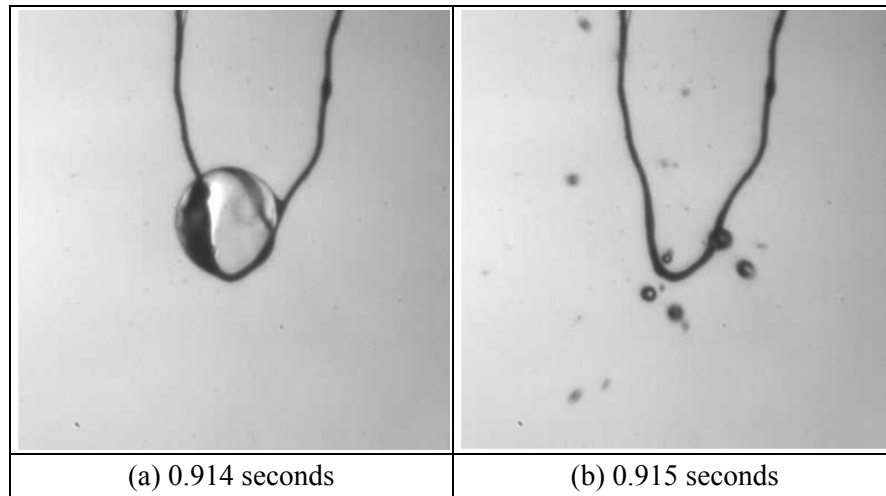
Figure 41. Microexplosion event of CW emulsion at 980 ˚C.

5.1.1 Probability of Microexplosion and Puffing

The probability of microexplosion in droplets was statistically studied in order to understand the conditions that lead to microexplosion phenomena. The overall probability of microexplosion events regardless of initial droplet condition ranging from 157 μm to 351 μm with a standard deviation of 43.3 μm was first studied to understand the direct relationship of microexplosion events with temperatures, and the different concentrations and compositions. Table 11 shows the probability of microexplosion phenomena at two temperature conditions and different emulsions.

Table 11. Overall probability of microexplosion (ME) events for all droplet sizes.

980 °C	CM 85/15[*]	Probability of ME	17/27[**]	63 %
	CM 90/10[*]	Probability of ME	14/27[**]	52 %
	CW 90/10[*]	Probability of ME	12/18[**]	67 %
900 °C	CM 85/15[*]	Probability of ME	15/27[**]	56 %
	CM 90/10[*]	Probability of ME	14/39[**]	36 %
	CW 90/10[*]	Probability of ME	12/25[**]	48 %

[*] Initial composition of each emulsion type
[**] Denominator includes all phenomena such as ME, puffing and combusting

In Table 11 it can be seen that higher temperatures and higher concentration of methanol in the emulsions leads to the higher probability of microexplosion. The increase in the probability of microexplosion at higher temperatures is the direct result of the sudden expansion of the emulsified secondary fluids (water or methanol) when they reach the superheat limit. Moreover, at higher temperature, Equation (20) predicts higher occurrence of nucleation and microexplosion. Also, greater quantities of methanol or water inside of an emulsified droplets lead to an increase in the number of nucleation sites which provides the necessary conditions for microexplosion. In a previous study, Tsue et al. [14] found out that an increase in water content in fuels leads to an increased rate of microexplosion. On the other hand, a lesser amount of high vapor pressure fluids (methanol and water) often leads to a lesser probability of microexplosion of emulsion. When the rate of vaporization of the high vapor pressure fluid within a droplet is faster than the rate of nucleation at high temperatures, the emulsion droplets usually vaporized or combusted before they microexplosion occurred. When bubble nucleation rate is

slower than the rate of vaporization at lower temperatures, droplets experience a sudden decrease in size due to evaporation.

The probability of microexplosion of water-in-canola emulsion is greater than for methanol-in-canola emulsion at 900 °C. This is related to the surface tension and vapor pressure of the emulsified water and methanol in the droplets. Since the surface tension of water and methanol are 72 dyn/cm and 23 dyn/cm, respectively, it can be inferred that water requires greater internal pressures to counteract its high surface tension leading to a super critical state instead of simply evaporating from each droplet. However, under the same conditions, the dispersed methanol droplets inside an emulsified droplet of canola oil can easily vaporize or lead to puffing at relative low temperatures.

Puffing is characterized the ejection of the inner content of the emulsified droplet but without the complete breakage of the droplet. In the case of hexadecane emulsions, microexplosion occurred almost a 100 % of the time when initial droplets size was from 200 μm to 350 μm at 730 ˚C. Hexadecane emulsion droplets larger than 400 μm showed puffing before microexplosion took place. This confirms the fact [16] that the occurrence of puffing increases with droplet size. In the case of the CM 85/15 emulsion, CM 90/10 emulsion and CW 90/10 emulsion with the given conditions, puffing occurrence were detected. Figure 42 shows a puffing occurrence of CM 90/10 droplet at 900 ˚C.
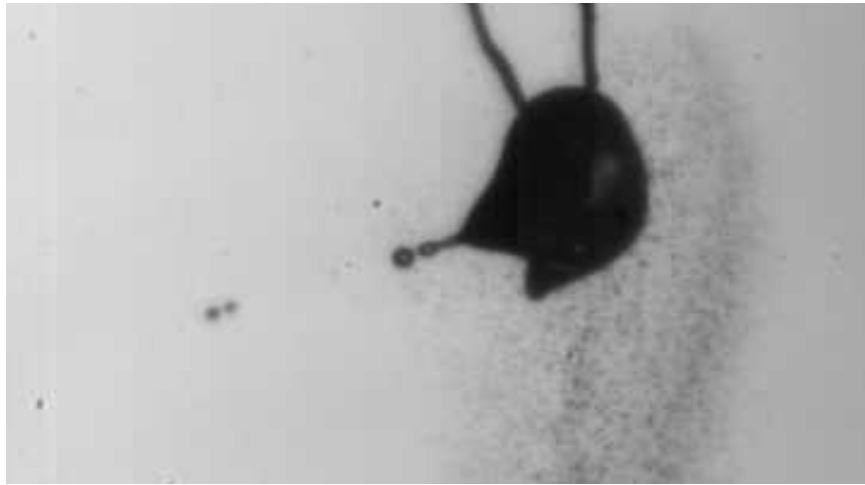
Figure 42: Puffing event of CM 90/10 at 900 ˚C.

Puffing events usually occurred prior to microexplosion. Reasons for this behavior include weak surface tension, large volume of emulsified droplets, and low temperatures. Table 12 depicts the probability of puffing events of each emulsion with droplet size ranging from 200 μm to 350 μm. The puffing probability of all of the emulsions at 980 ˚C was less than those at 900 ˚C. This was because under higher temperature condition, the high vapor pressure fluid within the emulsified droplets underwent complete evaporation or resulted in microexplosion without puffing. At lower temperatures, there is a correlation between the amount of methanol and puffing occurrence. More concentration of the low vapor pressure fluid increases the occurrence of puffing phenomena at lower temperatures. This can be explained by the lower surface tension and the associated lower Laplace pressure of the volatile droplets which leads to partial breakage of the droplet before it can completely microexploded. However, the effect of surface tension in CM

90/10 and CW 90/10 was not significant on the occurrence of puffing at 900 ˚C. Thus, it can be concluded that temperature is the most dominant factor that affects puffing.

Table 12. Probability of puffing event.

980 ˚C	CM 85/15[*]	Puffing	4/27[**]	15 %
	CM 90/10[*]	Puffing	3/27[**]	11 %
	CW 90/10[*]	Puffing	0/18[**]	0 %
900 ˚C	CM 85/15[*]	Puffing	10/27[**]	37 %
	CM 90/10[*]	Puffing	6/39[**]	15 %
	CW 90/10[*]	Puffing	4/25[**]	16 %

[*] Initial composition of each emulsion type
[**]Denominator includes all phenomena such as ME, puffing and combusting

The droplet size effect on microexplosion was also observed during the experiments. Table 13 shows that probability of microexplosion for two initial droplets sizes. For all the blend compositions, smaller droplets (224 µm ±8.4 µm) experienced a greater probability of microexplosion than larger droplets (304 µm ±8.4 µm). One reason for the reduced occurrence of microexplosion of larger droplets can be attributed to the occurrence of puffing. Droplets that experience puffing first lose a considerable amount of high vapor pressure fluid which is necessary for the formation of nucleation sites before microexplosion occurs. Table 13 shows that at smaller initial droplet size, higher temperatures and greater methanol content results in greater probability of microexplosion. The overall probability of microexplosion for 224 µm and 304 µm droplets is very similar to the probability microexplosion for all droplet sizes as shown in Table 13.

Table 13. Probability of microexplosion events at all the parameters.

Tem (°C)	Emulsion Type	Explosion Type	224 µm (±9 µm)		304 µm (±9 µm)		Overall Probability of 224 µm and 304 µm droplet size
980	CM 85/15[*]	Probability of ME	4/5[**]	80 %	6/8[**]	75 %	77 %
	CM 90/10[*]	Probability of ME	3/4[**]	75 %	7/14[**]	50 %	61 %
	CW 90/10[*]	Probability of ME	5/7[**]	71 %	4/6[**]	67 %	70 %
900	CM 85/15[*]	Probability of ME	6/9[**]	67 %	6/10[**]	60 %	70 %
	CM 90/10[*]	Probability of ME	4/7[**]	57 %	6/17[**]	35 %	41 %
	CW 90/10[*]	Probability of ME	3/4[**]	75 %	5/10[**]	50 %	57 %

[*] Initial composition of each emulsion type
[**] Denominator includes all phenomena such as ME, puffing and combusting

5.2 Study of Distributed Secondary Droplets

The distribution of secondary droplet sizes after microexplosion was studied to find correlations among initial droplet size, chamber temperature and emulsion. Since the high speed camera was able to capture images at a speed of 1000 Hz which is faster than the speed of exploding secondary droplets, the camera was also able to capture images of secondary droplets undergoing microexplosion at a resolution of 1024 x 1024.

5.2.1 Methanol-in-Canola Emulsion

Two Types Droplet Expansion in Methanol-in-Canola Oil Emulsions

Two swelling or droplet expansion types were visibly identified before microexplosion could take place in certain methanol-in-canola oil emulsion droplets as depicted in Figure 43. Depending on the types of droplet expansion, microexplosion

events could occur in different ways. The first case involved the swelling or expansion from a single bubble. When the emulsions are exposed to high temperatures, the dispersed water droplets inside the emulsified droplet easily coalesce into a single water core surrounded by a layer of canola oil due to its high surface tension. Under those conditions, the droplet can be described by the Birchley-Riley emulsion model [33]. In the case of multi-bubble swelling phenomena, multiple bubbles inside the emulsified droplet could be observed when the chamber temperatures were not high enough to increase mixing and coalescence of bubbles within the droplet.
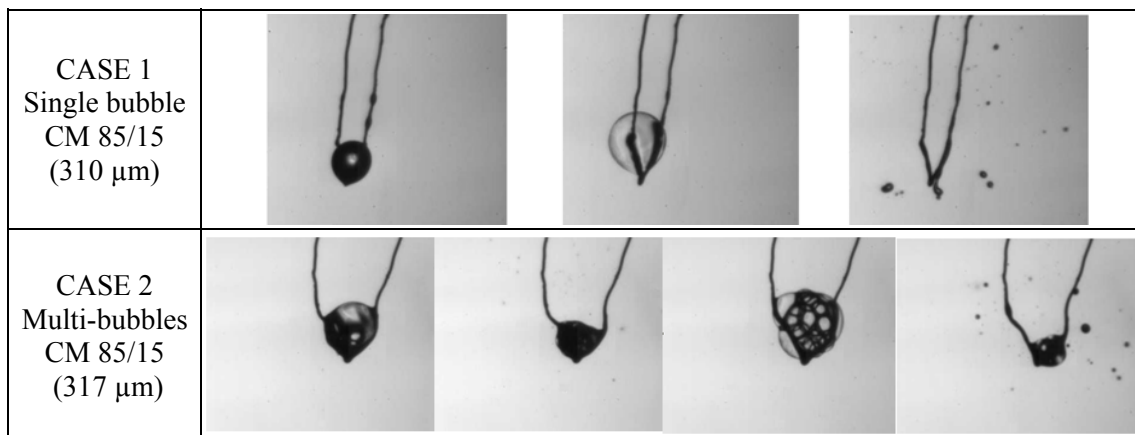

Figure 43. Two types of droplet expansion before microexplosion of CM 85/15 emulsion.

In Table 14 it can be seen that the probability of multi-bubble swelling depends on methanol concentration and temperature as shown. The definition of multi-bubble expansion is when multiple bubble nucleation of the dispersed secondary fluids in emulsion droplet take place and the bubbles do not coalesce into one single core bubble before microexplosion. That is due to the fact that the amount of well-dispersed methanol

droplets in CM 85/15 emulsion is more than that in CM 90/10 emulsion. Furthermore, at lower temperatures, higher probability of the multi-bubble swelling was found because the dispersed methanol in the droplet emulsion could not coalesce easily into a single bubble because of insufficient mixing of methanol within the droplet as shown in Figure 44. Also, it can be observed that as temperature increases, the probability multi-bubble expansion decreases. Such phenomena could be considered as Thermophoresis or the Soret effect since it involves the mixing two different liquids in the presence of a temperature gradient. Similar results were reported from Suzuki et al. [40] where the aggregation rate of water was shown to increase with higher temperatures of the emulsified droplets. Figure 45 shows a coalesced single bubble formation.

Table 14. Probability of multi-bubble swelling.

980 ˚C	CM 85/15[*]	Probability of Multi	6/28[**]	21 %
	CM 90/10[*]	Probability of Multi	1/28[**]	4 %
900 ˚C	CM 85/15[*]	Probability of Multi	9/29[**]	31 %
	CM 90/10[*]	Probability of Multi	2/40[**]	5 %

[*] Initial composition of each emulsion type
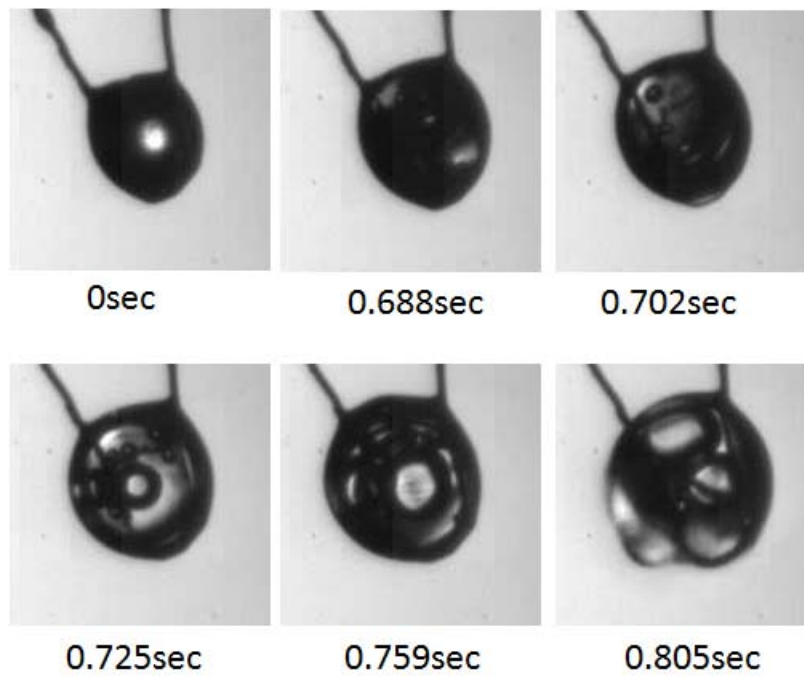[**] Denominator includes all phenomena such as ME, puffing, and combusting

Figure 44. Multi-bubble nucleation type before microexplosion of CM 85/15 at 900 ˚C.
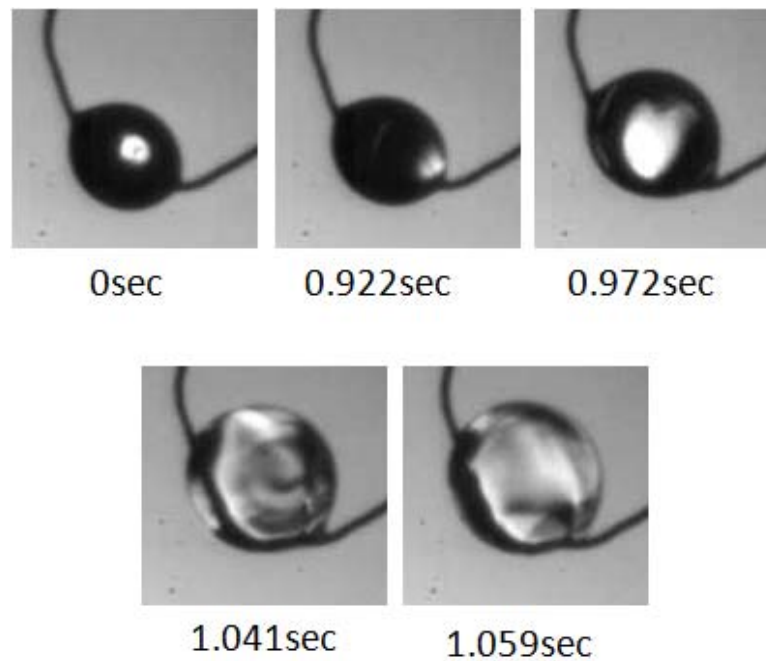

Figure 45. Single-bubble formation before microexplosion of CM 85/15 at 980 ˚C.

Multi-bubble swellings were not detected in water-in-canola oil and hexadecane-in-water emulsions. This can be attributed to the high surface tension of water causing small vapor bubbles to coalesce as temperature increases.

Statistics of Distributed Methanol-in-Canola Oil Droplets after Microexplosion

Microexplosion experiments for several droplets were conducted at the same chamber temperature to understand the correlation between the distribution of secondary droplet sizes after microexplosion and input parameters such as initial droplet size and emulsion type. Only droplet sizes larger than 10 μm diameter were considered due to the limited resolution of the high speed camera below 10 μm. Nevertheless, the overall volume ratio of finely distributed droplets (less than 10 μm) was statistically determined as discussed in the next section.

Figure 46 depicts the statistics of the distributed CM emulsion droplet sizes after microexplosion at 900 ˚C. It can be seen that larger initial droplet size leads to the larger distributed droplets after microexplosion. One reason for the large average distributed droplet size can be attributed to the large surface area of the initial droplet. With greater initial droplet surface area, the droplet partially microexplodes and it quickly contracts until higher inner pressures are reached. Once the critical inner pressure is reached again at high surface tension due to its intermediate and smaller droplet size, it completely microexplodes as depicted in Figure 47. In other words, larger droplets undergo multiple microexplosion events until they finally microexplode entirely. Furthermore, with CM 85/15 emulsion, smaller distributed droplets after microexplosion were found due to the

greater amount of dispersed methanol. Also, the distributed droplets of CM emulsions at 980 ˚C showed similar pattern with that at 900 ˚C as depicted in Figure 47. The percentage of the distributed droplets was calculated based on the volume of all droplets. Figure 48 shows statistics of distributed droplet size of CM emulsion at 980 ˚C.
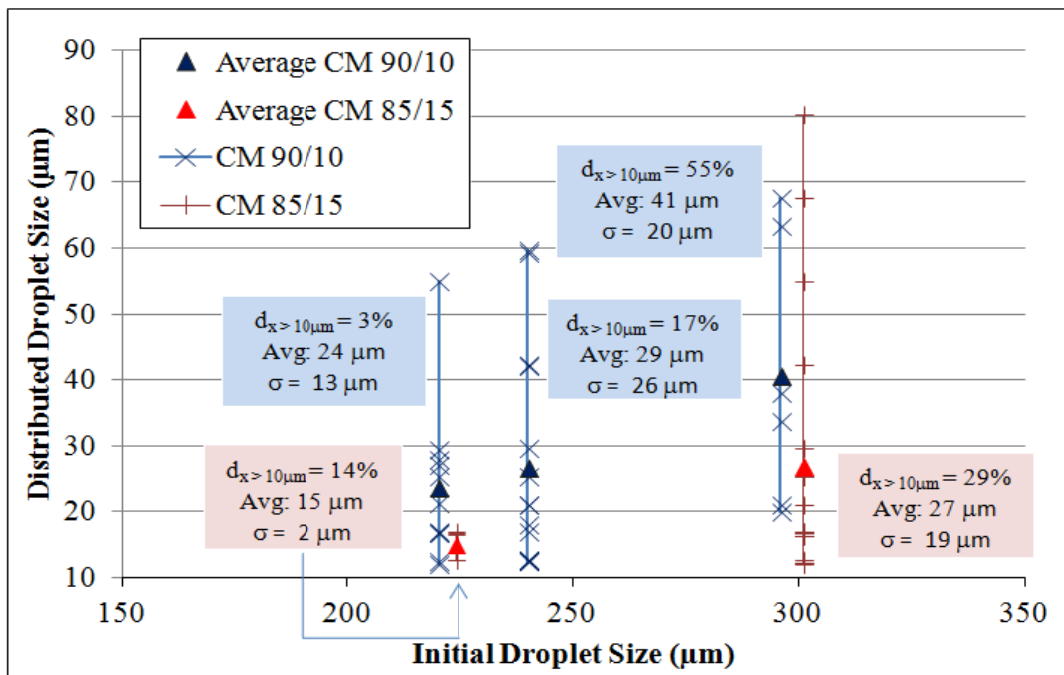

Figure 46. Statistics of distributed droplet size of CM emulsion at 900 ˚C.

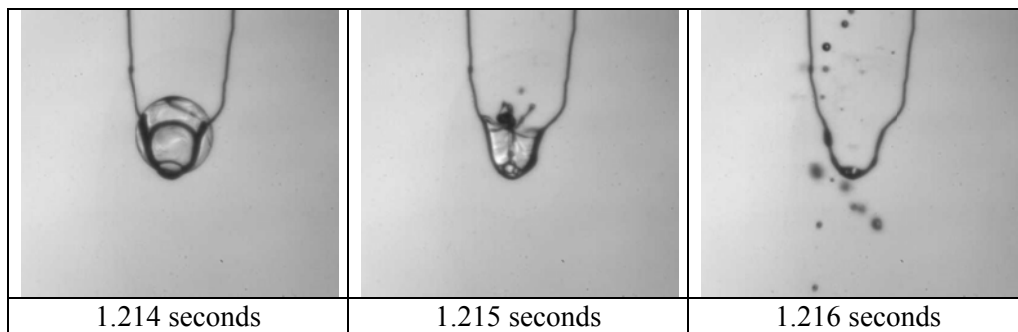| 1.214 seconds | 1.215 seconds | 1.216 seconds |

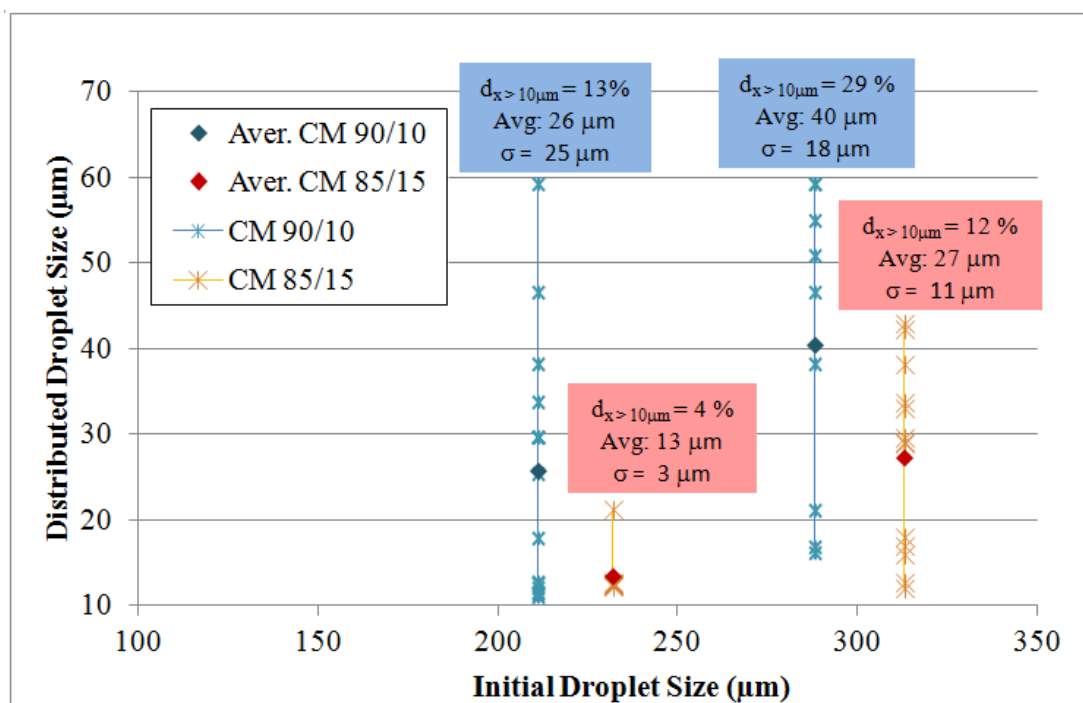Figure 47. Partial microexplosion of distributed droplets.

Figure 48. Statistics of distributed droplet size of CM emulsion at 980 ˚C.

In Figure 49, it is straightforward to understand that smaller initial droplet size leads to a finer droplet size distribution after microexplosion. Also, more methanol content in the dispersed droplets also results in finer droplets after microexplosion. The effect of temperature on average droplet size after microexplosion with the same emulsion was not as significant as composition or droplet size. However, from Figures 46 and 48, it can be seen that higher temperatures lead to finer droplets with average size less than 10 μm. This is explained in greater detail below.
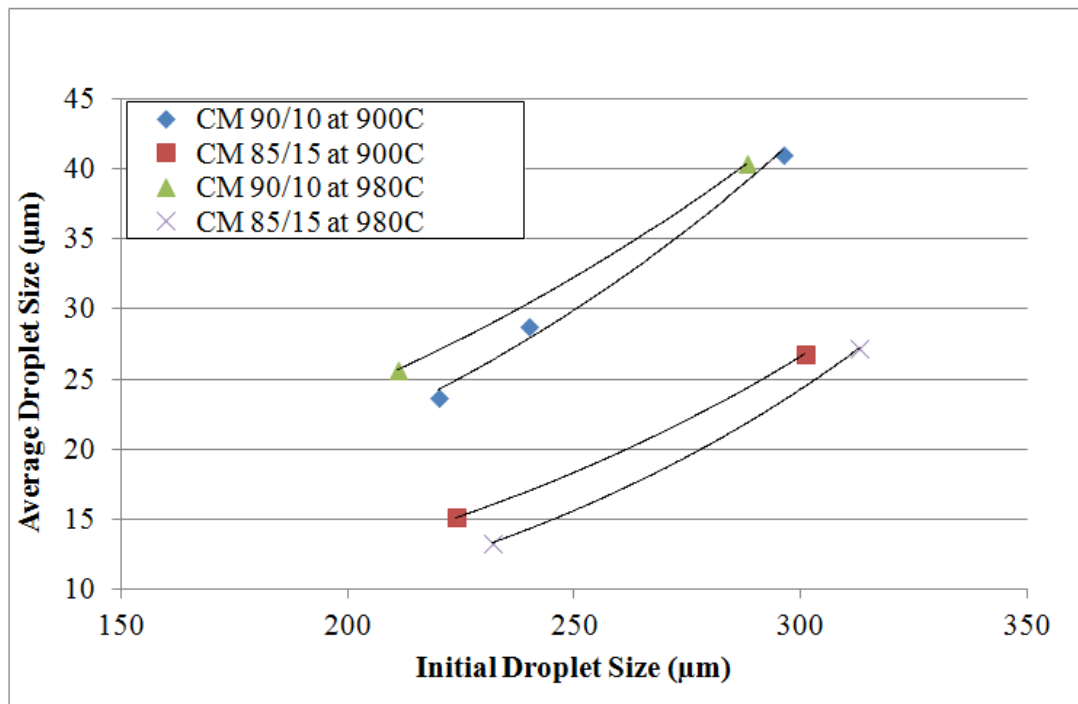
Figure 49. Comparison of average distributed size of CM emulsion at each temperature.

Methanol-in-Canola Oil Fine Droplets

From Table 15, smaller initial droplet size and greater methanol concentration leads to higher percentage of finer droplets. This is due to the combination of higher vapor pressure under higher surface tension when microexplosion occurs. Furthermore, at higher temperatures, finer droplets are formed through primary and secondary microexplosion events. The volumetric percentage was obtained using Equation (25) and (26).

Table 15: Statistical study of distributed methanol-in-canola fine droplets after ME.

Temp (°C)	Emulsion Type	Droplet size before ME (μm)	Microexploded Average Droplet (μm) (> 10 μm)	Microexploded Fine Droplets (%) (< 10 μm)	Size of Droplet on Stick after ME (μm)
900	CM 90/10*	220	24	97 %	0
		240	29	83 %	60
		296	41	45 %	125
	CM 85/15*	224	15	86 %	57
		301	27	71 %	138
980	CM 90/10*	211	26	87 %	88
		288	40	71 %	182
	CM 85/15*	232	13	96 %	40
		313	27	88 %	74

* Initial composition of each emulsion type

5.2.2 Water-in-Canola Emulsion and Hexadecane-in-Water Emulsion

The distributed droplet size of CW emulsion and hexadecane emulsion after microexplosion showed the same results as of CM emulsion droplets. As the initial droplet size decreased, the average distributed droplet sizes were smaller in both emulsions, as shown in Figures 50 and 51. Also, the effect of the temperature on the CW distributed droplet size after microexplosion was not significant, which is similar results with CM emulsion. However, in CW emulsion, a large number of droplets with size of 10 μm or less were formed as seen in Figure 50. Again, this is indicative of the effect of the surface tension between water and canola oil that led to very high internal pressures before each droplet microexploded.
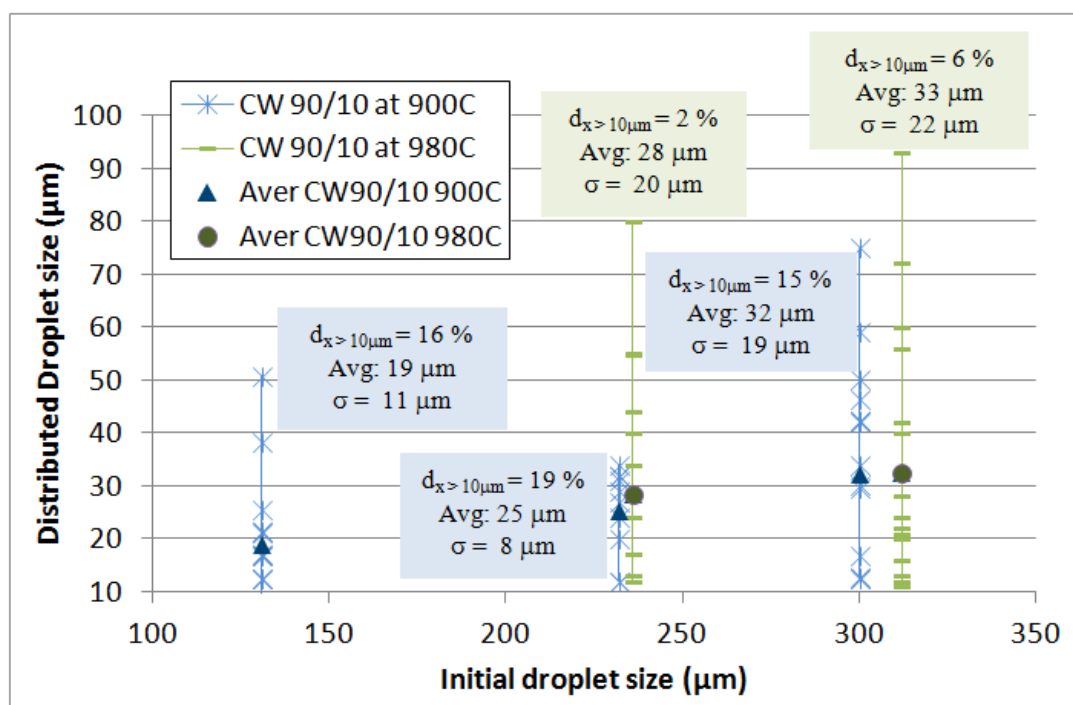
Figure 50. Statistics of distributed size of CW emulsion at 900 ˚C and 980 ˚C.
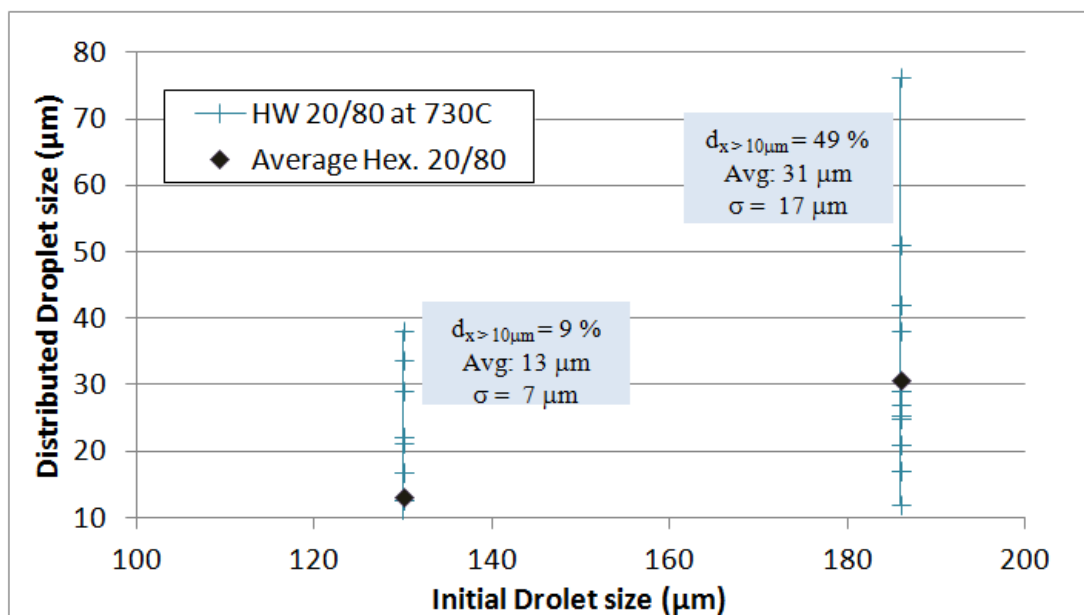

Figure 51. Statistics of distributed size of hexadecane emulsion at 730 ˚C.

Table 16 depicts the percentage of fine droplets for different conditions. The initial size of CW emulsified droplets had little effect of the percentage of fine droplets as seen in Table 15. At higher temperatures, finer droplets were formed. In the same manner, the initial size of hexadecane emulsions droplets has the same effect of the percentage of fine droplets after microexplosion as depicted in Table 17.

Table 16. Statistical study of distributed water-in-canola fine droplets after ME.

Temp. (°C)	Emulsion Type	Droplet size before ME (μm)	Microexploded Ave. Droplet size (μm) (> 10 μm)	Microexploded Fine Droplets (%) (< 10 μm)	Size of Droplet on Stick after ME (μm)
900	CW 90/10[*]	131	19	84 %	118
		232	25	81 %	114
		300	32	85 %	130
980	CW 90/10[*]	236	28	98 %	0
		312	32.5	94 %	0

[*] Initial composition of each emulsion type

Table 17. Statistical study of distributed hexadecane-in-water fine droplets after ME.

Temp. (°C)	Emulsion Type	Droplet size before ME (μm)	Microexploded Ave. Droplet sizes (μm) (> 10 μm)	Microexploded Fine Droplets (%) (< 10 μm)	Size of Droplet on Stick after ME (μm)
730	HW 20/80[*]	130	13	91 %	114
		186	31	51 %	118

[*] Initial composition of each emulsion type

5.2.3 Continuous Microexplosion after Initial Microexplosion

Secondary microexplosion of emulsified droplets was observed in multiple occasions. For instance, Figure 52 shows secondary microexplosion events in CM 90/10 of a 135μm droplet.
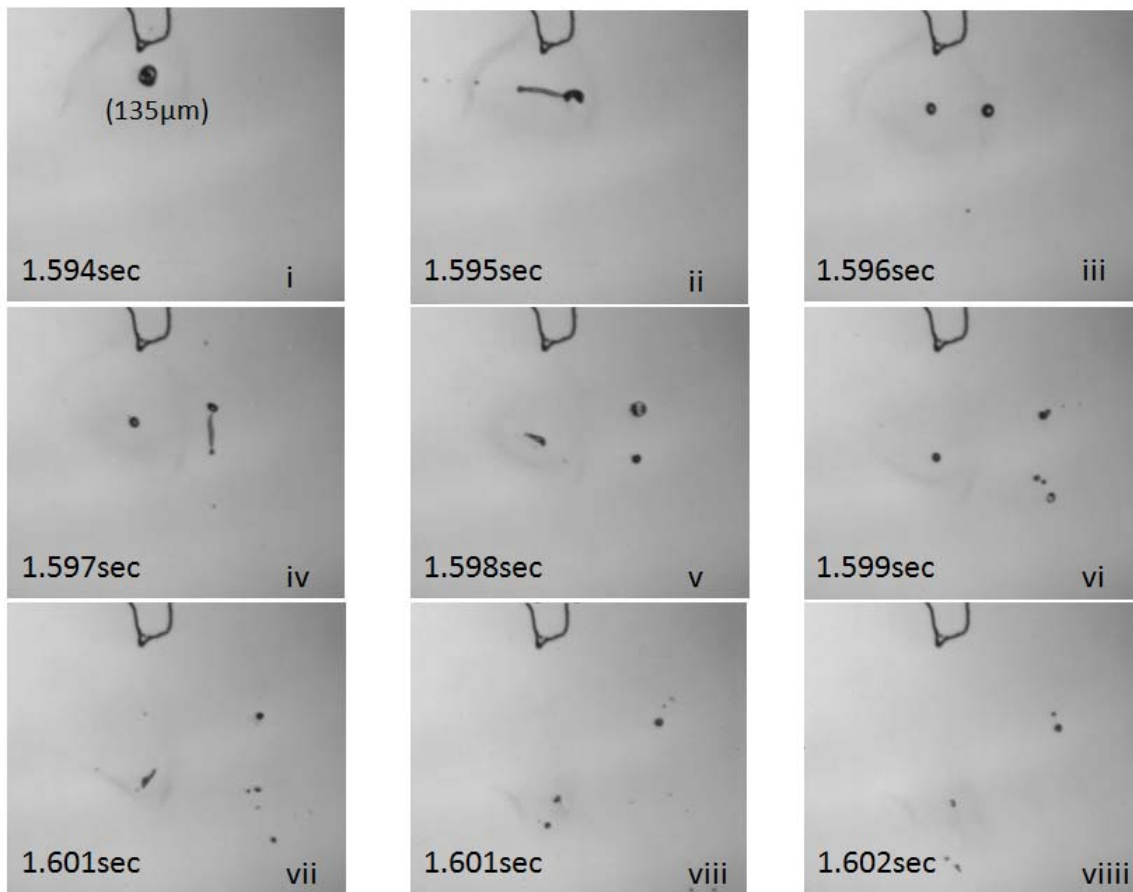

Figure 52. Continuous microexplosion after first microexplosion of CM 90/10.

5.3. Signal Analysis

The signal processing technique discussed in section 3 was used to evaluate the specific characteristics of microexplosion phenomena. Microexplosion acoustic sound

waves were collected and studied along high speed camera images. Sound wave signals were transformed to frequency using a FFT algorithm. For analysis, calibration of the acoustic and synchronization between the acoustic sensor and the high speed camera were undertaken using a pencil lead break test. Furthermore, noise frequencies generated by experimental equipment were investigated and filtered out to be able to detect the corresponding microexplosion frequencies.

5.3.1 Study of Noise Frequency

A pencil lead break test was used to understand the performance of the transducer, and to distinguish between the microexplosion and noise frequencies. Many pencil lead tests were conducted and the noise frequencies were statistically analyzed. The frequencies of the Pt stick and Pt wire used as a medium to transfer acoustic waves were studied as well. Four setups were proposed for the pencil lead break test as shown in Figure 53. A preamplifier was set at 60 dB which amplified wave signals 1000 times. Six pencil lead tests with the setup as shown in Figures 53 (a) and (b) were conducted. Ten tests with the setup shown in Figures 53 (c) and (d) were conducted as well. Then, the frequency peaks of each case were statistically studied. The frequency peaks for all cases are shown in Table 18. Table 18 includes frequencies for sensor noise, Pt stick noise, Pt wire noise, and whole set up noise. All of the frequencies shown 50% probability or higher were considered as noise frequencies.
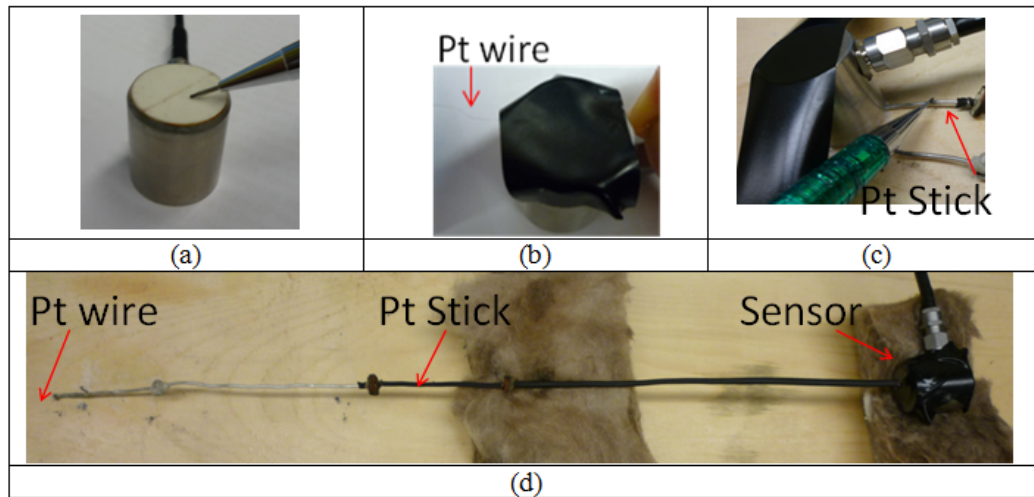
Figure 53. Setups for pencil lead break test, (a) test on the sensor (b) test on the Pt wire (c) test on the Pt stick (d) test on the Pt wire that is connected to Pt stick.

Table 18. Noise frequencies of the medium.

(a) Sensor noise		(b) Pt stick noise		(c) Pt wire noise		(d) noise of whole parts	
Avg. (kHz)	Peak Probability	Avg. (kHz)	Peak Probability	Avg. (kHz)	Peak Probability	Avg. (kHz)	Peak Probability
30.4	**100 %**	**30.1**	**100 %**	**30.1**	**100 %**	**30.1**	**100 %**
38.8	40 %	**38.7**	**100 %**	38.6	100 %	**36.1**	**81 %**
72.5	10 %	66.8	20 %	57.7	42 %	37.5	25 %
81.1	**80 %**	**80.9**	**50 %**	67.4	75 %	55.7	19 %
90.5	**90 %**	88.9	1 %	**72.5**	**75 %**	66.1	56 %
100.4	**60 %**	93.3	10 %	**80.8**	**83 %**	72.2	25 %
112.9	30 %	96.4	30 %	**88.4**	**58 %**	**81.1**	**63 %**
141	10 %	**102**	**70 %**	90	25 %	**89**	**75 %**
227.7	10 %	115.1	10 %	**96.2**	**50 %**	92.9	38 %
		157	10 %	**101.1**	**83 %**	**99.1**	**56 %**
				135.4	**58 %**	115.2	25 %
						129.4	25 %
						135.6	**83 %**

Additionally, the noise frequency of the cooling pipe was also considered. As the Pt stick was located in the center of tube, noise from the cooling pipe had to be filtered out when analyzing the frequency of microexplosion. As depicted in Figure 54, the noise frequencies of cooling pipe were below 80 kHz, 120 kHz and 180 kHz.
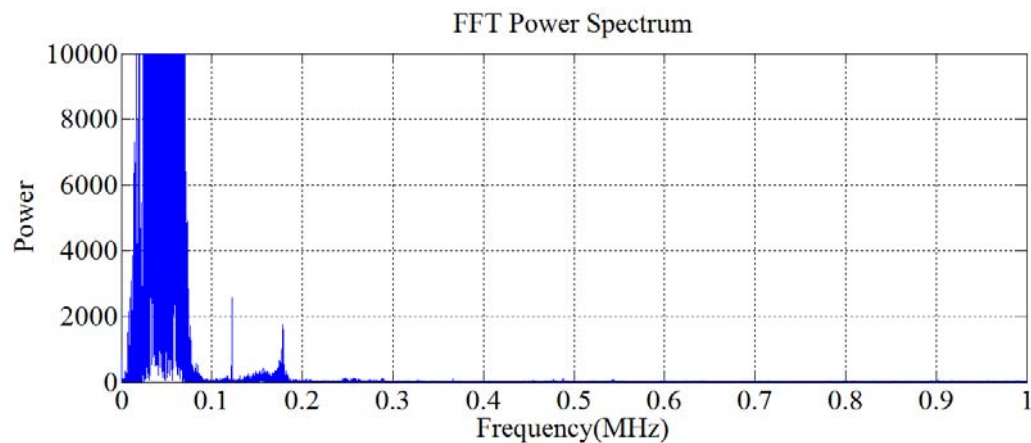

Figure 54. Noise frequency of cooling pipe.

5.3.2 Analysis of Microexplosion of Hexadecane Emulsion

Once the acoustic sensor system and high speed camera system were synchronized, sensing of microexplosion through acoustic sensing had to be undertaken. The whole system was validated using the experimental published results by Yamasaki et al. [31] under the same condition. After the acoustic sensor setup validation, two different droplet sizes of hexadecane emulsion (19 % n-hexadecane + 79 % water + 2 % (w/w) surfactant) were burned using a small flame torch as conducted by Yamasaki et al. [31]. The droplets were also tested in the heated chamber at 730 ˚C.

Yamasaki's Experiment **[31]**

Yamasaki et al. [31] used a flame lighter or small torch to combust a 1.8 mm droplet hexadecane emulsion (20 % n-hexadecane/ 80 % water) by suspending it at the tip of quartz fiber. The sampling rate was set at 0.2 MHz. Figure 55 shows the time response due to puffing and microexplosion of the droplets as reported by Yamasaki et al. [31]. Microexplosion took place at point A while puffing occurred at point B.
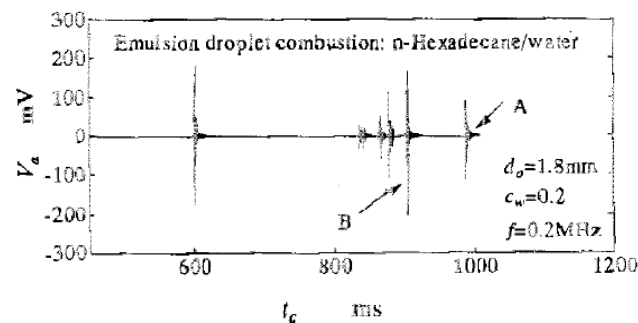

Figure 55. Time response of ME of a HW emulsion from Yamasaki's paper [31].

Using the same method as Yamasaki's [31], hexadecane emulsion droplets were burned using a small flame torch. Figure 56 shows the time response of microexplosion and puffing. Images of microexplosion are depicted in Figure 57 in the same time scale. As seen in Figures 56 and 57, the first puffing event took place at around 1.43 seconds, followed by continuous puffing and the associated decrease in droplet volume before it microexploded at 1.781 seconds as shown in Figure 57 (c). Even though a smaller droplet was used for validation purposes, it is evident that both systems have been properly

synchronized and the characteristics behavior observed by Yamasaki et al. [31] was also captured by both systems used in the current study.
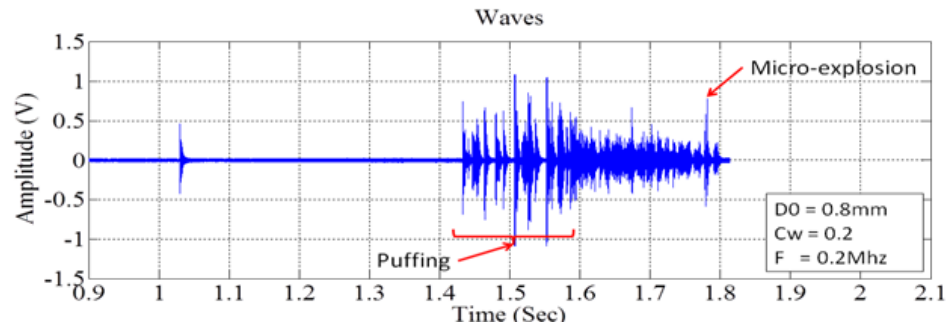

Figure 56. Time response of hexadecane emulsion droplet ($t_{peak\ of\ ME}$ = 1.782 sec).

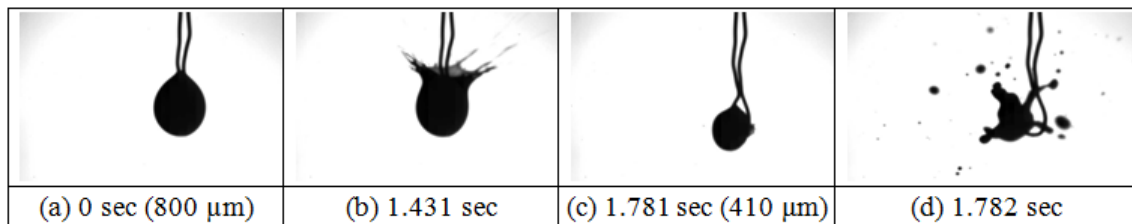| (a) 0 sec (800 μm) | (b) 1.431 sec | (c) 1.781 sec (410 μm) | (d) 1.782 sec |

Figure 57. Microexplosion images of hexadecane emulsion droplet
(a) initial droplet size of 800 μm (b) first puffing (c) decreased droplet size and right before microexplosion event (d) microexplosion.

Microexplosion Frequency Analysis

For the analysis of microexplosion frequencies of hexadecane emulsion experiment, the period of time of interest or when microexplosion had been observed visually was considered as shown in Figure 58 (a). The FFT algorithm explained in section 2.5.1 was used to calculate microexplosion frequency responses from the microexplosion wave signals. Among all the frequency peaks in the FFT spectrum shown

in Figure 58 (b), the microexplosion frequencies after filtering out the noise frequencies
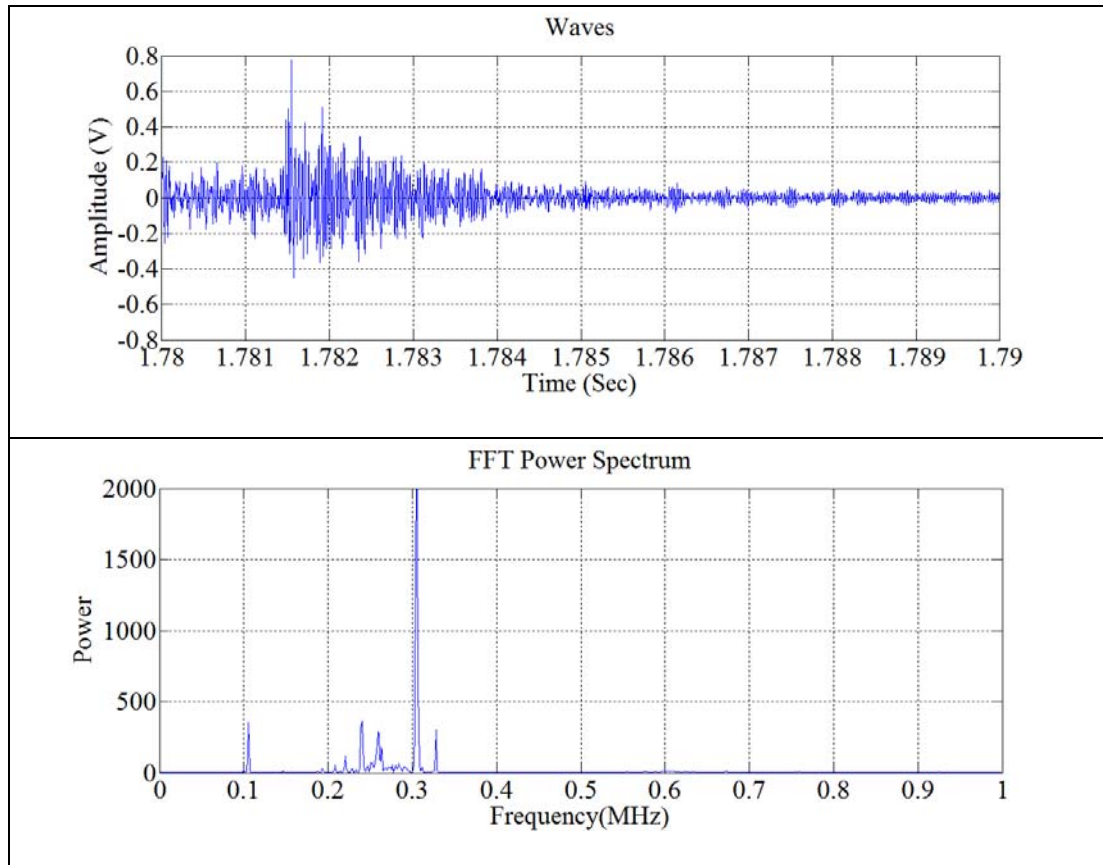were 240 kHz, 260 kHz, 310 kHz and 325 kHz.

Figure 58. Microexplosion of 800 μm diameter hexadecane emulsion droplet (a) time
response (b) frequency response.

To understand the size effect on microexplosion frequency, a smaller hexadecane
droplet of 270 μm was burnt using a flame torch. Due to the smaller droplet size, the
amount of time required for microexplosion significantly reduced compared to that of 800
μm size droplet as shown in Figure 59. As discussed in the previous section, the

distribution of droplets after microexplosion was smaller with smaller initial droplet size.

Figure 60 (a) shows the wave signal for the 270 μm droplet.
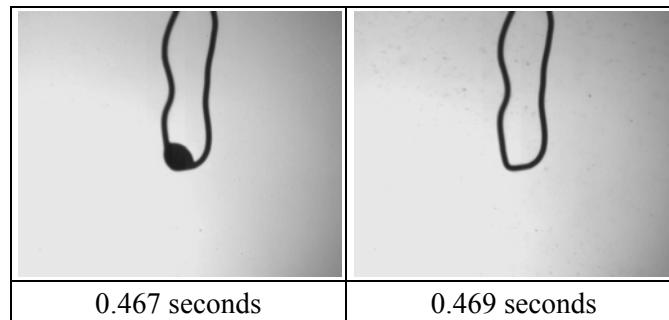

| 0.467 seconds | 0.469 seconds |

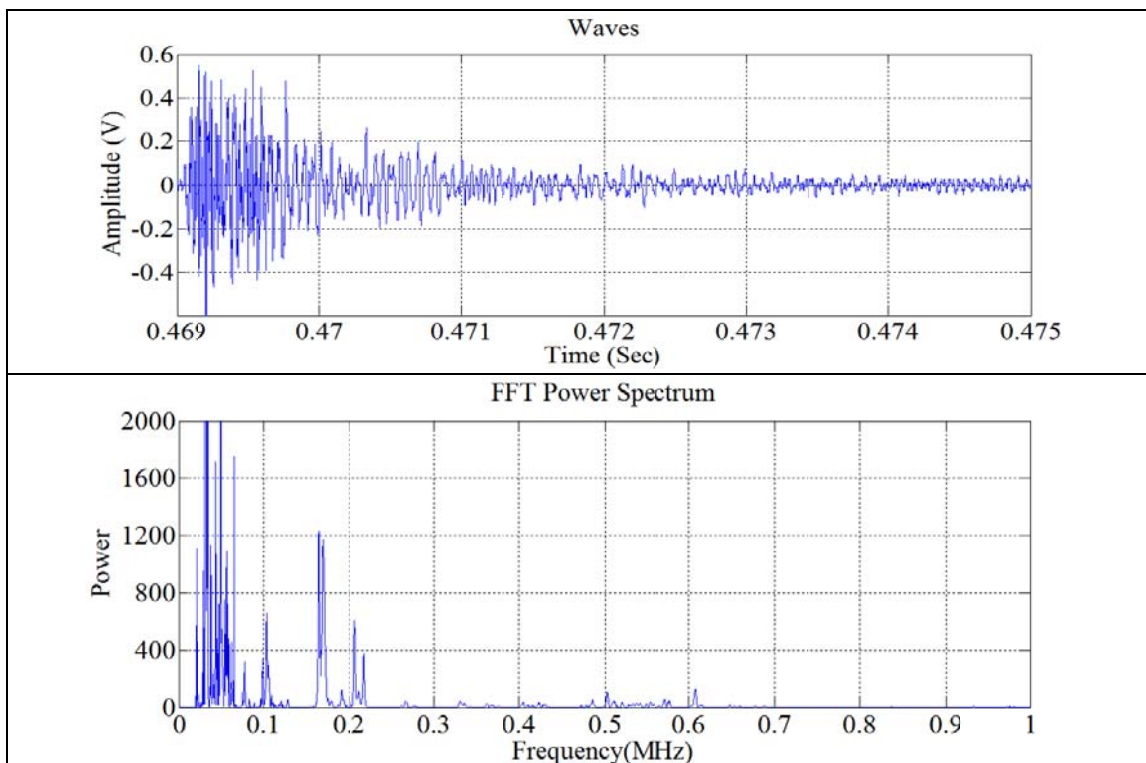Figure 59. Microexplosion of hexadecane emulsion droplet of 270 μm with a flame torch.

Figure 60. Microexplosion of hexadecane emulsion droplet of 270 μm with a flame torch
(a) time response (b) frequency response.

In Figure 60 (b) depicts the frequency spectrum after the microexplosion wave signal of 270 μm size droplet was obtained through the FFT algorithm. By looking at Figures 58 (b) and 60 (b), it is evident that smaller droplets show higher frequency range than larger droplets under the same conditions as depicted in Table 19 and Figure 61. Figure 62 shows a normalized power spectrum plots for both droplet sizes. This phenomenon was explained in section 4 using Equations (19) and (36) which predict that smaller initial droplet size produces weaker microexplosion waves which characteristically exhibit higher frequency.

Table 19: Overview frequency peaks of microexplosion of hexadecane emulsion with a flame torch.

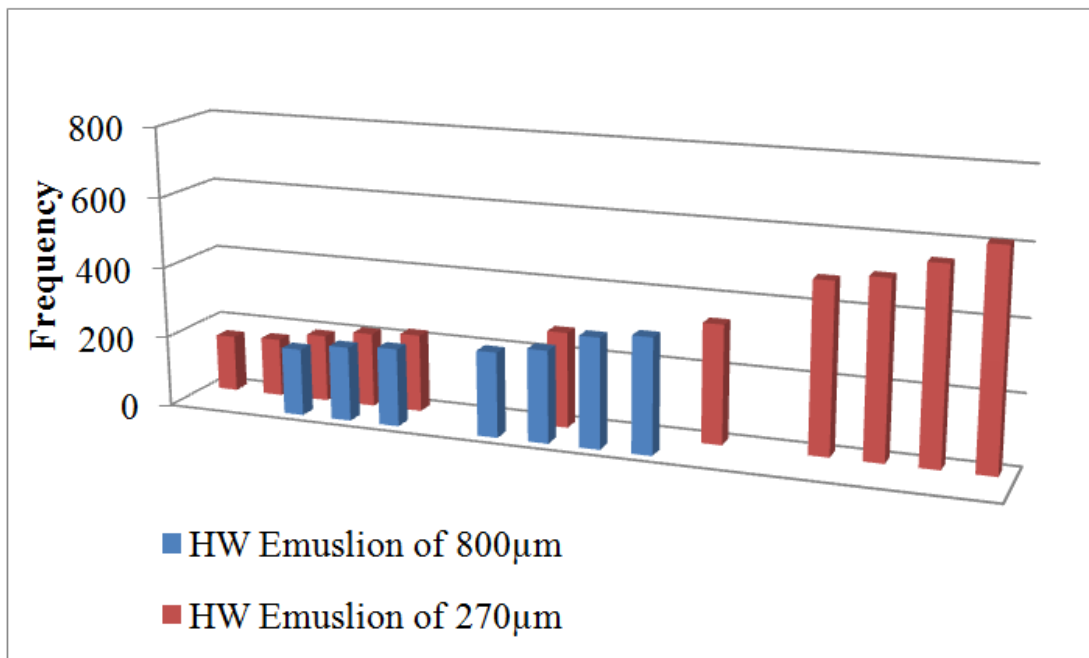| Flame Torch	
Hexadecane Emulsion of 800 μm droplet (kHz)	Hexadecane Emulsion of 270 μm droplet (kHz)
190	190
210	210
220	220
240	
260	270
310	
325	
	335
	480
	500
	550
	610

Figure 61. Frequency comparison of HW emulsion ME at 730 ˚C.

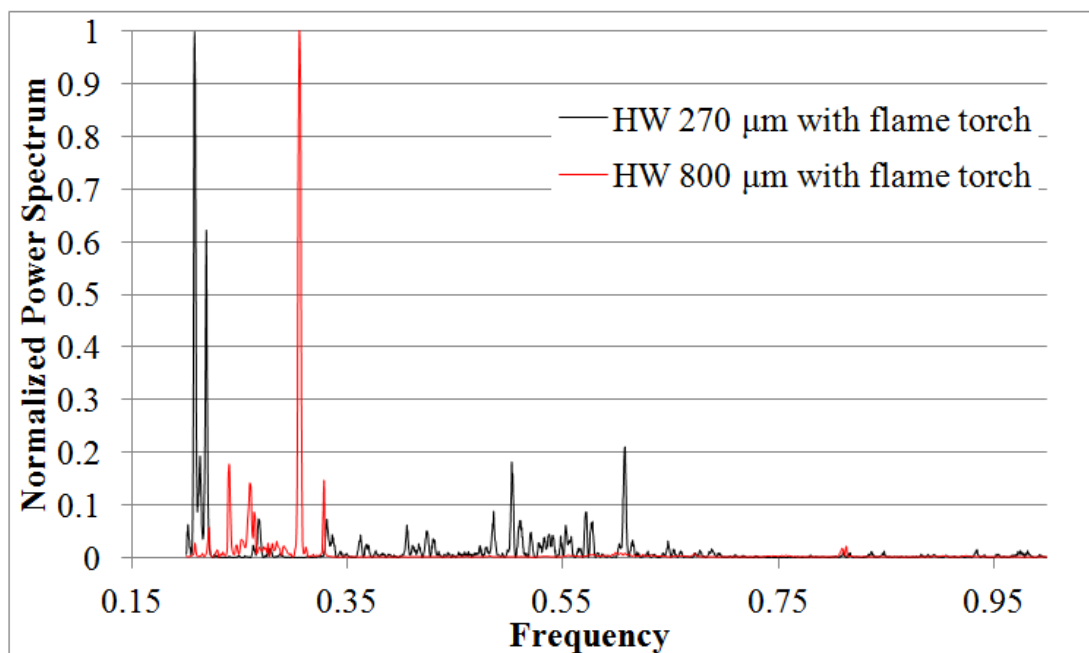Figure 62. Frequency comparison of HW emulsion ME with a flame torch after power spectrum normalization.

Hexadecane Emulsion Droplet in the Furnace

To understand the effect of chamber temperatures on emulsified droplet microexplosion, the experiments were conducted using the custom-made electric furnace or chamber. Experiments with two hexadecane emulsion droplets of 363 μm and 224 μm were conducted for frequency analysis. As shown in Figures 63 and 64, both hexadecane emulsions exploded into very fine droplet sizes. However, the distribution of droplet size after microexplosion of the 224 μm droplet was smaller than that of 363 μm droplet also the amount of time required for microexplosion for the 313 μm droplet took longer than the smaller one.
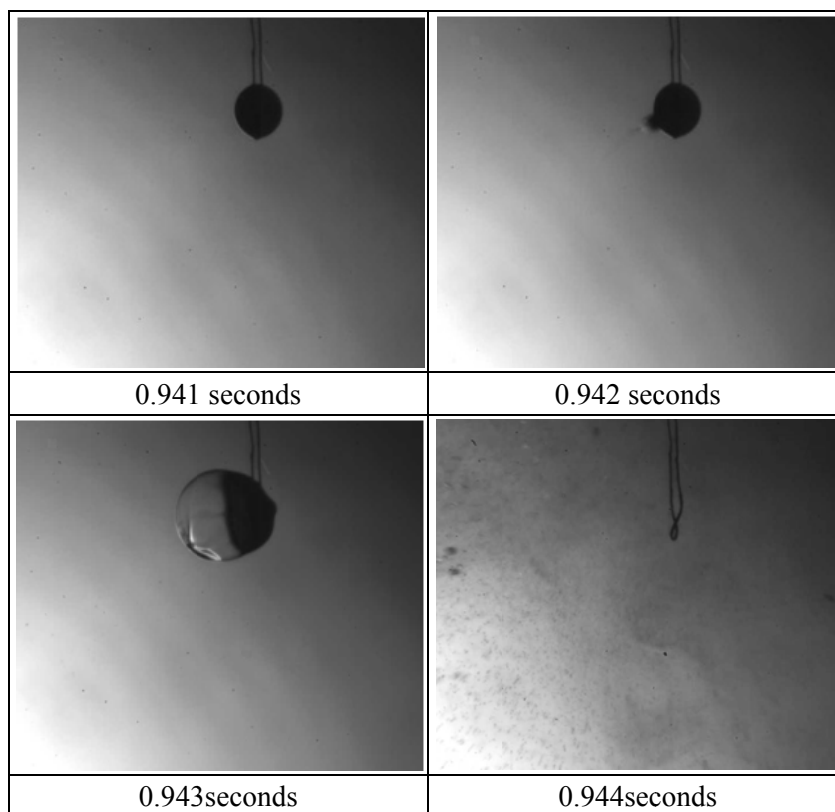

| 0.941 seconds | 0.942 seconds |
| 0.943seconds | 0.944seconds |

Figure 63. Microexplosion of hexadecane emulsion droplet of 313 μm diameter at 730 ˚C.
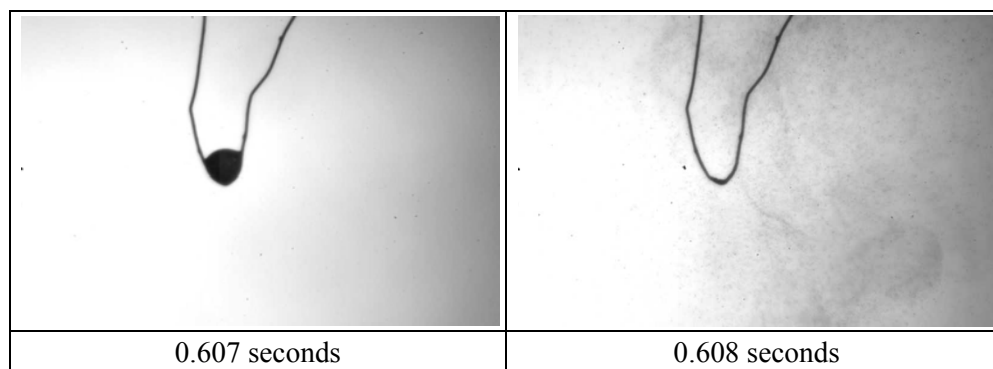
Figure 64. Microexplosion of hexadecane emulsion droplet of 224 μm at 730 ˚C.

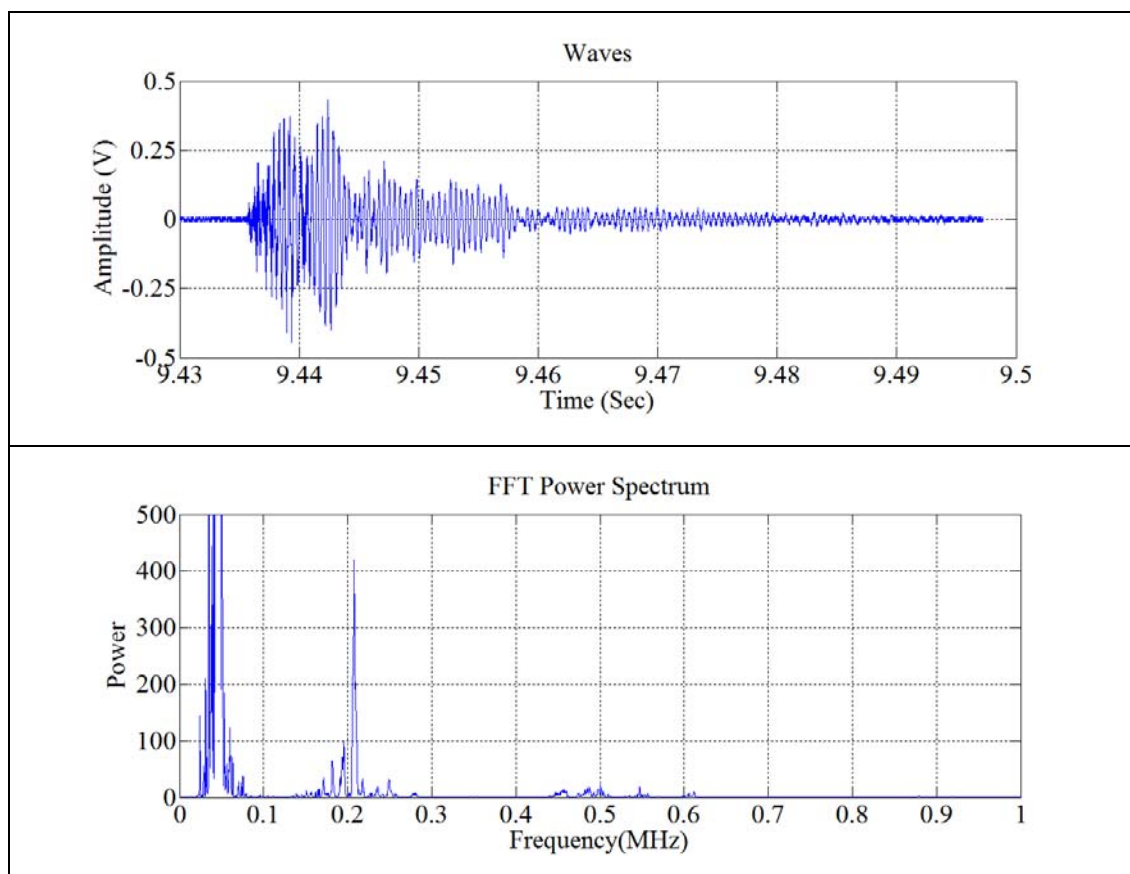Figure 65. Microexplosion of hexadecane emulsion droplet of 313 μm at 730 ˚C
(a) time response (b) frequency response.
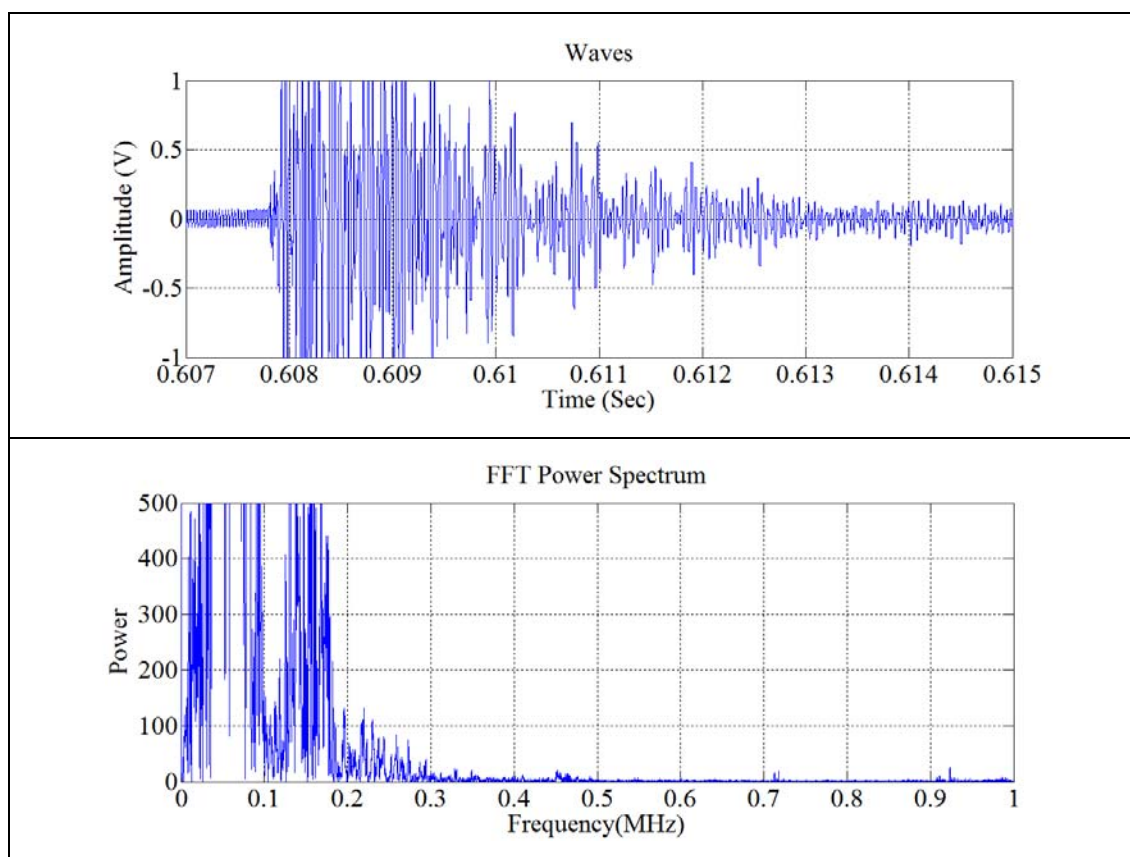
Figure 66. Microexplosion of hexadecane emulsion droplet of 224 μm at 730 ˚C
(a) time response (b) frequency response.

The characteristic microexplosion frequencies of both droplets depicted in Figures 65 (b) and 66 (b) were tabulated after filtering out the noise frequency of Pt stick, Pt wire and cooling pipe as shown in Table 20. Any frequency peak regardless of the level of power spectrum cannot be ignored since the sum of every peak on the frequency domain represents the whole microexplosion process. From Table 20 and Figure 67, it can be seen that the frequency range was highly dependent on the size of initial droplet diameter which directly affected the microexplosion strength. As the size of initial droplet diameter decreased, the frequency ranges also decreased as explained by Equations (19) and (36).

Therefore, the shift is frequency spectrum can be used to estimate the effect of ambient conditions on the droplet size distribution after microexplosion. Figure 68 shows a normalized power spectrum plots for both droplet sizes of 313 μm and 224 μm.

Table 20. Overview frequency peaks of microexplosion events of hexadecane emulsion at 730 ˚C.

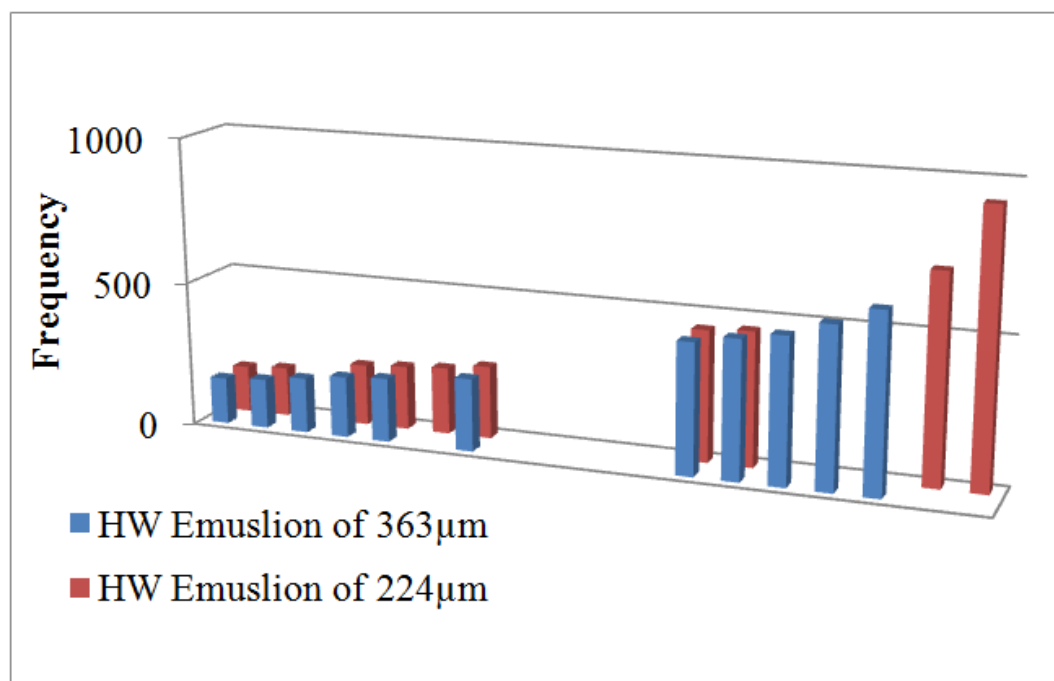| Electric Furnace	
Hexadecane Emulsion of 313 μm droplet (kHz)	Hexadecane Emulsion of 224 μm droplet (kHz)
160	160
170	170
190	
210	210
220	220
	230
250	250
450	450
475	470
500	
550	
610	
	720
	930

Figure 67. Frequency comparison of hexadecane emulsion ME at 730 ˚C.
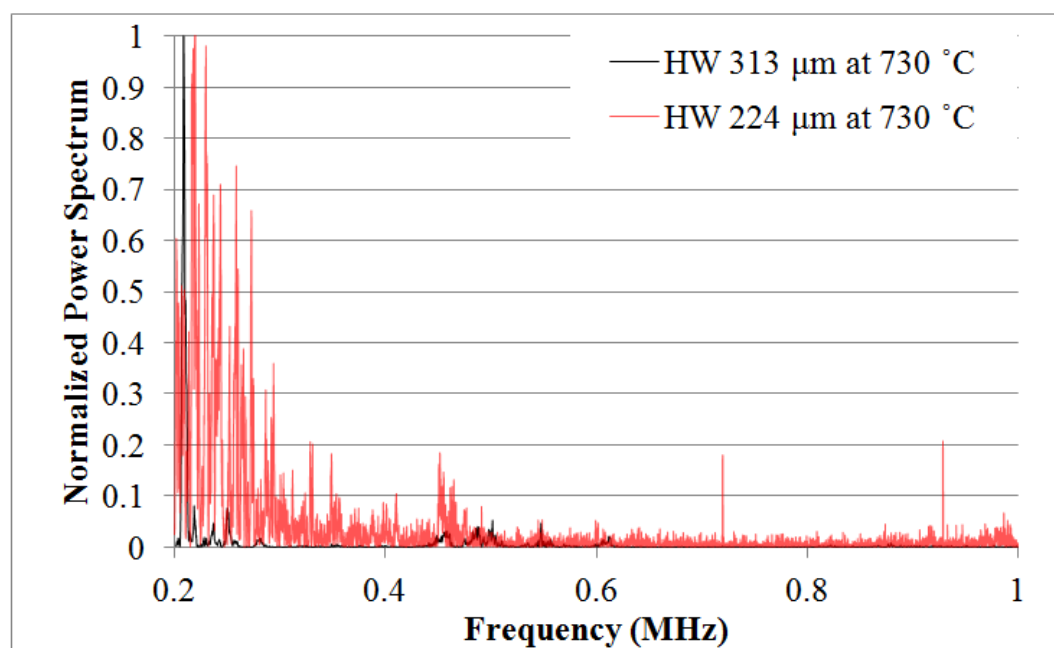

Figure 68. Frequency comparison of HW emulsion ME at 730 ˚C after power spectrum normalization.

5.3.3 Analysis of Single Bubble Microexplosion of Methanol-in-Canola Emulsion

The frequency study of the methanol-in-canola emulsion (CM 90/10 and CM 85/15) was performed with four conditions (CM 85/15 of 313 μm at 980 ˚C, CM 85/15 of 300 μm at 900 ˚C, CM 90/10 of 298 μm at 900 ˚C and CM 90/10 of 233 μm at 900 ˚C). With the four conditions, the effect of temperatures on the microexplosion frequency was first studied with the similar droplet sizes and same compositions. Then the effect of different concentration of methanol on the microexplosion frequency was conducted at the same temperatures and similar droplet sizes. Lastly, the effect of different sizes on the microexplosion frequency is discussed.

First, the microexplosion experiment of CM 85/15 emulsion droplet of 313 μm was performed at 980 ˚C. As Figure 69 shows puffing event occurred at 2.252 seconds and then the droplet expanded until 2.351 seconds. Time response and frequency of CM 85/15 droplet of 313 μm at 980 ˚C is shown in Figure 70. With different CM 85/15 droplets of 300 μm, microexplosion experiments were carried out at 900 ˚C as depicted in Figure 71. With frequency analysis in Figures 70 (b) and 72 (b), only two characteristic frequencies (195 kHz and 325 kHz) could be identified during process. The frequency range at 900 ˚C was similar to that at 980 ˚C. This explains that the effect of temperatures on the microexplosion strength is relatively weak. Fu et al. [26] previously identified that temperatures are independent of microexplosion strength once the internal high vapor fluid reaches the superheat temperature. However, temperature also causes an increase in the probability of microexplosion as discussed above. Figure 73 shows a normalized power spectrum of both droplets at different temperatures.
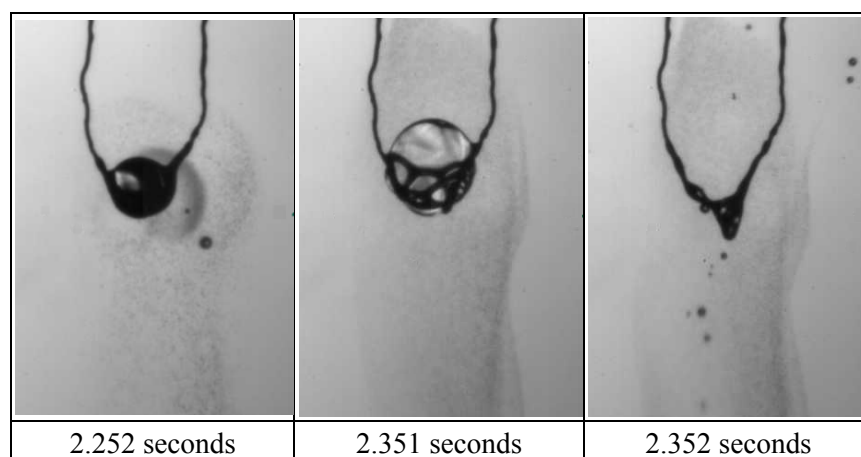
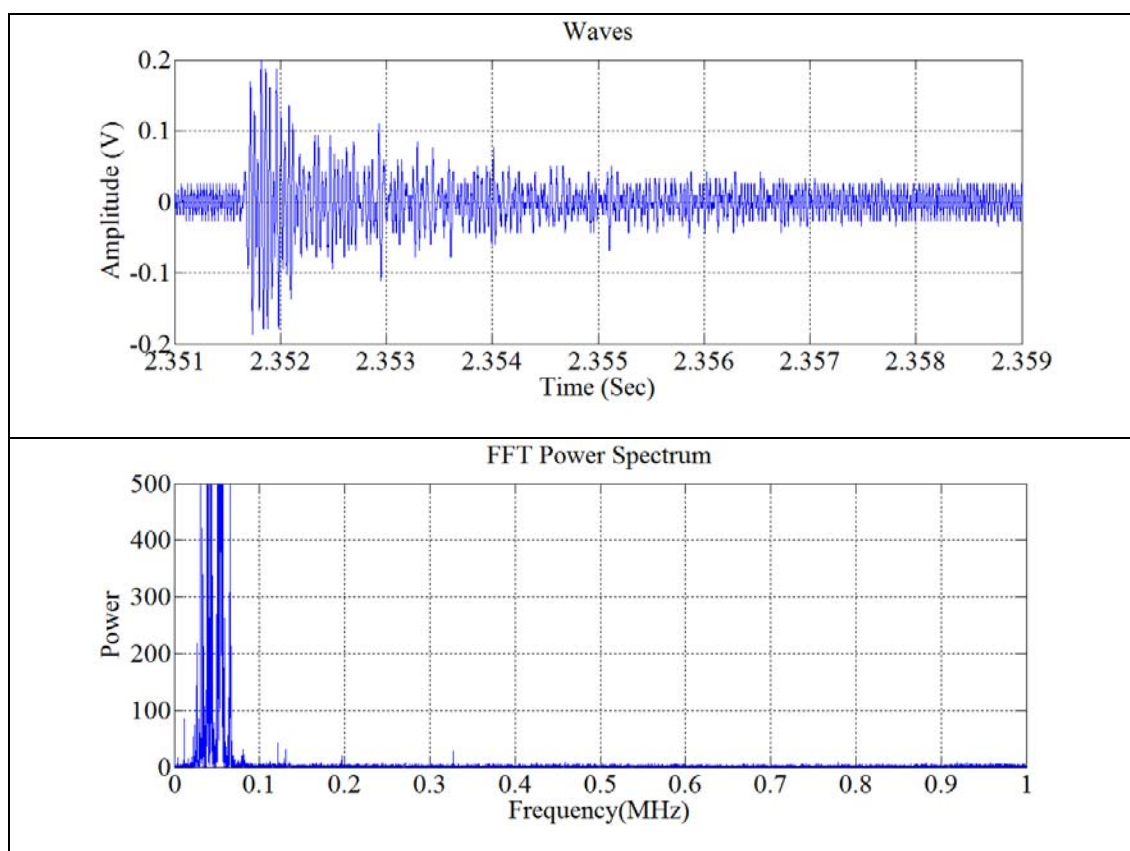| 2.252 seconds | 2.351 seconds | 2.352 seconds |

Figure 69. CM 85/15 emulsion droplet of 313 μm at 980 ˚C.

Figure 70. Microexplosion of CM 85/15 droplet of 313 μm at 980 ˚C (a) time response (b) frequency response.
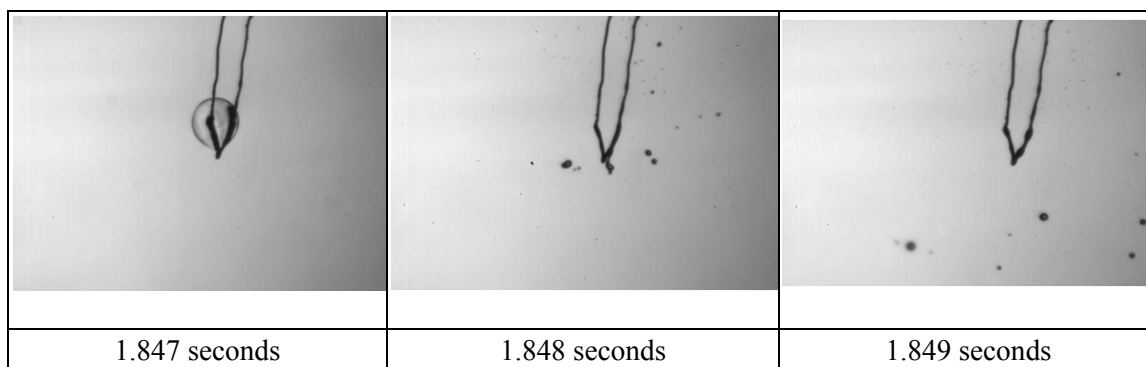
Figure 71. CM 85/15 emulsion droplet of 300 μm at 900 ˚C.
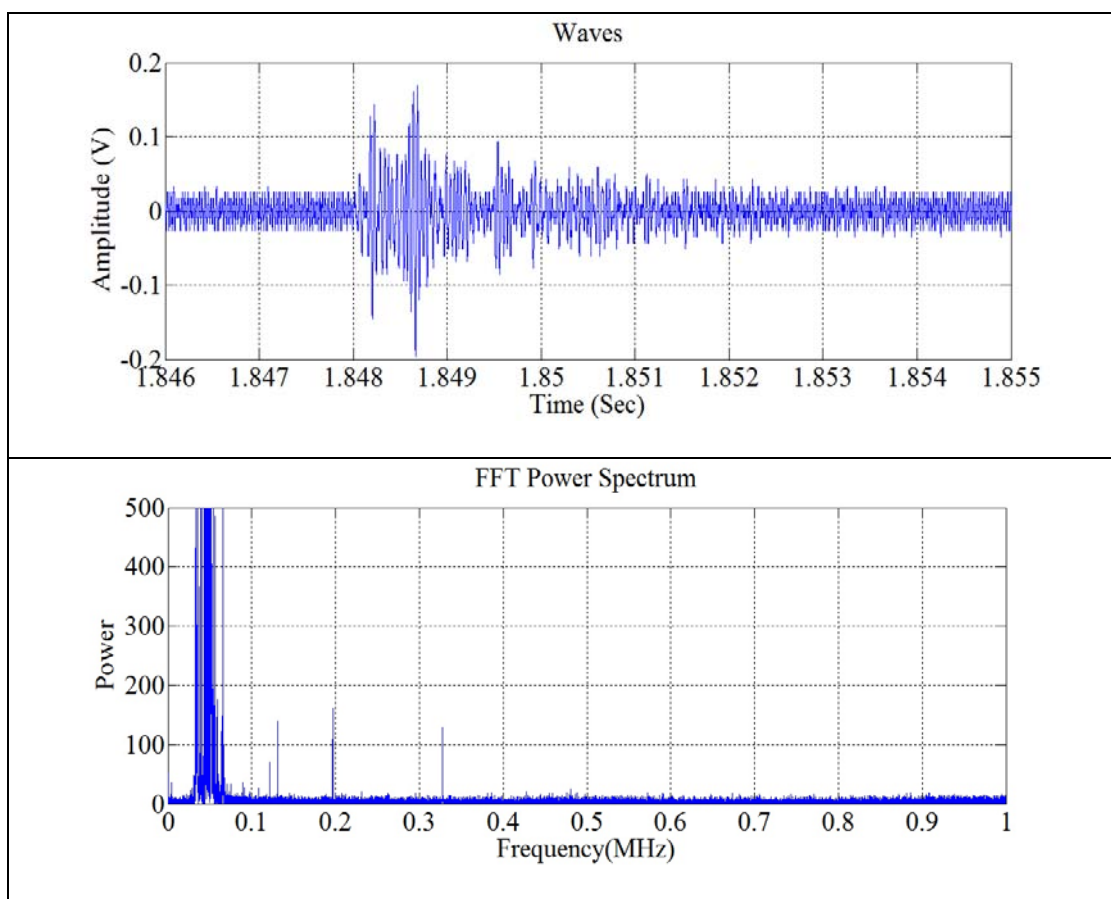

Figure 72. Microexplosion of CM 85/15 droplet of 300 μm diameter at 900 ˚C
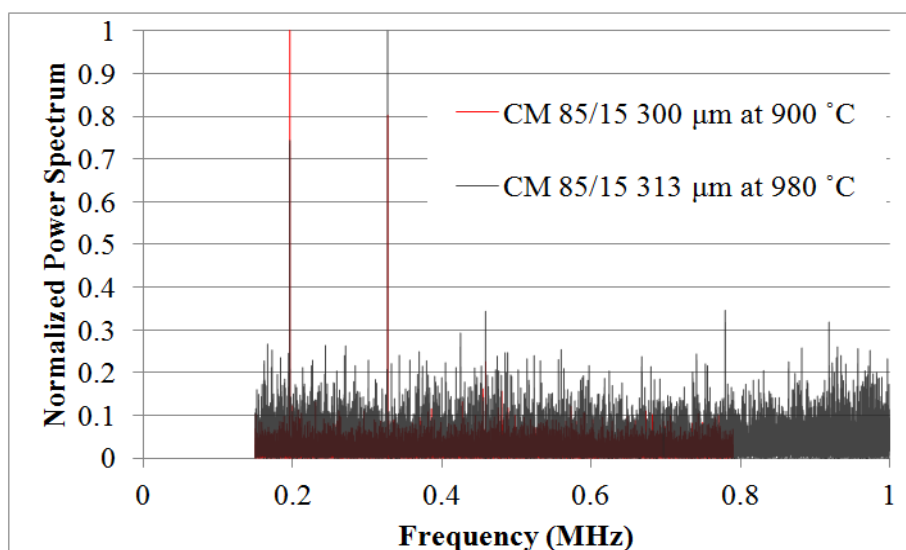(a) time response (b) frequency response.

Figure 73. Frequency comparison of CM emulsion ME at different temperatures after power spectrum normalization.

Next, the effect of methanol concentration on the microexplosion frequency was studied. An experiment with CM 90/10 droplet of 298 μm was conducted at 900 ˚C as shown in Figure 74. After FFT analysis, peaks of frequencies around 160 kHz, 190 kHz, 260 kHz and 325 kHz were detected as shown in the Figure 75 (b). The frequency ranges of CM 90/10 emulsion are similar to those of CM 85/15 as shown in Figure 72 (b). This suggests that different composition has little effect on the microexplosion frequencies, which means that microexplosion strength is not affected by emulsion composition. However, this contradicts the findings by Fu et al. [26] where they claimed that microexplosion strength varies with the concentration of water. However, the characteristic frequencies are for methanol as the high vapor pressure liquid and not for water. Moreover, the surface between canola oil and water and canola oil and methanol are markedly different which should have a direct effect on the required Laplace pressure

to induce a microexplosion event. Figure 76 shows a normalized frequency comparison of

CM emulsion of different composition.

| 1.381 seconds | 1.382 seconds |
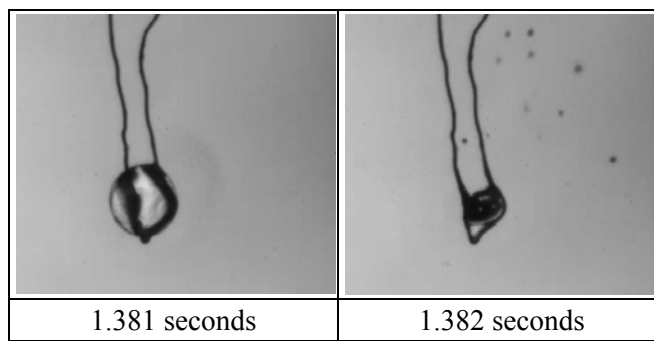
Figure 74. CM 90/10 emulsion droplet of 298 μm at 900 ˚C.
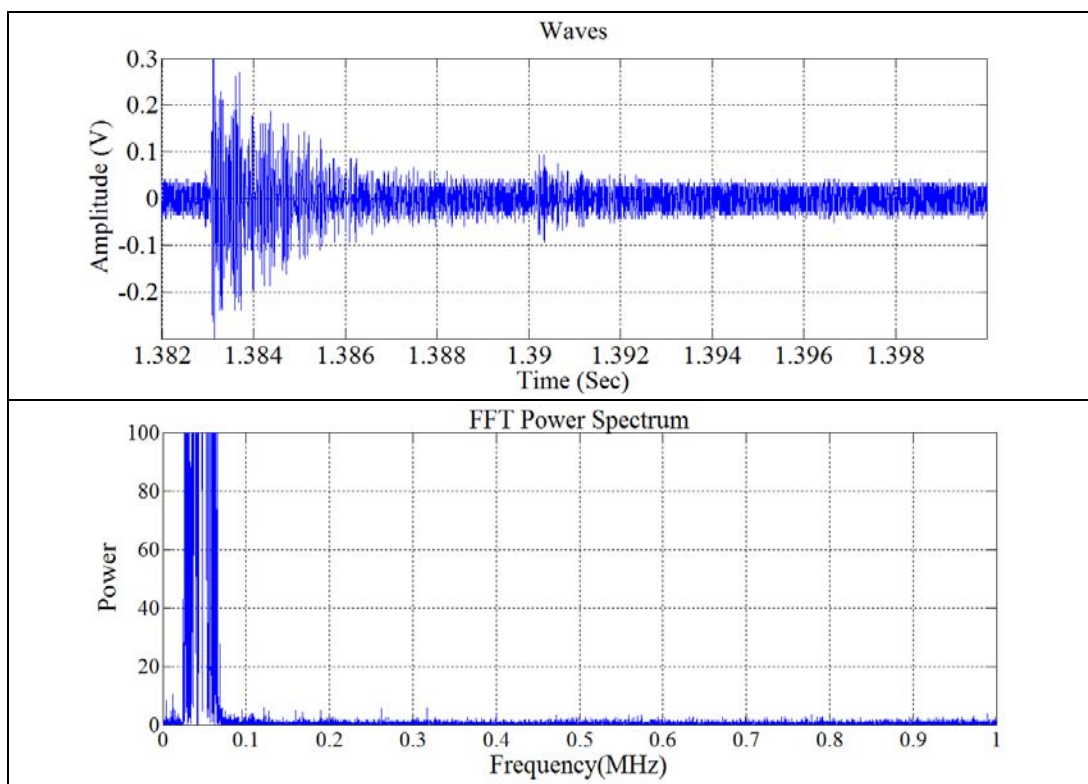
Figure 75. Microexplosion of 298 μm diameter of CM 90/10 droplet at 900 ˚C
(a) time response (b) frequency response.
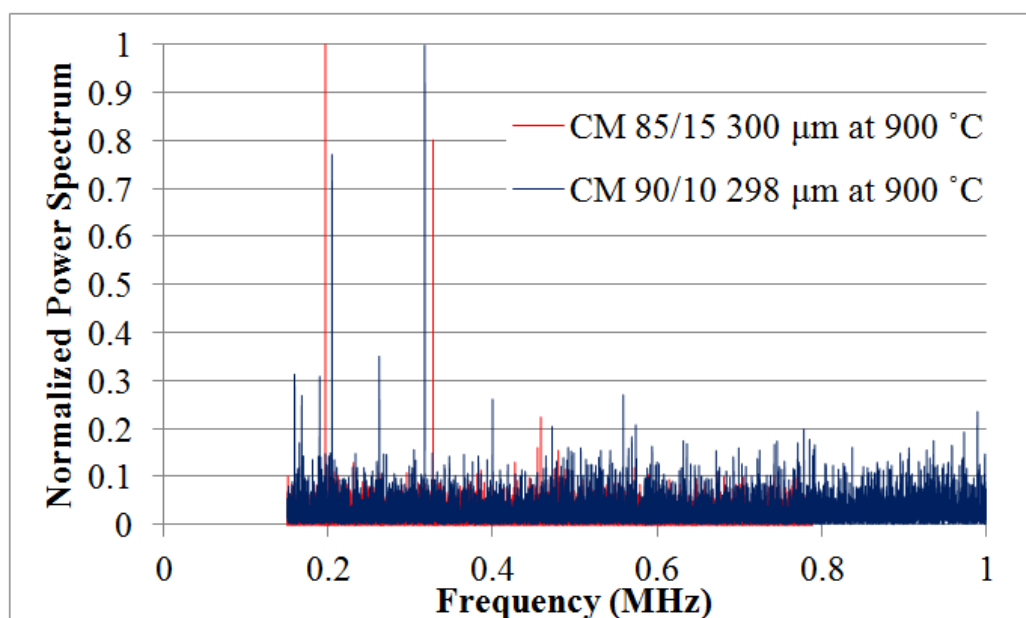
Figure 76. Frequency comparison of CM emulsion ME at different emulsion compositions after power spectrum normalization.

Finally, the study of the effect of droplet size on microexplosion was conducted by comparing the previous three experiments. Both Figures 77 and 78 (a) show the same time at which microexplosion took place. The 233 µm CM emulsion droplet showed the broadest frequency ranges among all the experiments as shown in Figure 78 (b). This suggests that microexplosion strength of CM 90/10 of 233 µm droplet size is the weakest one among the others.
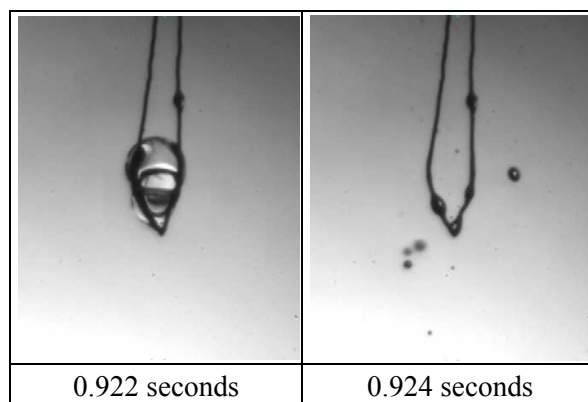
Figure 77. CM 90/10 emulsion droplet of 233 μm at 900 ˚C.
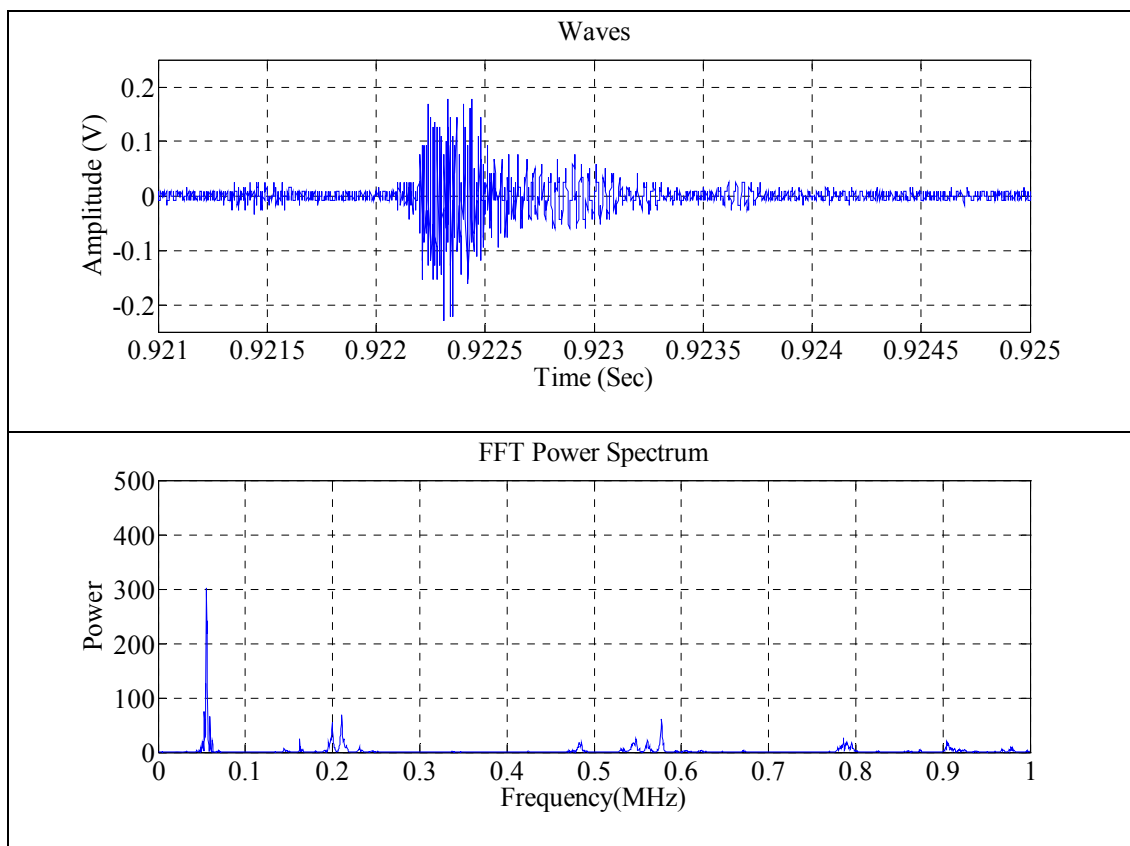
Figure 78.Microexplosion of CM 90/10 droplet of 233 μm at 900 ˚C (a) time response (b) frequency response.

Table 21 and Figure 79 depict the effects of emulsified droplet size, fuel composition and temperature on the characteristics microexplosion frequencies. All the frequency peaks after filtering out the noise were tabulated. A larger range of frequencies was found with smaller emulsion droplets (around 233 μm) when compared to bigger droplets (300 μm). Figure 80 shows the frequency of CM emulsion ME after power spectrum normalization.

Table 21. Overview of microexplosion frequency of CM emulsion.

Microexplosion Frequencies			
CM 85/15 of 313 μm at 980 ˚C (kHz)	CM 85/15 of 300 μm at 900 ˚C (kHz)	CM 90/10 of 298 μm at 900 ˚C (kHz)	CM 90/10 of 233 μm at 900 ˚C (kHz)
		160	160
195	195	190	200
		260	
325	325	325	
			480
			550
			560
			575
			780
			790
			910

Figure 79. Frequency comparison of CM emulsion ME.
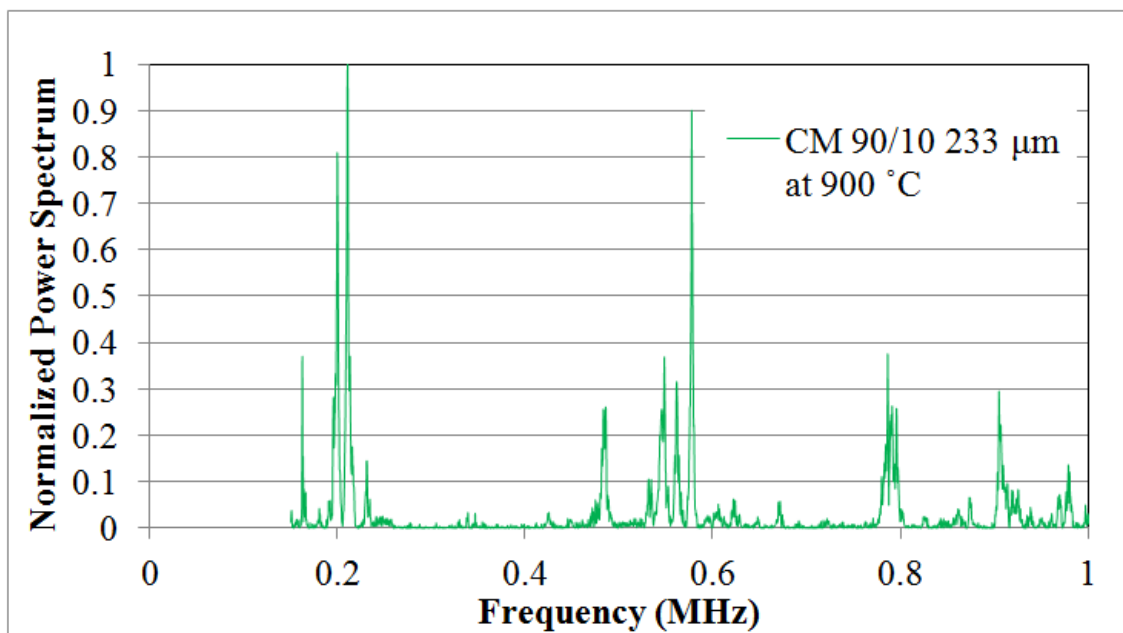
Figure 80. Frequency of CM emulsion ME of 233 μm after power spectrum normalization.

5.3.4 Analysis of Microexplosion of Water-in-Canola Emulsion

Microexplosion experiments with two different CW emulsion droplets were conducted at 900 ˚C. As depicted in Figure 81, the large initial droplet of 334 μm exploded partially at 1.215 seconds and it shrank until higher inner pressures were reached. Then complete microexplosion took place when the critical inner pressure was reached again at high surface tension. The time response and frequency response of CW 90/10 droplet of 334 μm are shown in Figure 82. In the case of a 202 μm droplet seen in Figure 83, only one microexplosion occurred without droplet expansion.

| 1.137 seconds | 1.214 seconds | 1.215 seconds | 1.216 seconds |
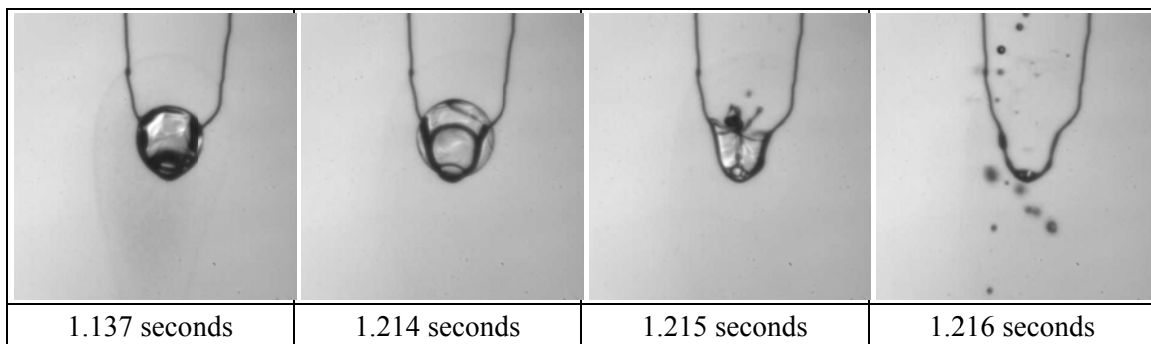
Figure 81. CW 90/10 emulsion droplet of 334 μm.
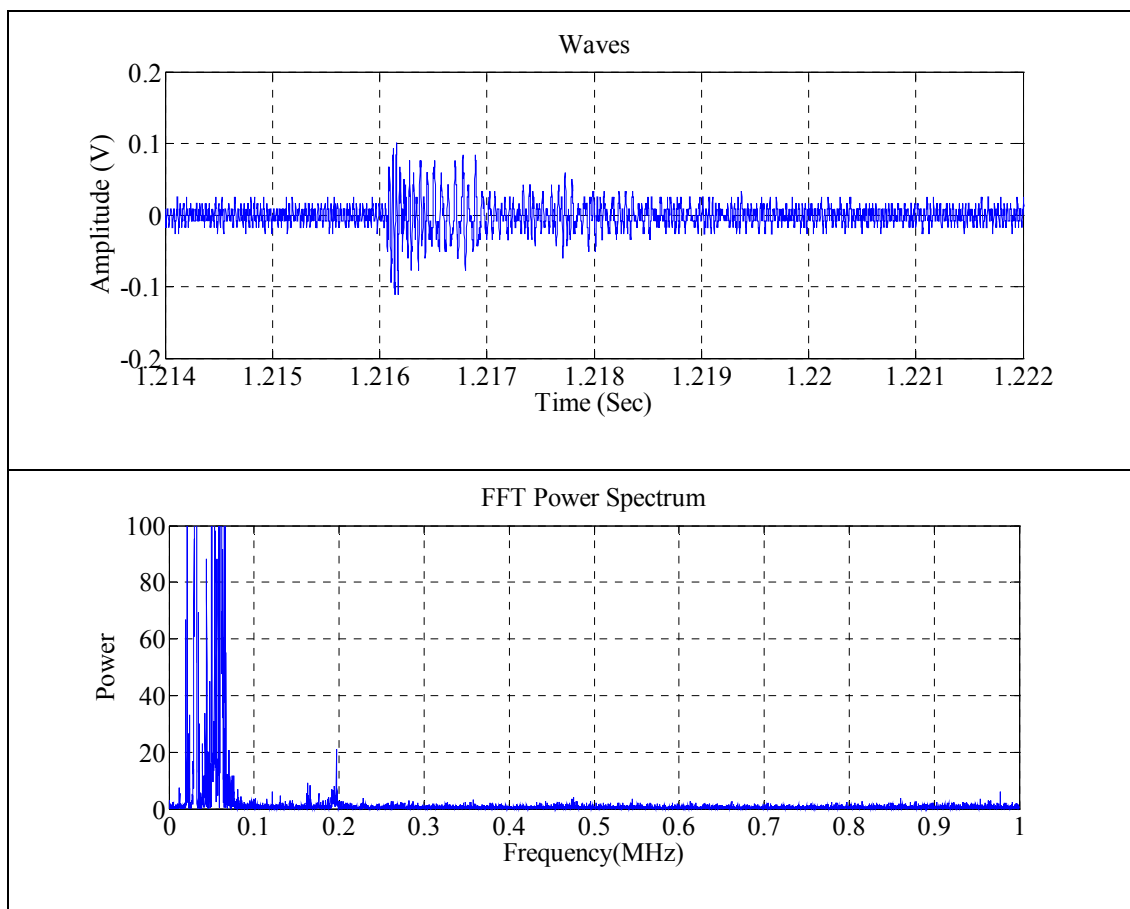
Figure 82. Microexplosion of 334 μm diameter of CW 90/10 droplet burned at 980 ˚C (a) time response (b) frequency response.

| 2.050 seconds | 2.051 seconds | 2.053 seconds |
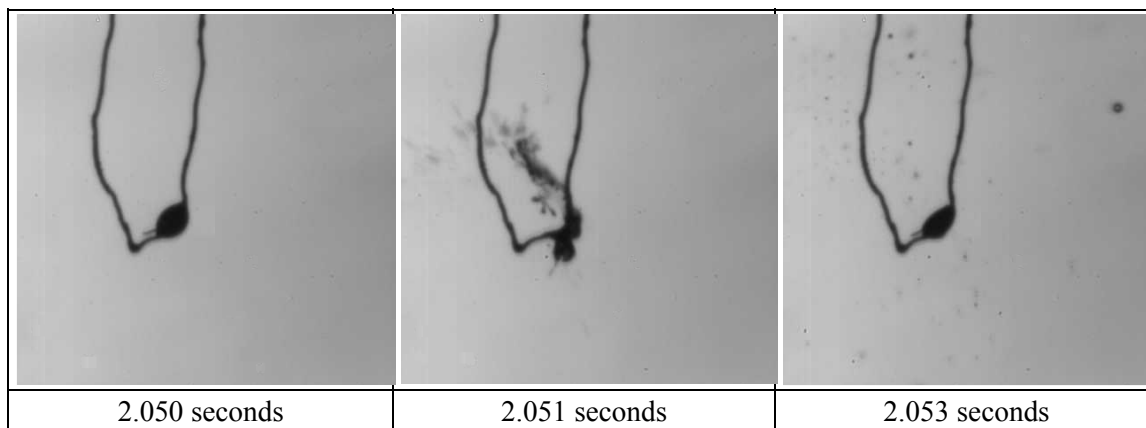
Figure 83. CW 90/10 emulsion droplet of 202 μm.
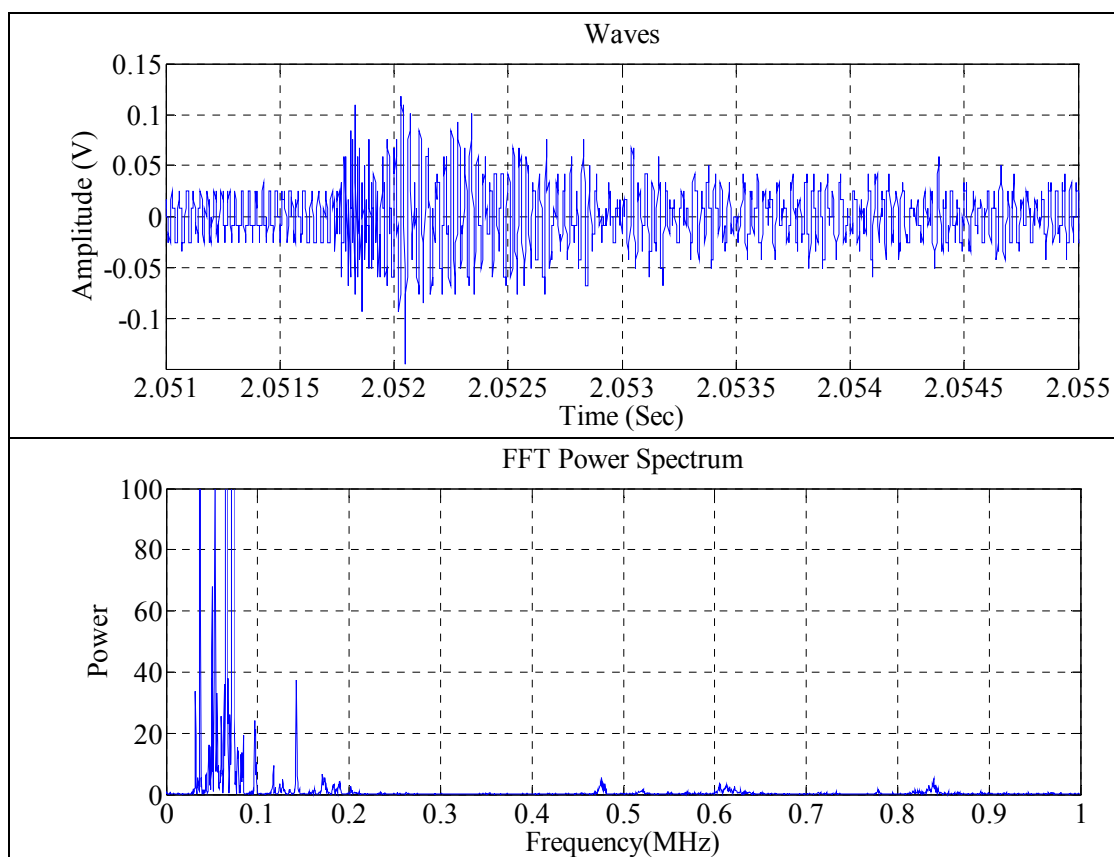
Figure 84. Microexplosion of 202 μm diameter of CW 90/10 droplet burned at 980 ˚C
(a) time response (b) frequency response.

Analysis of the frequencies generated by microexplosion of CW emulsion at 900 ˚C was also undertaken as shown in Figures 82 (b) and 84 (b). The microexplosion behavior of CW emulsion was very similar as in the case of other fuel blends. It also showed that smaller initial droplet causes weaker microexplosion resulting in broader frequencies. As depicted in Table 22 and Figure 85, microexplosion frequencies of 334 μm droplet were in the range of 160 kHz to 225 kHz while for the 202 μm droplet were found in the range from 140 μm to 850 μm. Thus, the frequency characteristics of CW

microexplosion confirm the fact that smaller droplets generate higher frequencies than larger droplets. Figure 86 shows a normalized power spectrum plot for both droplet sizes.

Table 22: Overview of microexplosion frequency of CW emulsion in different size.

CW 90/10 of 313 μm at 980 ˚C (kHz)	CW 90/10 of 202 μm at 980 ˚C (kHz)
170	170
	180
200	200
225	
	475
	525
	600
	625
	850
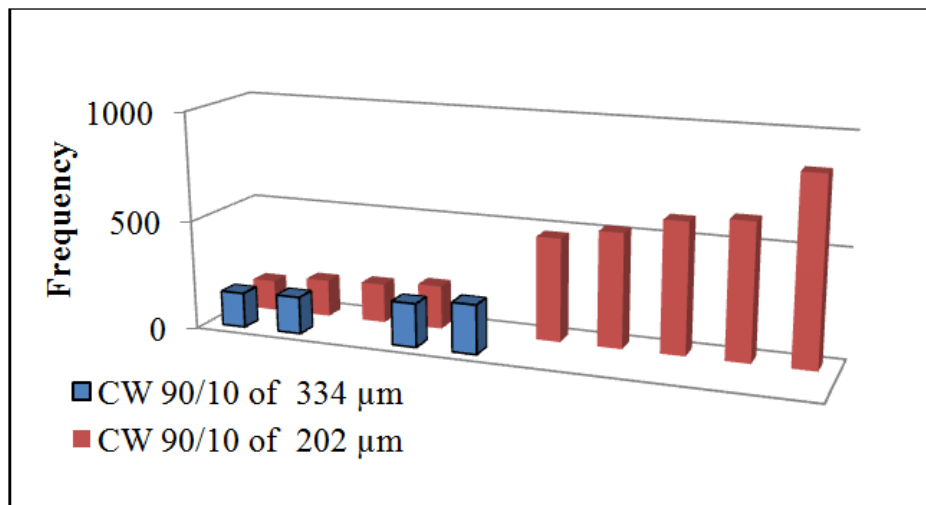
Figure 85. Frequency comparison of CW emulsion ME.
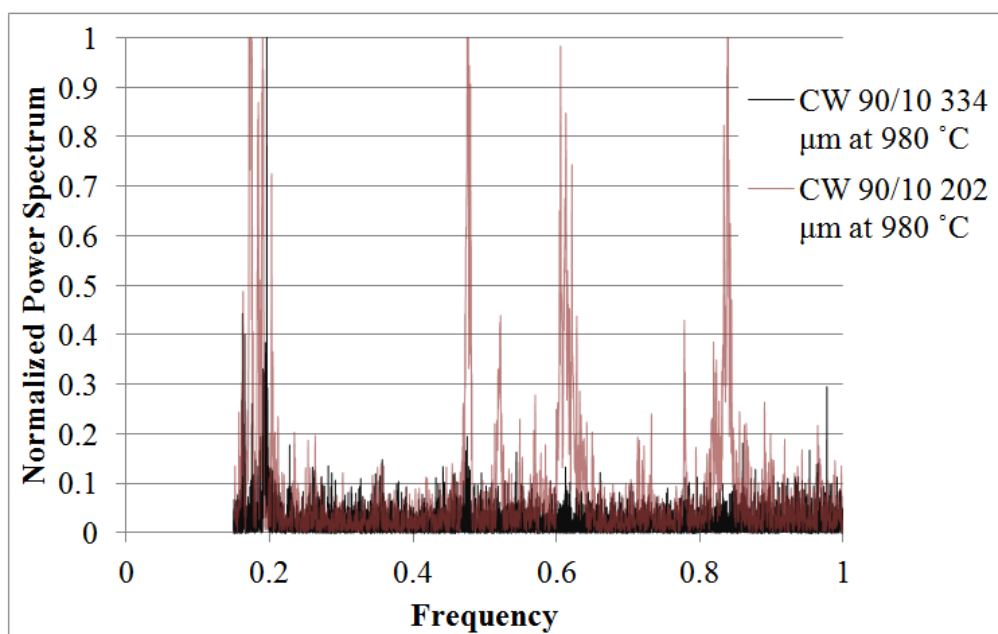
Figure 86. Frequency comparison of CW emulsion ME after power spectrum normalization.

6. CONCLUSIONS

Through this research project, a study was conducted to understand the influence of chamber temperatures, initial droplet size and initial fuel composition on microexplosion of CM 90/10, CM 85/15, CW 90/10, HW emulsion droplets ranging from 150 μm to 350 μm. Also the frequency characteristics of microexplosion were studied. The major conclusions of this research project are explained below.

6.1 Probability of Microexplosion

1. Higher temperatures and higher concentration of high vapor pressure fluid (methanol and water) in each emulsion leads to higher probabilities of microexplosion due to the sudden expansion of high vapor pressure fluids inside each droplet.

2. At constant temperature, the probability of microexplosion of CW emulsion is greater than for CM emulsion due to larger surface tension. Water requires greater internal pressures to counteract its high surface tension leading to a super critical state instead of simply evaporating from each droplet.

3. For all the blend compositions, smaller droplets depict a greater probability of microexplosion than larger droplets.

4. The probability of puffing probability of all emulsions at higher temperatures was less than those at lower temperatures. This was because under high temperature conditions, the high vapor pressure fluid within the emulsified droplets underwent complete evaporation or resulted in microexplosion without puffing.

6.2 Secondary Distributed Droplets

1. Two types of swelling or expansion mechanisms before microexplosion were defined with CM emulsion including the single bubble swelling and the multi-bubble swelling phenomena. It was evident that greater concentration of methanol and the lower temperatures of CM emulsion led to higher rate of multi-bubble microexplosion.

2. For all the blends, the larger initial droplet size led to the larger average size of distributed droplets after microexplosion because of surface tension effects. However, emulsion droplet with larger concentration of high vapor pressure fluid led to finer droplets after microexplosion.

3. For the study of fine droplet below 10 μm in size of CM and hexadecane emulsions, a higher percentage of fine droplets were formed by a greater concentration of high vapor pressure fluid. Also, smaller initial droplet size resulted in a greater number of finer droplets. However, in CW emulsions, initial droplet size did not considerably affect the amount of fine droplets formed after microexplosion.

4. It was also observed that after the first microexplosion event, large microexploded droplets continued to microexploded.

6.3 Signal Analysis

1. In hexadecane emulsion, smaller droplet sizes showed broader frequencies regardless of the burning apparatus used during microexplosion.

2. In case of CM emulsion, the effect of temperatures and the different concentration of methanol in emulsion droplet showed similar microexplosion frequency ranges which means that temperature and concentration had little effect on the microexplosion frequencies.

3. The effect of droplet size on microexplosion frequency was significant. Larger emulsion droplets produced lower frequencies. Microexplosion strength always increased as emulsion droplet size increased and microexplosion frequencies decreased.

6.4 Future Work

This study was helpful in finding optimal conditions for microexplosion and puffing events of CM, CW and HW emulsions. The microexplosion characteristics for each emulsion were defined and correlated with the microexplosion strength. However, further studies are needed to determine the effect of using even smaller droplets on microexplosion. The following subjects of research should be considered in the future.

1. Emulsion with higher concentration of methanol and water should be studied to determine their effects on microexplosion phenomena and frequency.

2. Influence of temperatures higher than 980 ˚C on the microexplosion and puffing phenomena should be studied as well.

3. Smaller droplet sizes should be studied as well.

4. Emissions measurements after microexplosion events should be undertaken to assess the effect of microexplosion of pollutant formation.

5. Frequency characteristics of microexplosion need to be studied using wavelet transform which can be used to show the relations between frequency, power spectrum and intensity.

REFERENCES

[1]   H. Mollet, A. Grubenmann, Formulation Technology: Emulsions, Suspensions, Solid Forms, Wiley-VCH, New York, 2001.

[2]   P. Becher, Encyclopedia of Emulsion Technology Vol. 1 Basic Theory, Marcel Dekker Incorporated, New York, 1983.

[3]   T.F. Fadros, Emulsion Science and Technology, Wiley-VCH, New York, 2009.

[4]   W.C. Griffin, Classification of surface-active agents by HLB, Journal of the Scociety of Cosmetic Chemists 1 (1949) 311-326.

[5]   K. Annamalai, I.K. Puri, Combustion Science and Engineering, CRC Press, Boca Raton, Florida, 2007.

[6]   S.M. Bhimani, Experimental characterization of canola oil emulsion combustion in a modified furnace, M.S. Thesis, Texas A&M University, College Station, 2011.

[7]   V.M. Ivanov, P.I. Nefdov, Experimental investigation of the combustion process in nature and emulsified fuels, NASA TT F-258 (1965).

[8]   T. Houlihan, The triple crown, Power Engineering 4 (2009) 44-45.

[9]   C.K. Law, Combustion Physics, Cambridge University Press, Cambridge, 2006.

[10] T. Kadota, H. Yamasaki, Recent advances in the combustion of water fuel emulsion, Progress in Energy and Combustion Science 28 (2002) 385-404.

[11] F.L. Dryer, Water addition to practical combustion systems - concepts and applications, International Symposium on Combustion 16 (1977) 279-295.

[12] F.A. Williams, Combustion Theory: Second Edition, Addison-Wesley, Reading, Massachusetts, 1985.

[13] J. Henrych, The Dynamics of Explosion and Its Use, Elsevier Scientific Publishing Company, Amsterdam, 1979.

[14] M. Tsue, T. Kaota, D. Segawa, H. Yamasaki, Statistical analysis on onset of microexplosion for an emulsion droplet, International Twenty-Sixth Symposium on Combustion, The Combustion Institute (1996) 1629-1635.

[15] H. Watanabe, T. Harada, K. Hoshino, Y. Matsushita, H. Aoki, T. Miura, An experimental investigation of the characteristics of the secondary atomization and spray combustion for emulsified fuel, Journal of Chemistry Engineering 41 (2008) 1110-1118.

[16] T. Harada, H. Watanabe, Y. Matsushita, S. Tanno, H. Aoki, T. Miura, The effect of water/n-dodecane emulsified fuel droplet temperature and initial diameter on secondary atomization, Kagaku Kogaku Ronbunshu 34 (2008) 161-167.

[17] M. Takei, T. Tsukamoto, T. Niioka, Ignition of blended-fuel droplet in high-temperature atmosphere, Combustion and Flame 93 (1993) 149-156.

[18] L. Ferrante, M. Miccio, F. Miccio, R. Solimene, Fluidized bed combustion of liquid biofules: Application of integrated diagnostics for microexplosions characterization, Energy & Fuels 22 (2008) 4213-4222.

[19] C.H. Wang, C.K. Law, Microexplosion of fuel droplets under high pressure, Combustion and Flame 59 (1985) 53-62.

[20] Y. Morozumi, Y. Saito, Effect of physical properties on microexplosion occurrence in water-in-oil emulsion droplets, Energy Fuels 24 (2010) 1854-1859.

[21] P. McIntire, R.K. Miller, Nondestructive Testing Handbook Vol. 5 Acoustic Emission Testing: Second Edition, American Society for Nondestructive Testing, Columbus, Ohio, 1987.

[22] AE Sensors & Preamplifiers Users Manual, Part no. 1220-1001, Physical Acoustics Corporation, Princeton, New Jersey, 2002.

[23] NI-SCOPE Software User Manual, Part no. 322808A-01, National Instruments Corporation, Austin, Texas, 2001.

[24] E. Lai, Practical Digital Signal Processing for Engineers and Technicians, Newnes, Burlington, Massachusetts, 2003.

[25] D.E. Newland, An Introduction to Random Vibrations, Spectral & Wavelet Analysis: Third Edition, Dover Publications Inc, New York, 2005.

[26] W.B. Fu, L.Y. Hou, L. Wang, F.H. Ma, A unified model for the microexplosion of emulsified droplets of oil and water, Fuel Processing Technology 79 (2002) 107-119.

[27] M.W. Rohsenow, J.P. Hartnett, E.N. Ganić, Handbook of Heat Transfer Fundamentals: 2nd edition, McGraw-Hill, New York, 1985.

[28] Christian Grosse, Hsu-Nielsen Source, NDT.net, Germany, "Available: http://www.ndt.net/ndtaz/content.php?id=474", (1 Dec. 2011).

[29] J. Yu, P. Ziehl, B. Zarate, J. Caicedo, L. Yu, V. Giurgiutiu, B. Metrovich, F. Matta, Quantification of fatigue cracking in CT specimens with passive and active piezoelectric sensing, Proceedings of SPIE 7649 (2010) 76490R-1.

[30] H. Vallen, AE testing fundamentals, equipment, and applications, Journal of Nondestructive Testing (Germany) 7 (2002) 1-30.

[31] H. Yamasaki, Y. Obata, H. Nomura, Y. Ujie, Analytical study on microexplosion processes of a burning emulsion droplet using acoustic emission, Nihon Kikai Gakkai Nenji Taikai Koen Ronbunshu 3 (2005) 125-126.

[32] J. Tanaka, S. Nakajima, K. Tanaka, C.Y. Kim, K. Korematsu, Study on microexplosion of a droplet of emulsified fuel and its acoustic emission, Transactions of the Japan Society of Mechanical Engineers B 68, (2002) 1302-1307.

[33] J.C. Birchley, N. Riley, Transient evaporation and combustion of a composite water/oil droplet, Combustion and Flame 29 (1977) 145-162.

[34] J.M. Morais, O.D.H. Santos, T. Delicato, R.A. Gonçalves, P.A. Rocha-Filho, Physicochemical characterization of canola oil/water nano-emulsions obtained by determination of required HLB number and emulsion phase inversion methods, Journal of Dispersion Science and Technology 27 (2006) 109-115.

[35] N. Kaneko, T. Horie, S. Ueno, J. Yano, T. Katsuragi, K. Sato, Impurity effects on crystallization rates on n-hexadecane in oil-in-water emulsions, Journal of Crystal Growth 197 (1999) 263-270.

[36] C.A. Crowley, Electric furnace of developing temperature of 1650˚F for enameling, annealing and heat-treatment, Popular Mechanics 67 (1937) 941-946.

[37] Angie Turner, Emulsifiers with HLB Values, The Herbarie, Prospertiy, South Carolina, "Available: http://www.theherbarie.com/files/resource-center/formulating/Required_HLB_for_Oils_and_Lipids.pdf", (16 Dec. 2011).

[38] M.C. Potter, J.L. Goldberg, E. Aboufadel, Advanced Engineering Mathematics: Third edition, Oxford University Press, Oxford, 2005.

[39] R.C. Hibbeler, Engineering Mechanics: 12th edition, Pearson Prentice Hall, Upper Saddle River, New Jersey, 2010.

[40] Y. Suzuki, T. Harada, H. Watanabe, M. Shoji, Y. Matsushita, H. Aoki, T. Miura, Visualization of aggregation process of dispersed water droplets and the effect of aggregation on secondary atomization of emulsified fuel droplets, Proceedings of Combustion Institute 33 (2011) 2063-2070.

APPENDIX A

MICROEXPLOSION WAVE PROPAGATION

A partial differential equation was used to understand the wave motion traveling through a solid bar. u (x,t) is the displacement of the elastic plane of particles moved by longitudinal shock wave. Assumptions were made based on shown in Figure 40.

1. The bar has a constant cross-section area in the unstrained state

2. All cross-sectional planes remain flat surface and every element of membrane moves normal to the y-z plane

3. Hooke's law can be applied to relate stress and strain

4. The mass of membrane per unit area is constant

5. Elastic modulus of object is constant

$$\frac{\partial^2 u}{\partial t^2} = a^2 \frac{\partial^2 u}{\partial x^2}$$
(29)

where, $a = \sqrt{\dfrac{E}{\rho}}$ is the longitudinal wave speed (m/s)

An explosive force acting on the end of the bar was used to represent the microexplosion effect as shown in Figure 40.

Boundary Conditions

① $u(0,t)=0$ for no displacement at $x=0$

② $\dfrac{\partial u}{\partial x}(L,t)=0$ for no displacement gradient at free end at $x=L$

③ $u(x,0)=0$ for no initial displacement at $t=0$

④ $\dfrac{\partial u}{\partial t}(x,0)=\dfrac{Ft'}{m}$ for the impulse at $t=0$

Since the partial differential equation and the boundary condition are homogeneous, the separation variables method is used. $u(x,t)$ can be displayed with $\phi(x)$ and $h(t)$.

$$u(x,t)=\phi(x)h(t) \tag{37}$$

Substituting Equation (37) into Equation (29) with the separation constant (the eigenvalues) $-\lambda$ yields

$$\dfrac{1}{a^2}\dfrac{h''(t)}{h(t)}=\dfrac{\phi''(x)}{\phi(x)}=-\lambda \tag{38}$$

The displacement-dependent $\phi(x)$ terms from Equation (38) is,

$$\phi''(x)+\lambda\phi(x)=0 \tag{39}$$

General solution of Equation (39) is

$$\phi(x)=C_1\cos\left(\sqrt{\lambda}x\right)+C_2\sin\left(\sqrt{\lambda}x\right) \tag{40}$$

The B.C ① and Equation (40) show that

$$\phi(0)=C_1=0 \tag{41}$$

The B.C ②, Equation (40) and Equation (41) show that

$$\phi'(L)=C_2\cos\left(\sqrt{\lambda}L\right)=0 \tag{42}$$

Since ø(x) in Equation (40) is not zero, $\cos\left(\sqrt{\lambda}L\right)$ in Equation (42) should be zero. It concludes that

$$\sqrt{\lambda}L = \frac{\pi}{2} + n\pi \tag{43}$$

$$\lambda = \left(\frac{(2n+1)\pi}{2L}\right)^2 \qquad n=1, 2, 3\ldots \tag{44}$$

Thus,

$$\therefore \phi(x) = C_2 \sin\left(\sqrt{\lambda}x\right) \tag{45}$$

Now, the time-dependent h(t) terms from Equation (38) is

$$h''(t) + \lambda a^2 h(t) = 0 \tag{46}$$

General solution of Equation (46) is

$$h(t) = C_3 \cos\left(a\sqrt{\lambda}t\right) + C_4 \sin\left(a\sqrt{\lambda}t\right) \tag{47}$$

The B.C ③ and Equation (47) show that

$$h(0) = C_3 = 0 \tag{48}$$

Thus

$$\therefore h(x) = C_4 \sin\left(a\sqrt{\lambda}t\right) \tag{49}$$

After substituting Equation (45) and Equation (49) into Equation (37), the solution of the one-dimensional wave equation can be written as

$$\therefore u(x,t) = \sum_{n=0}^{\infty} C_n \sin\left(\sqrt{\lambda}x\right) \cdot \sin\left(a\sqrt{\lambda}t\right) \tag{50}$$

where, $C_n = C_2 \times C_4$ is a constant variable

Finally, the B.C ④ and Equation (50) show that

$$\frac{\partial u}{\partial t}(x,t) = a\sqrt{\lambda}\sum_{n=0}^{\infty}C_n\sin\left(\sqrt{\lambda}x\right)\cdot\cos\left(a\sqrt{\lambda}t\right) \tag{51}$$

$$\frac{\partial u}{\partial t}(x,0) = \sum_{n=0}^{\infty}C'_n\sin\left(\sqrt{\lambda}x\right)\cdot 1 = \frac{Ft'}{m} \tag{52}$$

Since it is known $\int_0^L \sin^2 xdx = \frac{L}{2}$, multiply $\int_0^L \sin\left(\sqrt{\lambda}x\right)dx$ and each side,

$$\sum_{n=0}^{\infty}C'_n\sin\left(\sqrt{\lambda}x\right)\cdot\sin\left(\sqrt{\lambda}x\right) = \frac{Ft'}{m}\cdot\sin\left(\sqrt{\lambda}x\right) \tag{53}$$

$$C'_n\cdot\int_0^L\sin^2\left(\sqrt{\lambda}x\right)dx = \frac{Ft'}{m}\int_0^L\sin\left(\sqrt{\lambda}x\right)dx \tag{54}$$

$$C'_n = \frac{2}{L}\cdot\frac{Ft'}{m}\int_0^L\sin\left(\sqrt{\lambda}x\right)dx \tag{55}$$

Final solution of the one-dimensional wave motion of Equation (29) shows

$$\therefore u(x,t) = \sum_{n=0}^{\infty}C'_n\sin\left(\sqrt{\lambda}x\right)\sin\left(a\sqrt{\lambda}t\right) \tag{56}$$

where, $C'_n = \frac{2}{L}\cdot\frac{Ft'}{m}\int_0^L\sin\left(\sqrt{\lambda}x\right)dx$

$$\lambda = \left(\frac{(2n+1)\pi}{2L}\right)^2 \qquad n=1,\ 2,\ 3\ldots$$

APPENDIX B

MATLAB CODE OF FAST FOURIER TRANSFORMS

The microexplosion frequencies were obtained using the following Matlab code. Fast Fourier Transform algorithm was used to obtain frequency information from the wave signal data collected by NI USB DAQ.

```matlab
load CW_16.dat ; % Load wave signal data
f1= CW_16(:,1); % Time data
f2= CW_16(:,2); % Amplitude data


% Plot signal waves on time domain
plot(f1,f2), grid, title('Waves','fontsize', 24);
xlabel('Time (Sec)','fontsize', 24)
ylabel('Amplitude (V)','fontsize', 24)
pause


Y = fft(f2); % Returns the discrete Fourier transform (DFT) of
vector x,computed with a fast Foureir transfrom algorithm


N = length(Y); % length of N value
Y(1) = [];
```

```matlab
power = abs(Y(1:N/2)).^2; % Fine single-sided spectrum by using
abs function


freq = (1:N/2)/(N/2); % Fine frquency points


% Plot single-sided amplitue spectrum
plot(freq,power), grid onxlabel('Frequency(MHz)','fontsize',
24)
ylabel('Power','fontsize', 24)
title('FFT Power Spectrum','fontsize', 24)


% Save frequency data
z=[freq', power];
save CW_16 z /ascii
pause
```

VITA

Hyungseok Nam was born in Busan, Korea. He received his Bachelor of Science degree in Mechanical Engineering from SungKyunKwan University in August 2009. He enrolled in Texas A&M University, College Station in Fall 2009 and received his Master of Science in mechanical engineering in May 2012.

Mr. Nam can be contacted by email at namhs219@gmail.com. He can be contacted in person at,

Texas A&M University

Department of Mechanical Engineering

3123 TAMU

College Station

TX 77843-3123